PIPELINE RESPONSE TO EARTHQUAKE-INDUCED GROUND DEFORMATION

A Dissertation

Presented to the Faculty of the Graduate School

of Cornell University

In Partial Fulfillment of the Requirements for the Degree of

Doctor of Philosophy

by

Christina Argyrou

May 2018

PIPELINE RESPONSE TO EARTHQUAKE-INDUCED GROUND DEFORMATION

Christina Argyrou, Ph. D.

Cornell University 2018

The primary focus of this thesis is the evaluation through experimental and numerical investigations of pipeline performance under earthquake-induced ground deformation. This kind of deformation is associated with soil liquefaction, landslides, fault rupture, tectonic uplift and subsidence and settlement of loose granular soils.

A large part of this thesis involves the earthquake response of pipelines with defects, e.g., cracks and/or leaking joints, rehabilitated with cured-in-place linings (CIPLs). The thesis begins with the description of a series of full-scale static and dynamic axial tension tests to characterize the tensile capacity of CIPL-reinforced pipelines. The CIPL de-bonding is of great importance for the accommodation of tensile deformation. The amount of CIPL de-bonding is a function of the CIPL properties (i.e. stiffness, tensile strength) with respect to the pipe/CIPL interface bond strength, which increases with increasing internal pressure. A one-dimensional finite element model is developed that accounts for the CIPL de-bonding mechanism as a Mode II fracture propagation phenomenon, including the enhanced pipe/CIPL interface strength in the presence of internal pressure. Seismic wave interaction with CIPL-reinforced pipelines subjects them to alternating tension and compression as the waves propagate through the ground. The combinations of ground velocity amplitude and pulse period that cause

lining deformation are evaluated through analytical models of seismic wave/pipeline interaction and finite element simulations.

CIPL-strengthened pipeline response to permanent ground deformation was also investigated through large-scale fault rupture experiments and numerical simulations. Fault rupture test results on pipelines with CIPLs are presented and compared with test results on unlined pipelines, to assess the effectiveness of the CIPLs for seismic retrofit. The results of the numerical model developed in this work that accounts for de-bonding between the lining and pipe as Mode II fracture propagation are in good agreement with full-scale fault rupture test results.

The thesis also includes a comprehensive evaluation of ductile iron (DI) pipeline response to earthquake-induced ground deformation through the results of a large-scale testing program, including a fault rupture test on a 150-mm DI pipeline with restrained axial slip joints. Three different types of DI joints are considered in this study: push-on, restrained, and restrained axial slip joints, which are often referred to as hazard-resilient joints. A series of axial tension, axial compression, four-point bending and ground rupture test results conducted on DI jointed pipes are used to identify the limit states associated with DI joint performance. A two-dimensional finite element model accounting for (i) coupled shear/normal forces to the pipeline and (ii) bell resistance to movement, validated against large-scale fault rupture test results, is used for the quantification of the DI pipeline performance under strike-slip faulting conditions over the entire spectrum of pipeline/fault crossing angles. Pipeline performance is shown to be governed by four limit states, including tensile, compressive, and rotational capacity of the joints and local buckling of the pipe. Each limit state is related to a specific range of pipeline/fault crossing angles, which are identified and shown in parallel with the plots of maximum fault offset vs. pipeline/fault intersection angle.

BIOGRAPHICAL SKETCH

Christina Argyrou was born in Athens, Greece, on August 19th, 1987, to parents Nikolaos Argyros and Stavroula Argyrou-Fatourou. After graduating from the 5th High School in Paleo Faliro, Athens, Greece, she attended the School of Civil and Environmental Engineering at National Technical University of Athens. She obtained a Diploma in Civil Engineering with concentration in Geotechnical Engineering, in July 2011. In August 2011, she joined the Geotechnical Engineering research group in the School of Civil and Environmental Engineering at Cornell University, where she received a Master of Science in Geotechnical Engineering in January 2014.

She pursued her doctoral studies under the supervision of Thomas R. Briggs Professor Thomas O'Rourke, with minors in Structural Engineering and Systems Engineering. She worked as a research assistant in the Cornell Large-Scale Lifelines Testing Laboratory, performing numerical analyses with focus on soil-pipeline interaction problems and assisting in the design of large-scale tests. In addition, she served as a teaching assistant for 10 semesters in various classes in the area of Geotechnical and Structural Engineering (Introduction to Geotechnical Engineering, Foundation Engineering, Retaining Structures and Slopes, Soil Dynamics and Earthquake Engineering, Modern Structures, Steel Structures).

To my family

ACKNOWLEDGMENTS

I would like to express my gratitude to the chairman of my Special Committee, Thomas R. Briggs Professor Thomas D. O'Rourke, for his continuous guidance and support during my graduate studies. Without his contribution, the completion of this dissertation would not have been possible. Working under his supervision allowed me to improve as an engineer and professional.

As a teaching assistant, I had the privilege to work with Professor Harry E. Stewart who encouraged me to experiment and find my teaching style. I am also grateful to have met and advised undergraduate and graduate students who challenged me and helped me evolve as an educator. Interacting with them has always been the highlight of my day.

I would also like to thank the members of Special Committee, Professor Mircea D. Grigoriu and Professor Linda K. Nozick for their continuous support during my graduate studies.

During my work as a research assistant, I had the chance to collaborate with Tim Bond, Dimitra Bouziou, Brad Wham, Chalermpat Pariya-Ekkasut, Joe Chipalowski and multiple undergraduate students. I enjoyed every conversation we had about work, but most importantly, life.

Special thanks to Ioannis Anastasopoulos, Professor of Geotechnical Engineering, in ETH Zurich for his invaluable advice on the numerical modeling and positive outlook on life. In addition, I thank Professor Christopher J. Earls for motivating me and helping me build up my self-confidence throughout my graduate studies.

Finally, I want to express my profound gratitude and appreciation to my partner, Gustavo Rivera-Rosario for his constant love and support during the past three years. I would also like to thank my close friends, Vasiliki Kosma, Thania Charmani and Vasileios Fountoulakis, who stood by me through difficult times. Last but not least, I would like to thank my family, who has been my rock during my whole life.

TABLE OF CONTENTS

LIST OF FIGURES

LIST OF TABLES

LIST OF ABBREVIATIONS

ASCE	American Society of Civil Engineers
ASTM	American Society for Testing and Materials
AWWA	American Water Works Association
CI	Cast Iron
CIPL	Cured-In-Place Lining
CIPP	Cured-In-Place Pipe
DCDT	Direct Current Differential Transformer
DI	Ductile Iron
EPA	Environmental Protection Agency
FE	Finite Element
FEM	Finite Element Model
FRP	Fiber-Reinforced Plastic
JC	Joint Centered
JT	Joshua Tree
LADWP	Los Angeles Department of Water & Power
LEFM	Linear Elastic Fracture Mechanics
LVDT	Linear Variable Differential Transformer
PC	Pipe Centered
PGD	Permanent Ground Deformation
RI	Return Interval
SEESL	Structural Engineering & Earthquake Simulation Laboratory
TGD	Transient Ground Deformation
UB	University of Buffalo
1D/2D	One/Two-Dimensional

LIST OF SYMBOLS

A	Pipe Cross-sectional Area
b	Rate of Growth
C	Wave Propagation Velocity
C_α	Apparent Wave Propagation Velocity along Pipeline Axis
C_u	Soil Coefficient of Uniformity
d	Fault Displacement
d_c	Joint// Crack Displacement
D	Pipe Outer Diameter
D_L	Lining Outer Diameter
D_{50}	Mean Grain Size
E	Pipe Young's Modulus
E_L	Lining Young's Modulus
f	Probability Density Function
f_A	Apparent Frictional Force/Pipe Unit Length
f_T	True Frictional Force/Pipe Unit Length
f_x	Frictional Force/Pipe Unit Length
f_{xo}	Maximum Frictional Force/Pipe Unit Length for "At-rest" Conditions
f_{xu}	Frictional Force/Pipe Unit Length Coupled to Lateral Pressure
f_y	Lateral Force/Pipe Unit Length
f_{ym}	Maximum Lateral Force/Pipe Unit Length
f_{tm}	Mortar Tensile Strength
$F_{bell,ref}$	Bell Resistance at Reference Burial Depth $H_{c,ref}$
$F_{bell,Hc}$	Bell Resistance at Burial Depth H_c
$F_{bell,fym}$	Bell Resistance at Burial Depth H_c in the Zone of Maximum Lateral Forces
F_θ	Joint Tensile Capacity at Joint Rotation θ

$F_{\theta=0}$	Joint Tensile Capacity at Zero Joint Rotation
G_f	Fracture Energy
H	Burial Depth to the Pipe Crown
H_c	Burial Depth to the Pipe Centerline
$H_{c,ref}$	Reference Burial Depth to the Pipe Centerline
i	Angle of Asperities
I	Pipe Moment of Intertia
i_N	Interference Factor
i_{Nmax}	Maximum Interference Factor
K_j	Joint Spigot Stiffness
K_N	Joint Bell Stiffness when Curved End Facing Fault Rupture
K_o	"At-rest" Earth Pressure Coefficient
K_s	Lining Secant Stiffness
K_S	Joint Bell Stiffness when Flat End Facing Fault Rupture
L_{pipe}	Pipe Length
N_{qH}	Dimensionless Lateral Force/Pipe Unit Length
M	Pipe Bending Moment
N	Pipe Axial Force
N_u	Lining Ultimate Load/Width
P	Maximum Force Parallel to Pipe/Lining Interface under Zero Internal Pressure
P_u	Axial Pullout Force for Lining-Reinforced Pipe
p	Probability of Exceedance
$p(\theta)$	Soil Stress Normal to Pipe Surface as a Function of Angular Position θ
p_i	Internal Pressure
p_H	Soil Reaction Force Normal to Pipeline Longitudinal Axis
p_{max}	Maximum Soil Reaction Force Normal to Pipeline Longitudinal Axis

R	Reliability
R_p	Joint Pullout Ratio
T	Pulse Period
t	Time// Pipe Thickness
t_L	Lining Thickness
V	Ground Velocity// Pipe Shear Force
V_α	Ground Velocity along Pipeline Axis
$V_{\alpha p}$	Peak Ground Velocity along Pipeline Axis
V_p	Peak Ground Velocity
V_{pRef}	Reference Ground Velocity//Peak Ground Velocity for $\gamma_i=45^o$
V_{pRI}	Peak Ground Velocity for Recurrence Interval RI
v_p	Peak Sinusoid Pulse Velocity
w	Moisture Content
X	Distance along Pipeline Axis
α_S	Joint Rotation based on Simplified Geometric Solution
β	Pipeline/Fault Intersection Angle
γ_i	Wave/Pipeline Angle of Incidence
γ_d	Dry Unit Weight
$\bar{\gamma}$	Soil Total Unit Weight
δ	Pipe/Lining Slip
δ_H	Soil/Pipe Relative Horizontal Displacement
δ_s	Soil/Pipe Interface Friction Angle
δ_u	Pipe/Lining Maximum Slip
δ_x	Soil/Pipeline Relative Displacement along Pipeline Axis
δ_y	Lateral Soil/Pipeline Relative Displacement
δ_{ym}	Lateral Soil/Pipeline Relative Displacement at Maximum Lateral Force

ε_a	Pipe Axial Strain
ε_b	Pipe Bending Strain
ε_g	Ground Strain
ε_p	Pipe Strain
ε_u	Lining Strain at Failure// Pullout Strain
θ	Joint Rotation// Angular Position around Pipe Circumference
σ_n	Normal Stress
σ_u	Pipe Tensile Strength
σ_y	Pipe Yield Stress
τ	Shear Stress
$\tau(\theta)$	Frictional/Shear Stress to Pipe Surface as a Function of Angular Position θ
τ_{b1}	Pipe/Mortar Interface Shear Strength
τ_{b2}	Mortar/Lining Interface Shear Strength
τ_c	Pipe/Lining Interface Bond Strength
τ_f	Frictional Component of Pipe/Lining Interface Shear Strength
τ_{max}	Pipe/Lining Maximum Bond Strength
ϕ_b	Surface-to-Surface Friction Angle
ϕ'	Soil Friction Angle

CHAPTER 1

INTRODUCTION

1.1 Overview

Pipeline networks are of vital importance for the security and welfare of modern societies. Water distribution and energy pipeline systems are critical, not only under normal operating conditions, but also during recovery after extreme events. The US water infrastructure inventory includes well over 1 million miles of water distribution and transmission pipelines, with 38% of the total number consisting of cast iron (CI) pipelines installed more than 50 years ago (US.EPA, 2013; US.EPA, 2002a). Research indicates that annual repair rates as high as 25-30/100 miles/year should be expected (Grigg, 2007; Deb et al., 2002), with the cost for pipe replacement exceeding $1.9 trillion by 2050 (AWWA, 2012).

Cast iron is an iron-carbon alloy with low melting temperature, responsible for its castability and machinability. Brittle material behavior combined with low flexural rigidity of CI pipes, makes them highly vulnerable to ground deformation. In addition, CI pipes are susceptible to graphitization, a natural process in which iron or iron alloys degrade in softer materials, contributing to their deterioration. Since the mid-1960s, ductile iron (DI) pipelines have been used to replace aging CI pipelines in the US (US.EPA, 2002b). Ductile iron pipelines are most often installed with push-on joints that provide little resistance to pull-out, and thus are especially vulnerable to ground deformation that is accompanied by lateral movement. Restrained DI joints, which resist pull-out, are commercially available. More recently, DI pipelines with restrained axial

slip joints have been developed and marketed as earthquake resistant or hazard resistant pipelines for water distribution (Pariya-Ekkasut, 2018; Wham et al., 2017; Stewart et al., 2015). Such pipelines can accommodate lateral soil movement through slip at the joints combined with axial resistance to pullout.

Ground deformation can be induced under normal operating conditions by traffic loading, seasonal freeze-thaw cycles, settlement, frost heave, and construction activities, such as excavations and tunneling. Ground deformation also occurs under extreme loading conditions such as earthquakes, hurricanes, floods, and subsidence due to dewatering or mining activities.

The vulnerability of pipelines to earthquake damage has been well documented (O'Rourke et al., 2014, 1992, 2006; Tang, 2000). For instance, the San Francisco earthquake in 1906 resulted in at least 300 broken distribution pipelines and approximately 23,200 broken service laterals (Eidinger et al., 2006), diminishing firefighting capacity. O'Rourke et al. (2006) showed that the damage in the pipeline network was concentrated at the areas of liquefaction and severe ground failures. More recently, after the February 2011 Christchurch earthquake, 1645 repairs to mains and sub-mains were required in a network of 1060 miles due to liquefaction-induced deformations (O'Rourke et al., 2014).

Earthquake damage to underground pipelines is caused by transient ground deformation (TGD), permanent ground deformation (PGD), or both. The sources and types of earthquake-induced ground deformation are summarized by Bird et al. (2004). Transient ground deformation affects large geographic areas, with pipeline damage caused by seismic wave–pipeline interaction at levels of ground strain lower than those

caused by PGD. Transient ground deformation effects occur during every earthquake event and normally cease to exist after shaking has stopped. On the contrary, PGD effects result in permanent strain in the pipeline and may not be prominent after earthquakes with low to moderate intensity. Earthquake induced PGD is associated with ground rupture phenomena, such as soil liquefaction, landslides, fault rupture, tectonic uplift and subsidence and settlement of loose granular soils (O'Rourke, 1998). Although affecting smaller geographic areas than TGD, PGD, especially due to liquefaction, has been shown to induce higher damage rates for water distribution systems (O'Rourke et al., 2014; Bray et al., 2013; O'Rourke & Jeon, 2000; Hamada & O'Rourke, 1992; Elhmadi and O'Rourke, 1990).

In summary, a high percentage of the underground pipeline inventory in the US is highly vulnerable to ground deformation from all causes, but especially from earthquakes and other extreme natural hazards. There is the need to develop and utilize pipelines that can accommodate large ground deformation, and thereby improve the resilience of water supplies and energy delivery systems. There is also the need to rehabilitate aging CI mains with in situ lining technologies installed with trenchless construction methods so that pipelines are strengthened for additional service life without disruptive excavation in crowded urban and suburban locations. Improving the response of pipelines to large ground deformation during extreme events automatically improves their performance under normal operating conditions in which lower levels of deformation need to be sustained. Retrofitting pipeline systems for resilience to natural hazards is an integral part of infrastructure improvement for extended service life and improved daily performance.

1.2 Motivation of Study

Cured-in-place linings and pipes (CIPLs and CIPPs, respectively) are used to reinforce underground pipelines in situ, thereby increasing the service life of aging underground infrastructure. The linings are installed through trenchless construction procedures (Kramer et al. 1992), minimizing the cost and the disturbance to the surrounding infrastructure associated with the traditional cut-and-cover techniques for pipeline installation and replacement (Stein, 2005).

Cured-in-place pipe linings and pipes (CIPLs and CIPPs, respectively) are flexible and rigid structural tubes, respectively, of woven fabric or fiberglass reinforced felt saturated with epoxy or thermosetting resin and inserted and cured in existing pipelines. The linings secure continuity of pipeline flow, prevent leakage and intrusion, and provide variable degrees of structural reinforcement (AWWA, 2001; Barsoom, 1995). Although in situ polymeric linings are used frequently to rehabilitate underground lifelines for daily use, they are not used in a systematic or formal way for earthquake protection. Previous research has shown promising results with respect to the use of CIPLs and CIPPs to strengthen underground utilities against earthquake-induced transient and permanent ground deformation (Zhong et al., 2017a, 2017b, 2015, 2014; Zhong, 2014; Bouziou, 2015; Bouziou et al., 2012). However, additional experimental and numerical investigations on the performance of pipelines strengthened with CIPLs or CIPPs are required to assess their effectiveness against earthquake-induced ground deformations.

Ductile iron pipelines account for 23% of the US water distribution network (US.EPA, 2013) and are the most popular choice for the replacement of deteriorated CI

pipelines since the 1960s (US.EPA, 2002b). There are three main DI joint types commercially available: push-on, restrained and hazard-resistant joints (Stewart et al., 2015). All three types are equipped with a rubber gasket to prevent leakage. However, the geometries of the joints differ significantly. For example, the restrained joints employ restraining clips as a locking mechanism to resist pullout under tension. The hazard-resistant joints may likewise employ restraining clips to resist pullout, but possess an elongated bell to allow for axial slip of the spigot for both tension and compression. The hazard-resilient joint will be referred as restrained axial slip joint throughout this work. Full-scale axial tension, axial compression, four-point bending and ground rupture tests have been performed on push-on, restrained and restrained axial slip DI jointed specimens at Cornell University Large-Scale Lifelines Testing Laboratory (Stewart et al., 2015; Wham and O'Rourke, 2015; Pariya-Ekkasut, 2018). This set of experimental results serves as a basis for identifying limit states and assessing the relative performance of DI pipelines with different types of joints under various conditions of ground deformation.

The motivation for this thesis is the need for quantifying the performance of CIPLs as a means for improving the seismic response of existing pipeline systems. The motivation also extends to DI pipelines and the need to understand and quantify the seismic response of DI pipeline with different types of joints.

1.3 Objectives

One of the main objectives of this research is to help to correct one of the most critical deficiencies in current underground utility practice, namely the lack of verification of

in situ trenchless lining technology for the retrofit of existing lifelines against earthquake effects. This is achieved through the evaluation of the performance of pipelines retrofitted with CIPLs under earthquake-induced ground deformations through experimental and numerical investigations. Another principal objective is to evaluate the response of DI pipelines with different types of joints and to provide guidance for the selection of the appropriate DI joint for the preliminary design of a new pipeline or replacement of an existing one. This is accomplished by assessing the relative performance of DI jointed pipelines with different types of joints under PGD through systematic numerical simulations. These objectives are discussed under the subheadings that follow.

1.3.1 Response of Pipelines Retrofitted with Cured-In-Place Linings (CIPLs) to Earthquake-Induced Ground Deformation

A goal of this thesis is to characterize the response of pipelines with defects, i.e. circumferential cracks and/or leaking joints, rehabilitated with CIPLs under earthquake-induced ground deformations and assess their effectiveness for reinforcing existing pipelines. Previous investigations have shown that the critical mode of deformation is in the axial direction of the pipeline. Full-scale static and dynamic axial tension tests are performed to characterize the response of the CIPL-reinforced jointed pipelines under transient and permanent ground deformations, respectively, at different levels of internal pressure. The factors controlling the CIPL de-bonding from the host pipe and therefore pipeline performance are identified. A one-dimensional finite element model accounting for the CIPL de-bonding mechanism as a fracture propagation phenomenon is used to simulate the CIPL-strengthened pipelines under

tensile static tensile loads, at different levels of internal pressure.

1.3.2 Large-Scale Fault Rupture Tests on Pipelines Reinforced with Cured-In-Place Linings (CIPLs)

Another goal of this thesis is to evaluate the effectiveness of CIPLs for the reinforcement of buried pipelines against permanent ground deformation (PGD). The response of jointed pipelines with and without CIPLs under strike-slip faulting conditions is investigated and quantified through large-scale fault rupture tests. A two-fold modeling process, in which the pipeline response is decomposed into longitudinal and lateral components, is developed. A two dimensional finite element soil-pipeline-lining interaction model is developed and used to simulate CIPL-reinforced pipeline performance under earthquake-induced PGD. Recommendations are made for applying the findings of this study for in situ strengthening of the underground pipelines.

1.3.3 Ductile Iron Pipeline Response to Earthquake-Induced Ground Rupture

An additional goal of this work is to evaluate the performance of ductile iron (DI) pipelines with different types of joints under abrupt PGD. Three typical types of DI joints, including push-on, restrained and restrained axial slip joints, are examined in this work. The limit states for jointed pipeline performance are identified and used to quantify the effectiveness of each type of DI pipeline to accommodate ground deformation under strike-slip faulting conditions. A systematic assessment of the pipeline response is performed through two-dimensional finite element simulations for

any pipeline/fault crossing angle. The results of this work allow for the quantification of the relative performance of different DI pipelines under large ground deformation and provide guidance for simplified design.

1.4 Scope and Organization

This thesis consists of five chapters, the first of which provides introductory and background information, explains the thesis objectives, and describes the scope and organization of the work. Chapters 2 to 4 are organized in the format of three individual papers. Chapter 2 deals with the performance of pipelines with defects reinforced with CIPLs under earthquake-induced ground deformation in the pipeline longitudinal direction. It describes full-scale static and dynamic axial tension tests and presents a one-dimensional finite element model for the CIPL de-bonding mechanism. Chapter 3 evaluates the response of the pipelines with and without CIPLs under strike-slip faulting conditions through large-scale testing. It also describes finite element soil-pipeline interaction models for the response of the CIPL-reinforced pipelines under permanent ground deformation. Chapter 4 provides a comparative assessment of the performance of DI pipelines with different types of joints under strike-slip faulting conditions for all possible pipeline/fault crossing angles. Chapter 5 presents the conclusions of this work, and provides recommendation for future research.

REFERENCES

AWWA. (2012). "Buried No Longer: Confronting America's Water Infrastructure." American Water Works Association, Denver, CO, available at: https://www.awwa.org/Portals/0/files/legreg/documents/BuriedNoLonger.pdf.

AWWA. (2001). "Rehabilitation of Water Mains." *Manual of Water Supply Practices M28, 2nd Ed.*, American Water Works Association, Denver, CO.

Bird, J., O'Rourke, T.D., Bracedirdle, A., Bommer, J. and Tromans, I. (2004). "A Framework for Assessing Earthquake Hazards for Major Pipelines." *International Conference on Terrain and Geohazards Facing Onshore Oil and Gas Pipelines*, London, UK.

Barsoom, J. (1995). "Trenchless Pipeline Technology." *ASTM Standardization News*, 23(5), May 1995.

Bouziou, D. (2015). "Earthquake-Induced Ground Deformation Effects on Buried Pipelines." PhD Dissertation: Cornell University.

Bouziou, D., Wham, B.P., O'Rourke, T.D., Stewart, H.E. and Palmer, M.C. (2012). "Earthquake Response and Rehabilitation of Critical Lifelines." *15th World Conference on Earthquake Engineering*, Sept. 24-28, Lisbon, Portugal.

Bray, J.D., O'Rourke, T.D., Cubrinovski, M., Zupan, J.D., Jeon, S.-S., Taylor, M., Toprak, S., Hughes, M., van Ballegooy, S., Bouziou, D. (2013). "Liquefaction Impact on Critical Infrastructure in Christchurch." *Final Technical Report, U.S.G.S. award number G12AP20034*, available at: http://earthquake.usgs.gov/research/external/reports/G12AP20034.pdf.

Deb, A. K., Grablutz, F. M., Hasit, Y. J., Snyder, J. K., Loganathan, G. V. and Agbenowsi, N. (2002). "Prioritizing Water Main Replacement and Rehabilitation." American Water Works Association Research Foundation, Denver, CO.

Eidinger, J., de Castro, L. and Ma, D. (2006). "The 1906 Earthquake Impacts on the San Francisco and Santa Clara Water Systems-What We Learned, and What We Are Doing About It." *Earthquake Spectra*, 22 (S2), pp. 113-134.

Elhmadi, K. and O´Rourke, M.J. (1990). "Seismic Damage to Segmented Buried Pipelines." *Earthquake Engineering & Structural Dynamics*, 19(4): 529-539.

Grigg, N.S. (2007). "Main Break Prediction, Prevention and Control." American Water Works Association Research Foundation, Denver, CO.

Hamada, M. and O'Rourke, T.D. (1992). "Case Studies of Liquefaction and Lifeline

Performance during Past Earthquakes. Japanese Case Studies." *Technical Report, NCEER-92-0001,* Vol.1: National Center for Earthquake Engineering Research, Buffalo, NY.

Kramer, S. R., McDonald, W.J. and Thomson, J.C. (1992). "An Introduction to Trenchless Technology." Van Nostrand Reinhold, New York, NY.

O'Rourke, T.D., Jeon, S.-S., Toprak, S., Cubrinovski, M., Hughes, M., Ballegooy, S. and Bouziou, D. (2014). "Earthquake Response of Underground Pipeline Networks in Christchurch, NZ." *Earthquake Spectra,* 30 (1), pp. 183-204.

O'Rourke, T.D., Bonneau, A., Pease, J., Shi, P., and Wang, Y. (2006). "Liquefaction Ground Failures in San Francisco." *Earthquake Spectra*, 22 (S2), pp.91-112.

O'Rourke, T.D. and Jeon, S.-S. (2000). "Seismic zonation for lifelines and utilities." *Invited Keynote Paper on Lifeline*s, *6th International Conference on Seismic Zonation*, Palm Springs, CA, EERI CD ROM, 35p.

O'Rourke, T.D. (1998). "An Overview of Geotechnical and Lifeline Earthquake Engineering." *Proceedings of Specialty Conference on Geotechnical Earthquake and Soil Dynamics*, Vol. 2, 75, pp. 1392-1426, Seattle, Washington.

O'Rourke, T. D., Roth, B.L., and Hamada, M. (1992). "Large Ground Deformations and Their Effects on Lifeline Facilities; 1971 San Fernando Earthquake." *NCEER-92-0002*, 3:1-85, National Center for Earthquake Engineering Research, Buffalo, NY.

Pariya-Ekkasut, C. (2018). "Characterization of Hazard-Resilient Ductile Iron Pipelines Response to Earthquake-Induced Ground Deformation." PhD Dissertation: Cornell University.

Stein, D. (2005). "Trenchless Technology for Installation of Cables and Pipelines." *Stein and Partner*, Arnsberg, Germany.

Stewart, H.E., Pariya-Ekkasut, C., Wham, B.P., O'Rourke, T.D., Argyrou, C., and Bond, T.K. (2015). "Hazard Resilience Testing of US Pipe Ductile Iron TR-XTREME™ Pipe Joints." *Report prepared US Pipe*, Feb. 2015, Cornell University, Ithaca, NY.

Tang, A. (2000). "Izmit (Kocaeli), Turkey, Earthquake of August 17, 1999, Including Duzce Earthquake of November 12, 1999-*Lifeline Performance." ASCE, Technical Council on Lifeline Earthquake Engineering, Monograph No.17*, Reston, VA.

US. EPA. (2013). "Primer on Condition Curves for Water Mains." *Final Report, EPA/600/R-13/080,* United States Environmental Protection Agency, Cincinnati, OH.

US.EPA. (2002b). "Deteriorating Buried Infrastructure Management Challenges and Strategies." Available at: United States Environmental Protection Agency, Washington, DC.

US. EPA. (2002a). "Decision-Support Tools for Predicting the Performance of Water Distribution and Wastewater Collection Systems." *Final Report, EPA/600/R-02/029*, United States Environmental Protection Agency, Edison, NJ.

Wham, B.P., Pariya-Ekkasut, C., Argyrou, C., Lederman, A., O'Rourke, T.D. and Stewart, H.E. (2017). "Experimental Characterization of Hazard-Resilient Ductile Iron Pipe Soil/Structure Interaction under Axial Displacement." *Congress on Technical Advancement*, Sept. 10-13, Duluth, MN, available at: https://ascelibrary.org/doi/pdf/10.1061/9780784481028.013.

Wham, B.P., and O'Rourke, T.D. (2015). "Jointed Pipeline Response to Large Ground Deformation." *Journal of Pipeline Systems Engineering and Practice*, 10.1061/(ASCE)PS.1949-1204.0000207.

Zhong, Z., Filiatraut, A. and Aref A. (2017a). "Numerical Simulation and Seismic Performance Evaluation of Buried Pipelines Rehabilitated with Cured-in-place Pipe Liner under Seismic Wave Propagation." *Earthquake Engineering and Structural Dynamics*, International Association for Earthquake Engineering, 46(5):811-829.

Zhong, Z., Filiatraut, A. and Aref A. (2017b). "Experimental Performance Evaluation of Pipelines Rehabilitated with Cured-in-place Pipe Liner Under Earthquake Transient Ground Deformations." *Journal of Infrastructure Systems*, 10.1061/(ASCE)IS.1943-555X.0000326.

Zhong, Z., Filiatraut, A. and Aref A. (2015). "Seismic Performance Evaluation of Buried Pipelines Retrofitted with Cured-in-Place Pipe Liner Technology under Near-Fault Ground Motions." *Structures Congress*, April 23-25, Portland, Oregon, available at: https://ascelibrary.org/doi/10.1061/9780784479117.164.

Zhong, Z. (2014). "Earthquake Response and Rehabilitation of Critical Underground Lifelines Reinforced with Cured-in-Place Pipe Liner Technologies under Transient Ground Deformations." PhD Dissertation: University at Buffalo.

Zhong, Z., Bouziou D., Wham B., Filiatraut, A., Aref A., O'Rourke, T.D. and Stewart, H.E. (2014). "Seismic Testing of Critical Lifelines Rehabilitated with Cured-in-Place Pipeline Lining Technology." *Journal of Earthquake Engineering*, 18(6):964-985.

CHAPTER 2

RESPONSE OF PIPELINES RETROFITTED WITH CURED-IN-PLACE LININGS TO EARTHQUAKE-INDUCED GROUND DEFORMATION

Abstract

Cured-in-place linings (CIPLs) are flexible polymeric linings that can be used for the seismic retrofit of underground pipelines in situ. This paper focuses on the earthquake performance of 150-mm diameter pipelines with defects, such as weak joints and round cracks, which are reinforced with CIPLs. The most critical mode of deformation is in the axial direction of the pipeline. Full-scale tension tests show that CIPL de-bonding before rupture closely depends on the internal pipe pressure. The results of a finite element model accounting for CIPL de-bonding as a Mode II fracture propagation compare favorably with full-scale test results for different internal pressures. Quasi-static and dynamic tests on CIPL-reinforced pipes show that the CIPL can fail as the lining protrudes from a round crack that opens and closes under transient ground motion, thus "pinching" off the lining. The finite element model is used to calculate the peak ground velocity and periods leading to "pinching" failure. Recommendations are made for applying the findings of this study for the in situ strengthening of the underground pipelines.

2.1 Introduction

Cured-in-place linings and pipes (CIPLs and CIPPs, respectively) are used to rehabilitate underground pipelines in situ, thereby increasing the service life of underground infrastructure through trenchless construction procedures (Kramer et al., 1992). CIPLs and CIPPs are flexible and rigid structural tubes, respectively, of woven

fabric or fiberglass reinforced felt saturated with epoxy or thermosetting resin and inserted and cured in existing pipelines. The linings secure continuity of pipeline flow, prevent leakage and intrusion, and provide variable degrees of structural reinforcement (AWWA, 2001; Barsoom, 1995). The main goal of this paper is to explore the performance of pipelines reinforced with CIPLs to earthquake-induced ground deformations and thereby address an important deficiency in current practice, namely the lack of verification of trenchless pipe lining technology for retrofit of existing lifelines against earthquake effects.

Cured-in-place linings and pipes have benefitted from comprehensive research (Allouche et al., 2014; Ampiah et al., 2010; Bruzonne et al., 2007; Herzog et al., 2007; Guan et al., 2007; Jaganathan et al., 2007; Brown et al., 2014; Bainbridge et al., 2005; Boot, 2004), and show promise with respect to in situ retrofitting of underground utilities against earthquake-induced transient and permanent ground deformation (Zhong et al., 2017a, 2017b, 2015, 2014; Zhong, 2014; Bouziou, 2015; Bouziou et al., 2012). Experimental and analytical work by Netravali et al. (2003, 2000) and Jeon et al. (2004) demonstrate the effectiveness of CIPLs for in situ strengthening of cast iron (CI) pipelines that have full circumferential cracks and weak joints against the effects of excavation-induced ground deformation. Jeon et al. (2004) report on large-scale laboratory tests during which a CIPL reinforced CI pipeline with a round crack was able to accommodate the excavation-induced soil movements and then sustain an additional one million cycles of traffic-induced deformation without leakage. Zhong et al. (2014) report on experiments performed with twin shake tables to induce quasi-static and seismic ground motions in pipelines reinforced with CIPLs. The results

show that the retrofitted pipelines were able to accommodate high intensity transient ground motions, consistent with some of the highest near-field ground velocities ever measured. The CIPLs therefore provide substantial benefits for seismic strengthening in addition to the rehabilitation of aging underground infrastructure.

This paper begins with a description of the CIPL and ductile iron (DI) pipeline used in the experimental and analytical work. It reviews the pipeline deformation modes caused by permanent and transient ground deformations (PGD and TGD, respectively). Full-scale static and dynamic tests results are presented to evaluate the performance of CIPL-reinforced pipelines with weak joints or circumferential cracks under PGD and TGD. A one-dimensional finite element model accounting for the CIPL de-bonding under axial tension is presented and compared with the static tests results under different internal pressures. A simplified analytical model for the calculation of the weak joint or crack opening when pipeline is subjected to seismic ground waves is presented. Recommendations are made for applying modeling and experimental results for the seismic retrofit of underground pipelines.

2.2 Cured-In-Place Linings

Linings are classified based on their ability to carry loads due to internal pressure and external loads into structural, semi-structural and non-structural (AWWA, 2001). The CIPL used in this study is a semi-structural lining, commercially available as Starline2000®, which is installed by Progressive Pipeline Management, Ltd., with properties and installation methods that conform to ASTM F2207-02 (2002). As shown in Figure 2.1, the CIPL consists of a seamless woven polyester hose with a thin

interior polyurethane layer. The polyester hose is saturated with a two-part polyurethane that bonds the hose to the inside surface of the pipe. The installation of the CIPL is performed by the "inversion method", in which the polyurethane-impregnated lining is inverted into an existing, previously cleaned pipe using either heated air or water to drive the inversion process and accelerate curing.

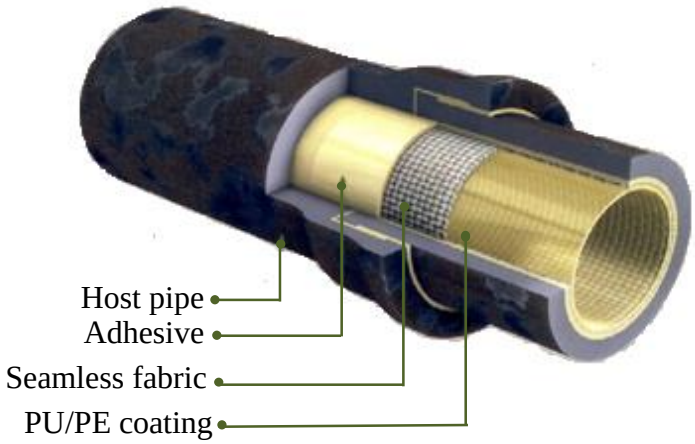

Figure 2.1. Three-Dimensional View of Cured-In-Place Lining (Progressive Pipeline Management, 2010).

The woven polyester hose is composed of yarns that are orthogonal to each other and are oriented along its axial and hoop directions. Tension tests were performed on 15-mm-wide and 200-mm-long samples in both axial and hoop directions following a modified ASTM D 3039/3039M-14 (2014). Test results reported by Stewart et al. (2015) are presented in Fig. 2.1 where force/width is plotted with respect to strain, in conformity with ASTM F2207-02 (2002). The data follow an approximately linear relationship until failure, with mean and standard deviation of strength, strain at failure, and secant stiffness of 170.6 ± 13.7 N/mm, 19.7 ± 1.5%, and 1000 ± 250

N/mm, respectively.

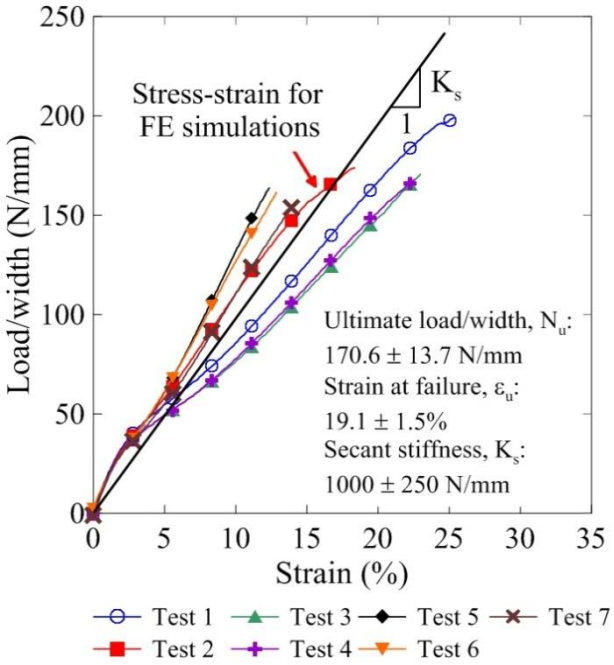

Figure 2.2. Tensile Test Results for CIPL Specimens Oriented in the Axial Direction (Stewart et al., 2015).

The linings were installed in ductile iron (DI) pipe specimens with a nominal 150mm diameter manufactured by the U.S. Pipe and Foundry Co. (US Pipe) and supplied by the Los Angeles Department of Water & Power (LADWP). The nominal 150-mm pipe outer diameter and wall thickness were 175 mm and 7.6 mm, respectively. All specimens had a 3.3-mm-thick interior cement mortar lining in conformance with AWWA C602-11 (2011). The modulus of elasticity, tensile strength and strain at rupture of the DI are 185 GPa, 417 MPa and 10.4%, respectively (Wham and O'Rourke, 2015). Figure 2.3 shows a cross-section of a push-on bell-and-spigot joint. The joint is sealed with a greased rubber gasket. During field installation, the spigot is inserted into the bell until contact between the spigot and bottom of the bell, leaving typically a small circumferential gap, on the order of 3-6 mm. The force

required to extract the fully inserted spigot from the bell varies from 0.67 to 0.89 kN (Wham & O'Rourke, 2015). Since the pullout capacity of DI joints is low with a full circumferential gap between the end of the spigot and back of the bell, they were used as proxies for CI pipelines with leaking joints or circumferential cracks, commonly encountered flaws. CI pipelines account for 38% of the US water distributions pipelines and are in operation for more 50 years, thereby constituting significant portion of the US aging infrastructure (EPA, 2013).

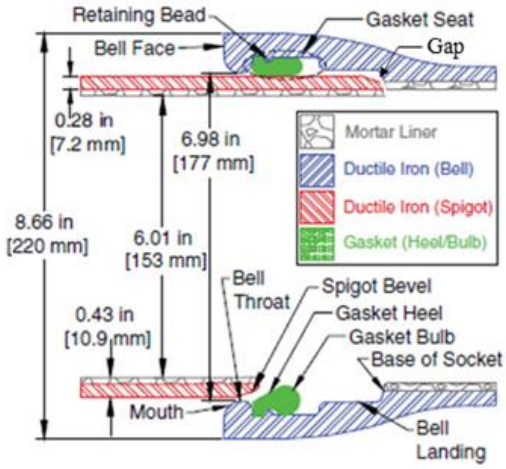

Figure 2.3. Cross-Section of a Typical 150-mm Push-on Joint (Wham & O'Rourke, 2015).

2.3 Permanent Ground Deformation

Permanent ground deformation (PGD) can arise from surface faulting, landslides, and liquefaction-induced lateral spreading and subsidence (O'Rourke et al., 2008). There are many ways in which seismic PGD affects underground pipelines, such as the oblique slip affecting pipelines crossing a fault plane in Fig. 2.4a. Strike slip may induce compression or tension, depending on the angle of intersection between the

pipeline and fault. Fig. 2.4b shows a pipeline crossing a lateral spread or landslide perpendicular to the general direction of soil movement. In this orientation, the pipeline is subject mainly to bending strains and extension. As shown in Fig. 2.4c, the pipeline will undergo bending and either tension or compression at the margins of the slide when crossing the ground movement zone at an oblique angle. Fig. 2.4d shows a pipeline oriented parallel to the general direction of soil displacement. At the head of the zone of soil movement, the displacements resemble normal faulting; under these conditions, the pipeline will be subjected to both bending and tensile strains.

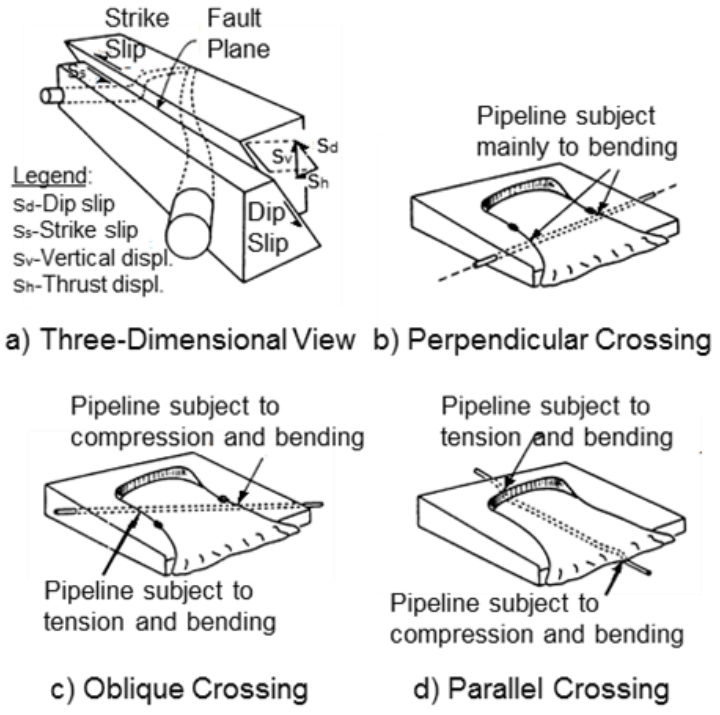

Figure 2.4. Principal Modes of Soil-Pipeline Interaction Caused by Earthquake-Induced Permanent Ground Deformation (O'Rourke et al., 2008).

2.4 Axial Tension Tests

Axial tensile deformation is the most critical response mode for pipelines reinforced with linings. De-bonding under axial extension allows the lining to increase in length, thereby accommodating tensile ground movement, provided that axial force in the lining does not exceed its tensile capacity. To assess the ability of CIPL-reinforced pipelines with circumferential cracks or weak joints to accommodate large axial deformation, full-scale axial tension tests were performed at Cornell to characterize the pullout capacity and investigate the failure mechanisms of pipelines with circumferential cracks or weak joints.

The specimens consisted either of two straight DI pipe sections separated by a 6 to 12 mm gap or two sections connected with a bell-and-spigot joint, denoted as "gap" and "joint" specimens, respectively. Figure 2.5 shows a photo of the experimental setup for the displacement controlled axial pull tests. One end of the pipe was clamped to the test frame, while the other was connected to a hydraulic 250-kN MTS actuator. During the test, the actuator force and displacement were recorded. Four string potentiometers were positioned at the pipe circumference to measure the relative displacement between the two pipe segments. Strain gages, typically between two and twelve, were installed on the exterior of the pipe at various distances from the gap or joint to measure the pipe strain and provide an indication of lining de-bonding at the respective locations. The de-bonded length was calculated based on strain gage measurements and visual inspection of the specimen interior.

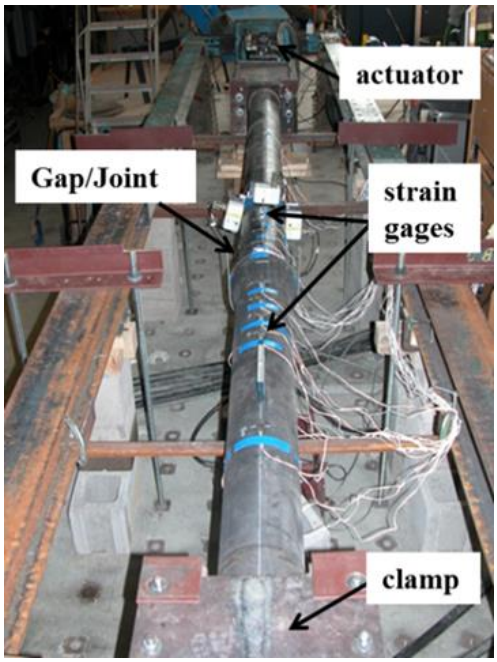

Figure 2.5. Experimental Setup for Axial Tension Tests at Cornell University.

Table 2.1 provides information on the specimen type and dimensions, loading rate, and internal pressure for each axial pull test. Tensile coupon tests performed at Cornell and UB (Zhong, 2014) show that loading rates of 1.3 mm/min to 510 mm/min do not have a significant effect on the mechanical behavior of the CIPL. Two monotonic axial tension tests conducted at UB were used as a source of supplemental data (Zhong, 2014). The tests on specimens G1 and G2 were stopped when de-bonding of the lining propagated to the end of the specimen. Specimen J5 was initially pressurized to 310 kPa, but lost internal pressure during the test, because the pressurization valves were kept closed. In addition, specimen J5 test was stopped at 102 mm of imposed displacement to avoid damage to the shake table.

2.4.1 Axial Tension Tests Results

The experimental results in terms of maximum axial force, joint/gap opening at the end of the test, observed failure mode and de-bonded length are summarized in Table 2.1. The following sections address the key test results of the lined pipe response to axial tension.

Table 2.1. Axial Tension Tests Description and Results.

Test Description					Test Results			
Specimen No.	Specimen Type	Length at each side (m)	Loading Rate (mm/min)	Pressure (kPa)	Max Force (kN)	Opening at test end (mm)	Lining Rupture	Debond. Length (mm)
G1	Gap	1.52, 1.52	5.1	0	47.3	280	No	2845
G2	Gap	1.52, 1.52	5.1	0	51.8	182	No	1880
G3	Gap	1.52, 1.52	5.1	517	81.2	81.2	Yes	381
G4	Gap	1.52, 1.52	5.1	517	88.2	88.2	Yes	559
J1	Joint	1.83, 2.74	510	517	92.1	92.1	Yes	508
J4[1]	Joint	1.83, 2.74	1.3	310	58.2	100	No	1011
J5[1]	Joint	1.83, 2.74	2.6	310	89.4	117	Yes	673

[1] Test conducted at UB (Zhong,2014).

2.4.2 Effect of Internal Pressure

Figure 2.6 shows the axial force vs. opening relationships for gap (Fig. 2.6a) and joint (Fig. 2.6b) specimens under different internal pressures. Test on specimen J5 was initiated with the water connection valve closed at an internal pipe pressure of 310 kPa. Volume expansion under tension with no water inflow would have reduced pressure rapidly to zero. Thus, the J5 test results represent near-zero pressure conditions.

Test results indicate that the response of the CIPL-strengthened pipes is strongly affected by internal pressure. The presence of internal pressure is associated with higher axial forces, and smaller de-bonded lengths and hence, lower capacity of the lined pipe to accommodate deformations compared to zero internal pressure

conditions. The additional normal stress at the pipe/CIPL interface due to internal pressure increases the pipe/CIPL interface strength, therefore reducing the tendency for lining de-bonding. The four tests (G3, G4, J1 and J4) conducted under internal pressure ended with lining rupture at axial loads ranging from 81.2 kN to 92.1 kN, consistent with the lining tensile strength obtained in tensile coupon tests.

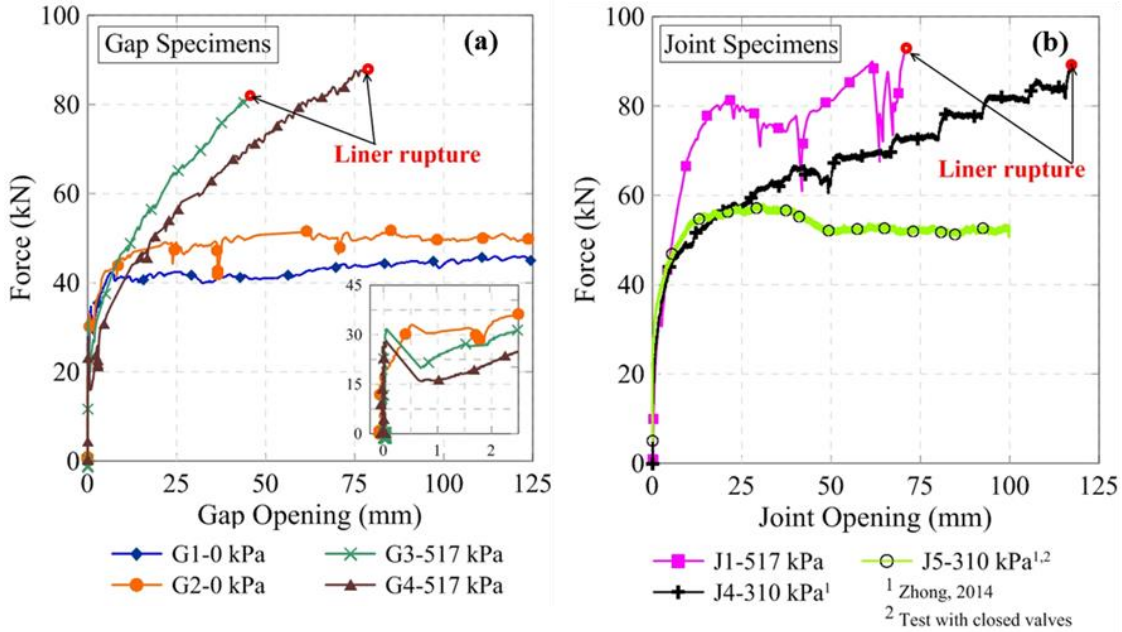

Figure 2.6. Axial Force vs. Opening Relationships under Different Internal Pressures for (a) Gap and (b) Joint Specimens.

For the tests conducted under no (i.e. G1 and G2) or near-zero internal pressure (i.e., J5), extensive de-bonding, but no lining rupture occurred. Figure 2.7 shows photos of the gap at the end of testing for specimens G3 and G1, with internal pressure of 517 kPa and 0 kPa, respectively. Fig. 2.7a shows the damaged lining with ruptured yarns, while Fig. 2.7b shows an intact lining with pieces of ruptured mortar adhered to its exterior. Internal pressure promoted lining failure in Test G3 at a relatively small

opening of 45 mm. In contrast, there was no lining failure in Test G1 at zero internal pressure, and the test was terminated at a relatively large opening of 280 mm. These tests demonstrate the importance of CIPL strength relative to the de-bonding force, which increases due to internal pressure. The de-bonded length of the lining is a function of the lining stiffness and strength relative to the pipe-lining interface strength.

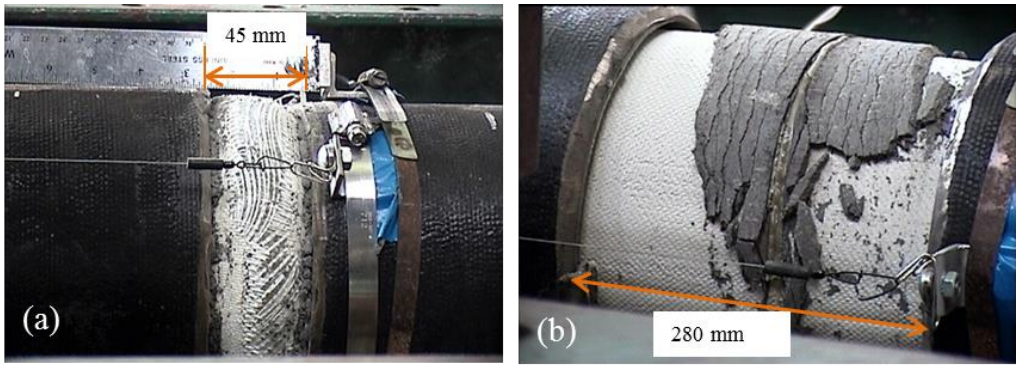

Figure 2.7. Close-up of Gap Location for Axial Tension Tests (a) Specimen G3 (517 kPa) and (b) Specimen G1 (0 kPa).

2.4.3 Gap vs. Joint Specimens

Figure 2.8 compares the response of gap and joint specimens under 517 kPa internal pressure, in terms of axial force vs. opening. The insert diagrams in Figures 2.6a and 2.8 show the response of the gap and joint specimens at axial deformation up to 2.5 mm. All gap specimens (see Fig. 2.6a) exhibit similar behavior, with an abrupt increase of the axial load for virtually zero imposed tensile displacement. The initial load varies between approximately 9 and 30 kN and results from the tensile resistance of the resin that infiltrates the gap during the lining installation process. Figure 2.9a shows a test specimen with resin filling the gap. Before resin tensile failure, the axial

load is carried by the resin and the lining. Once the resin fails, the load is carried exclusively by the lining.

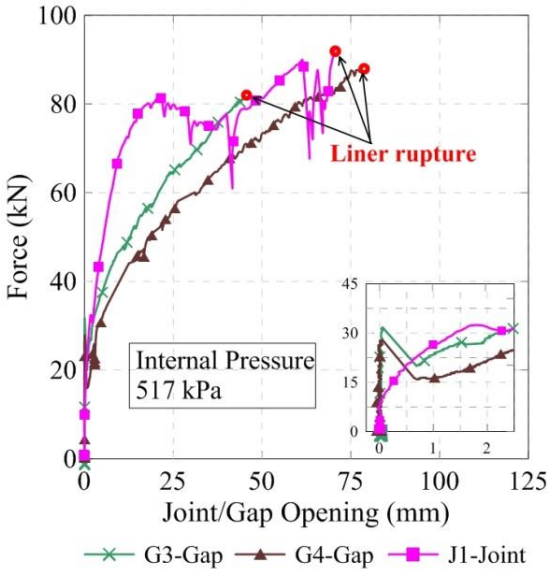

Figure 2.8. Axial Force vs. Opening Plots for Gap and Joint Specimens under Internal Pressure of 517 kPa.

The behavior of the joint specimen at early stages of loading differs from that of the gap specimen. Figure 2.9b is a photo of the cross-section of the 150-mm DI joint, showing the locations where resin can migrate during the installation process. A resin plug was observed in the separation between the end of the spigot and base of the bell. Resin that penetrates into the separation contributes to resistance against axial tensile load in a fashion similar to that of the gap specimens. There is also the possibility of resin penetrating the annular space between the bell and the spigot, and thus mobilizing additional shear resistance against joint opening. As shown in Figures 2.3 and 2.9b, the effect of resin in the annular space between the spigot and bell should be noticeable until roughly 25 mm of joint opening. As shown in Fig. 2.3, 25 mm is

the length of the bell landing. When the spigot has been pulled from that landing, there is no more capacity to develop resisting shear from resin that penetrated the annular space between the bell and spigot. The J1 test results in Figure 2.8 reflect the effects of this mechanism. J1 carries higher load compared to gap specimens G3 and G4 until approximately 25 mm of axial movement, after which the lining takes on the entire load, and its force vs. displacement response converges with that of the gap specimens.

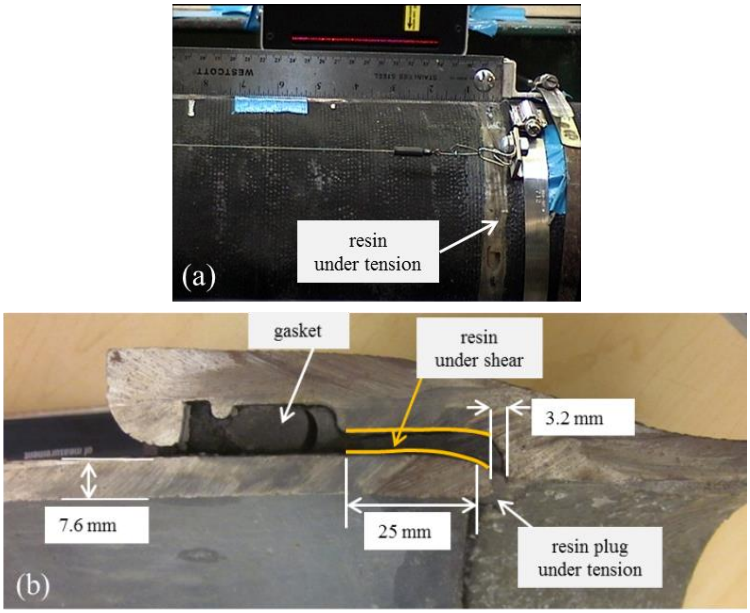

Figure 2.9. Photos of (a) Resin in Gap Specimen and (b) Cross-Section of DI Joint with Locations of Potential Resin Migration.

2.5 Numerical Modeling

2.5.1 One-Dimensional Finite Element Model (1D FEM)

Figure 2.10a shows a schematic of the 1D FEM developed with the software ABAQUS (v6.13-2) to simulate the axial tension tests described in Section 2.4, in which the pipeline and the lining are represented by beam elements (type b33) and the pipe/CIPL interface with nonlinear springs (type spring 2). The pipeline continuity is interrupted,

to simulate a crack or weak joint. Tensile displacements are applied at one end of the pipe element, while the opposite end is fixed. The mechanical properties of the pipe and the lining are consistent with those obtained from tensile coupon tests. The lining is modeled with properties only in the axial direction. De-bonding of the lining is modeled as a fracture propagation mechanism. The 1D FE model shown in Fig. 2.10a, can be modified to account for the soil-pipeline interaction for a CIPL-reinforced pipeline with defects subjected to soil displacement along its longitudinal axis, as illustrated in Fig. 2.10b. This model is further discussed in Section 2.7.3.

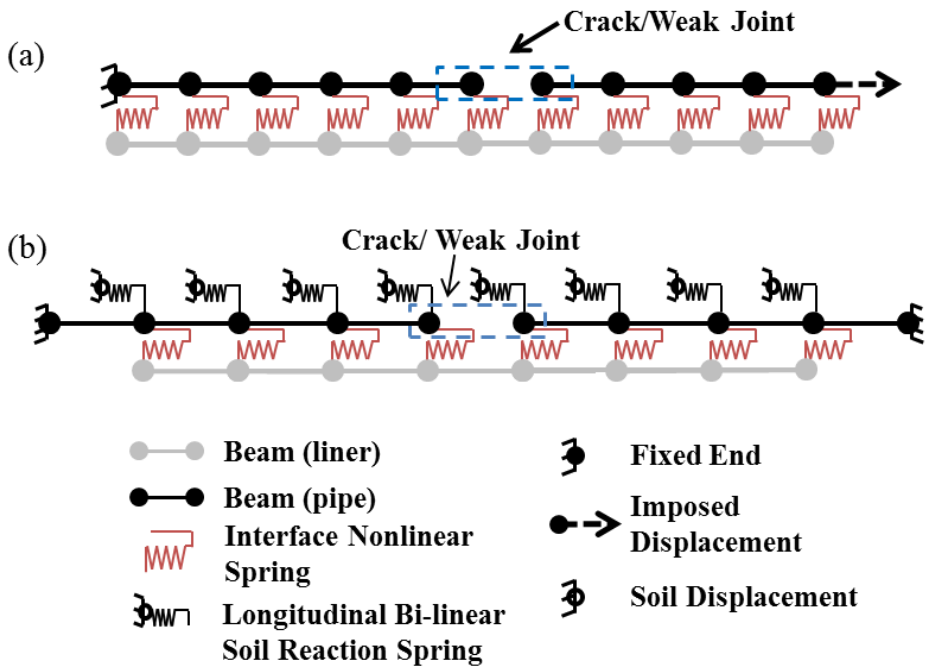

Figure 2.10. Schematics of (a) 1D FEM for Axial Tension of CIPL-Reinforced Pipelines with Cracks or Weak Joints, and (b) 1D FE Soil-Pipeline Interaction Model for CIPL-Reinforced Pipelines.

Substantial research has been conducted to investigate fracture processes in materials and structures by means of linear elastic fracture mechanics (LEFM) principles (e.g. Taljsten, 1996; Hillerborg et al., 1976), damage models (e.g. Turon et

al., 2006) and cohesive zone modeling (CZM) (e.g. Alfano et al., 2014, Spring and Paulino, 2014; Turon et al., 2007; Elices et al., 2002; Tvergaard and Hutchinson, 1992; Barenblatt, 1962; Dugdale, 1960). Caggiano et al. (2012) present a one-dimensional analytical approach for modeling the response of fiber-reinforced plastic (FRP) plates bonded to concrete, assuming elastic material response and an elastic softening relationship for the bond strength vs. slip. Similar to the Caggiano et al. (2012) model, a Mode II fracture propagation was assumed in this work, i.e. the fracture is assumed to propagate predominantly parallel to the pipe/lining interface. To simplify the problem, uniformity of the pipe/lining interface properties were assumed along the entire length of the pipeline. In this work, the pipe/mortar and mortar/lining interfaces as well as mortar layer are not modeled explicitly. Instead, a spring force vs. displacement relationship is used to represent behavior along pipe/lining interface.

2.5.2 Interface Modeling under Zero Internal Pressure

Faella et al. (2009) discuss direct and indirect optimization methods assuming an elastic-linear softening bond strength vs. slip relationship, τ_c vs. δ, to identify FRP plates-to-concrete interface relationships, based on arrays of strain gage measurements taken during direct tension tests. Multiple shapes of τ_c vs. δ curves have been suggested, including trapezoidal, rectangular, linear ascending with either linear or exponential softening (e.g. Park and Paulino, 2013; Caggiano et al., 2012; Gustafsson, 1987). A modified linear ascending and softening shape, as shown in Figure 11a, is used in this work, wherein an abrupt increase in bond strength is assumed because of

its simplicity and compatibility with the experimental data. The τ_c vs. δ relationship is characterized by the maximum apparent bond strength, τ_{max}, and the maximum slip at zero bond strength, δ_u. The area below τ_c vs. δ curve represents the fracture energy, G_f, i.e. the energy required to bring a unit area of a bonded surface to complete fracture in Mode II.

The pipe/lining interface is composed of both the pipe/mortar and the mortar/lining interfaces. Mortar slippage can occur when the bond strength at either the mortar/lining or mortar/pipe interface is exceeded. Moreover, slippage can be initiated when the tensile capacity of the mortar is reached. These conditions are illustrated by the Mohr circle for zero internal pipe pressure shown in Figure 2.11b. When axial tensile forces are applied to the lined pipe, the mortar is subjected to simple shear. As shear is increased at the mortar/lining and mortar/pipe interfaces, the Mohr circle increases in size until its radius either equals the a) mortar/lining shear capacity (point 2), b) mortar/pipe shear capacity (point 2), or c) tensile capacity of the mortar (point 1). When any one of these limit states is reached, slip or de-bonding of the lining will initiate. Therefore, the maximum bond strength, τ_{max}, can be defined as:

$$\tau_{max} = \min \left\{ f_{tm}, \tau_{b1}, \tau_{b2} \right\} \tag{2.1}$$

where f_{tm} is the tensile strength of the mortar, τ_{b1} the pipe/mortar and τ_{b2} the mortar/lining shear strength.

The value of τ_{max} was selected on the basis of published test results and observations during the axial tension tests. Sabnis et al. (1983), for example, summarize experimental results that show that concrete and mortar have direct tension strengths ranging between 8 and 12% of their compressive strengths. As required by

AWWA C602-11 (2011) the cement mortar lining for pipes should attain a minimum compressive strength of 31 MPa. Test results summarized by Sabnis et al. (1983) and Tashiro and Tatibana (1983) show that the pipe/mortar bond strength, τ_{b1}, varies between 1.4 and 3.4 MPa. Values of mortar/lining bond strength, τ_{b2}, are not available in the literature. Numerous observations during the axial tension tests, however, reveal that failure occurs as either tensile fracture in the mortar or slippage between the mortar and the pipe. Drawing from test observations as well as pipe mortar tensile capacity and pipe/mortar bond strength reported in the literature, a value of τ_{max} = 2.8 MPa (9% of the minimum compressive mortar strength) was chosen for the fracture propagation model in Fig. 2.11a.

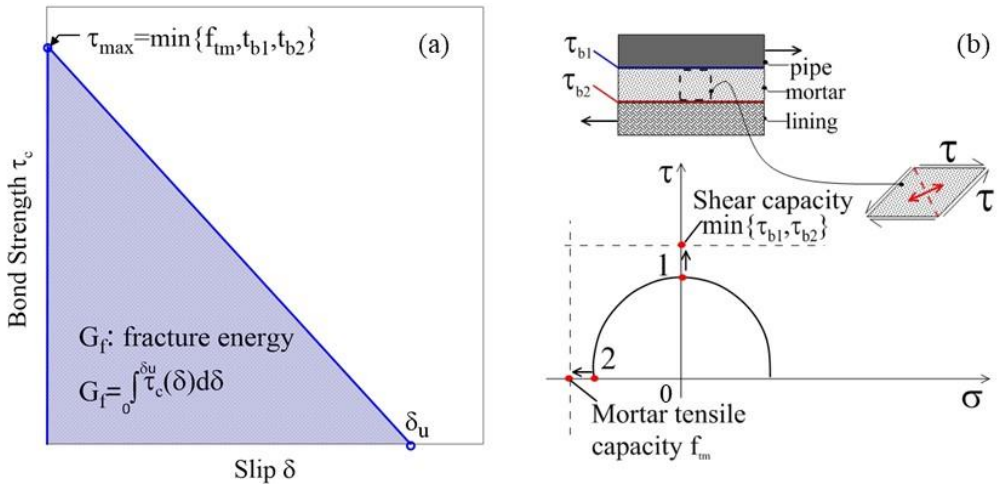

Figure 2.11. Strength Characterization for (a) Cohesion vs. Slip at Pipe-Lining Interface, and (b) Failure Modes Controlling Maximum Cohesion.

Using linear fracture mechanics Taljsten (1996) derived the following expression for the maximum force that can be resisted by an FRP-to-concrete interface:

$$P = \pi D_L \sqrt{2G_f E_L t_L} = \pi D_L \sqrt{2G_f K_S} \quad (2.2)$$

in which D_L, E_L, t_L, and K_s are the outer diameter, elastic modulus, CIPL thickness, and linear secant stiffness, expressed in terms of load/width, for the CIPL tensile test specimens, respectively (see Fig. 2.2).

As shown by Caggiano et al. (2012), the de-bonding propagation occurs at a constant force along the FRP-to-concrete interface, which is consistent with the lined pipe behavior under no internal pressure (tests G1 and G2). Therefore, Eqn. 2.2 can provide an estimate for the area below the bond strength vs. slip curve for the lined pipe, given the lining dimensions, material properties, and force measured during the tests. As shown by the axial tension test results under zero internal pressure, de-bonding propagation occurs at a constant force P equal to 45-50 kN. The CIPL thickness and outer diameter are equal to 1.4 mm and 155 mm, respectively, and the linear secant modulus of elasticity K_S is 1000N/mm. Using τ_{max} = 2.8 MPa and G_f from Eqn. 2.2, the maximum interface slip for fracture propagation characterization according to Fig. 2.11a, is δ_u = 3 mm.

2.5.3 Interface Modeling under Internal Pressure

In the presence of internal pressure, p_i, frictional forces contribute to the load transfer between the lining and the pipe. These frictional forces are assumed to follow Coulomb's frictional law for surface-to-surface contact and an interference factor that further contributes to the resistance. Patton (1966) developed an interface shear resistance model for rock discontinuities that accounts for the interlocking of asperities. The shear resistance, τ, is given by:

$$\tau = \sigma_n \tan(\phi_b + i) \tag{2.3}$$

where ϕ_b is the surface-to-surface friction angle and i is the angle of the asperities along the interface.

In our problem, the additional resistance generated by fragmentation and subsequent interaction among mortar pieces is expressed through an interference factor i_N, which is analogous to the inclination angle i used by Patton. The interference factor i_N is assumed to be a function of the slip δ, and is given by the following expression:

$$i_N(\delta) = i_{N\,max}(1 - e^{-b\delta}) \tag{2.4}$$

in which i_{Nmax} represents the maximum interference that develops as mortar fragmentation occurs and b is the growth rate of the interference factor. Since the fragmentation and slip of the mortar is analogous to slip and crushing along a rock discontinuity, values of i_{Nmax} should be consistent with the range of $10^o \leq i_{Nmax} \leq 30^o$, suggested for rock joint surfaces (Patton, 1966).

By combining the bond strength under zero pressure with frictional resistance, the interface shear strength, τ, for a lined pipe under internal pressure p_i, is given by the following expression:

$$\tau(\delta) = \tau_c(\delta) + \tau_f(\delta) = \tau_c(\delta) + \sigma_n \tan(\phi_b + i_N(\delta)) \tag{2.5}$$

where τ_c and τ_f are the bond and frictional components of the interface shear strength, respectively, σ_n is the normal stress at the pipe-lining interface, ϕ_b is the surface-to-surface friction angle and i_N is the interference factor.

Figure 2.12 shows the frictional component τ_f of Eqn. 2.5, as a function of slip δ for constant σ_n and ϕ_b. The frictional shear resistance, τ_f, increases asymptotically towards a limiting value, as a function of δ and i_N. The friction angle, ϕ_b, is taken as 35^o , as recommended by (Barton, 1973) for limestone.

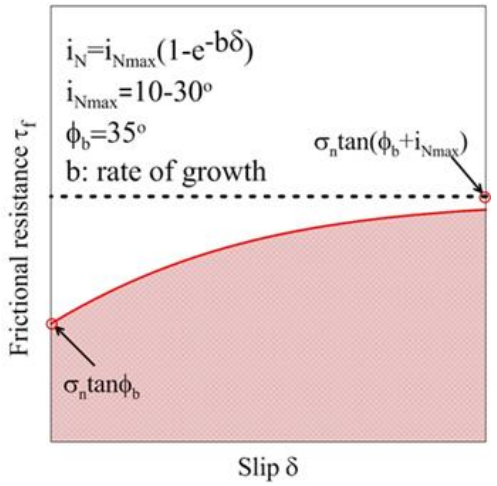

Figure 2.12. Frictional Resistance vs. Slip for Pipe-Lining Interface.

2.5.4 Determination of Normal Stress at Pipe/CIPL Interface

To determine the normal stress at the pipe-lining interface, σ_n, due to internal uniform pressure, a simplified two-dimensional (2D) axisymmetric model of the lined pipe cross-section was developed in ABAQUS 6.13 (v6.13-2). Both the host pipe and the lining were assumed to behave elastically. The modulus of elasticity used for the pipe is equal to 185 GPa. For the CIPL, the Young's modulus obtained with tensile coupon tests on specimens oriented in the hoop direction is equal to 210 MPa (Stewart et al., 2015). Because mortar has low stiffness and tensile capacity, it provides minimal resistance against radial stress and is not included in the model. The numerical results showed that 98% of the imposed internal pressure, p_i, is transferred across the lining to normal stress, σ_n, on the internal surface of the pipe. Thus, σ_n is virtually equal to

p_i.

2.5.5 Experimental vs. Numerical Results

Finite element analyses are performed with the model shown in Fig. 2.10a to simulate the axial tension tests on DI pipes lined with CIPLs described in Section 2.4. A beam element length equal to 1.3 mm was selected after mesh convergence studies. The pipe/lining interface shear strength, τ, is characterized by Eqn. 2.5. Figures 2.13 and 2.14 show comparisons of the numerical and experimental results in terms of axial force vs. gap opening and de-bonded length vs. gap opening, respectively for internal pressures of 0, 310 and 517 kPa.

For the bond strength component, τ_c, the fracture energy, G_f, is estimated with Eqn. 2.2 using the average P from Tests G1 and G2 and a τ_{max} = 2.8 MPa, which is consistent with the maximum bond strength, as discussed in Section 2.5.2, yielding a δ_u=3 mm. Figure 2.13a compares the numerical and experimental results in terms of axial force vs. gap opening for tests G1 and G2. There is good agreement between the numerical results that show de-bonding propagation at a force of 43 kN, compared to 40 and 49 kN from the G1 and G2 tests, respectively. In addition, there is close agreement between the stiffnesses provided by the numerical and experimental results. Tests G3 and G4 were used to calibrate the model for the interference factor, i_N, given by Eqn. 2.4. Using $i_{Nmax}=10^o$, the rate of growth, b, was adjusted so that numerical results fit the experimental data, as shown in Fig. 2.13b. To validate the model, the J4 test results were used. The test was conducted at a different internal pressure (i.e. 310 kPa), compared to tests G3 and G4 (i.e. 517 kPa). There is very good agreement between the experimental and numerical results, as illustrated in Fig. 2.13c.

To check further the validity of the numerical model, the measured lengths of de-bonded lining vs. gap, or joint opening, are plotted in Figure 2.14 for tests G1 and G2 (Fig. 2.14a), G3 and G4 (Fig. 2.14b) and J4 (Fig. 2.14c), and compared with the numerical results. The numerical and experimental results are in excellent agreement for the case of zero internal pressure, as shown in Fig. 2.14a, with the ratio of de-bonded length to opening being equal to approximately 10.

In the presence of internal pressure, the tendency for lining de-bonding is lower and the ratio is smaller, as shown in Figs. 2.14b and 2.14c. For internal pressure of 517 kPa, as presented in Fig. 2.14b, the numerical results follow the same trend and are in close agreement with the experimental results in terms of absolute values. Finally, for internal pressure of 310 kPa, as illustrated in Fig. 2.14c, the numerical de-bonded length vs. opening relationship follows the same general trend as the experimental data.

2.6 Transient Ground Deformation

2.6.1 Seismic Wave/Pipeline Interaction

When the effect of transient ground deformation (TGD) is concentrated at a locally weak joint or circumferential crack, there are six possible modes of deformation that can occur, as illustrated in Figure 2.15: axial, vertical and transverse horizontal displacement, vertical and horizontal rotation, as well as torsion. Previous research (O'Rourke and Liu, 2012) indicates that pipelines are primarily affected by TGD in the axial direction, whereas bending strains are roughly one to two orders of magnitude smaller than axial strains generated by shear waves (S-waves).

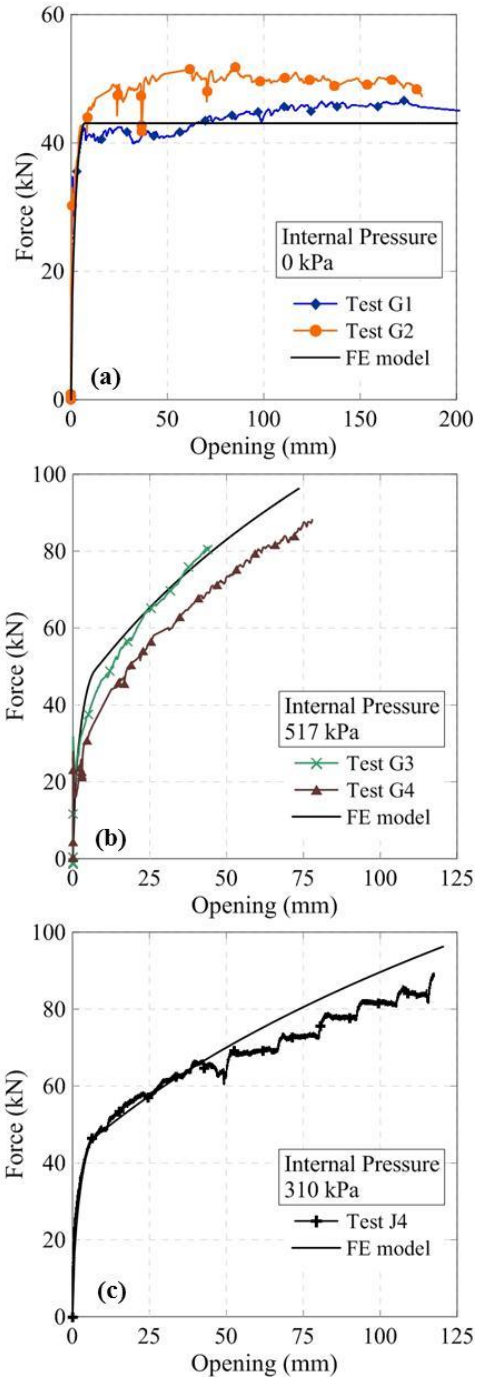

Figure 2.13. Numerical vs. Experimental Results for Axial Tension Tests on CIPL-Reinforced Pipes for Internal Pressure of (a) 0 kPa, (b) 517 kPa, and (c) 310 kPa.

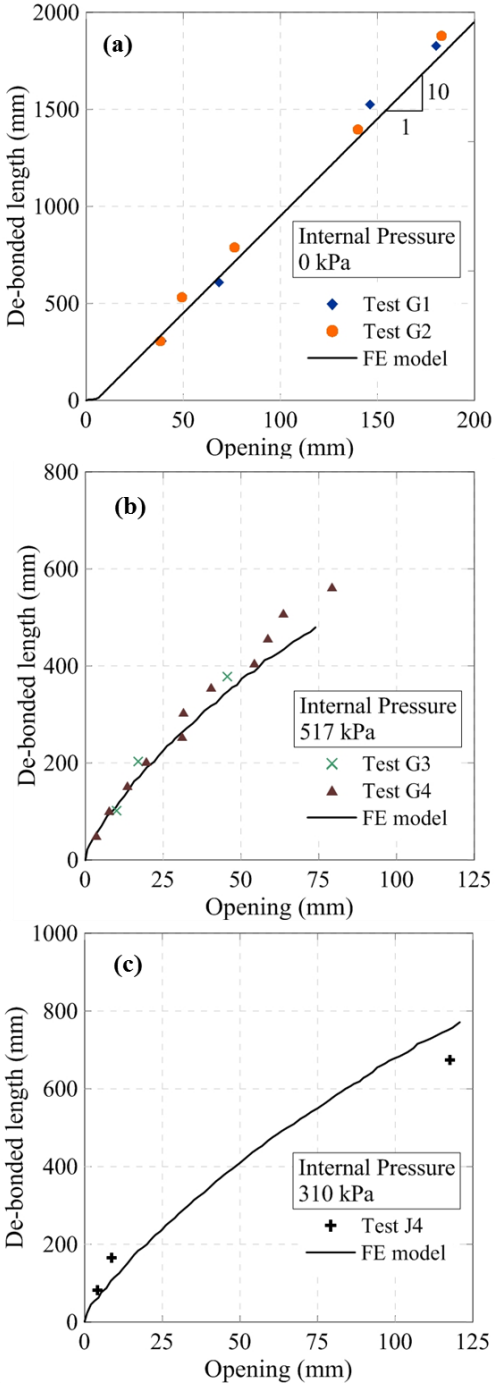

Figure 2.14. Numerical vs. Experimental Results of De-bonded Length vs. Opening for Axial Tension Tests at Internal Pressure of (a) 0 kPa, (b) 517 kPa, and (c) 310 kPa.

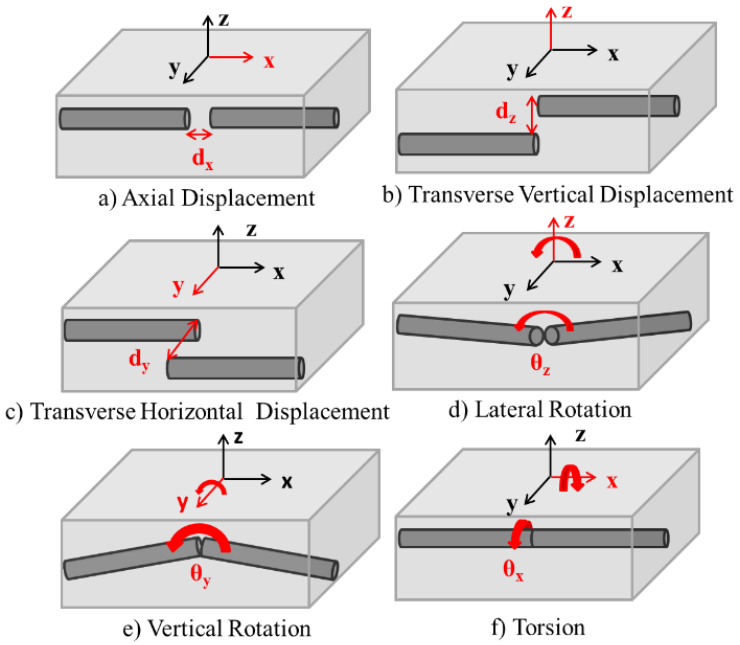

Figure 2.15. Deformations at a Weak Joint or Circumferential Crack Due to Seismic Wave Interaction.

A systematic, detailed assessment of the different modes of jointed, or segmented, pipeline response to seismic waves was performed by Bouziou (2015). The numerical results indicate that by far the most prominent form of deformation caused by seismic wave propagation occurs in the axial pipeline direction. The vertical and horizontal offsets at round cracks were found to be three orders of magnitude smaller than the round crack axial separation when the pipelines were subjected to the seismic wave motion recorded at the Rinaldi Receiving Station during the 1994 Northridge earthquake. The Rinaldi peak velocity of 148 cm/sec is among the largest recorded in the U.S. It was assumed that the azimuth of the seismic waves was oriented to induce maximum deformation of the pipeline. Lateral and vertical joint rotations were between 0.002° and 0.02°. Additional analyses for the same pipeline conditions subjected to 1999 Chi-Chi and 2011 Tohoku earthquake recorded motions, with

among the highest velocities recorded worldwide, showed similar results in which axial crack separations were approximately three orders of magnitude larger than the round crack vertical and horizontal offsets. Very small lateral and vertical joint rotations between 0.004° and 0.08° were obtained. The analyses show that non axial deformation induced by seismic ground waves is negligible with respect to axial deformation. Thus, the problem of seismic wave interaction with pipelines containing round cracks and locally weak joints, can be simplified by focusing on ground movements in the axial pipeline direction.

2.6.2 Axial Component of Intersecting Shear Wave

In the near field of fault rupture, body wave effects on underground pipelines are generated primarily by S-waves that intersect the pipeline at an angle of incidence, γ_i, illustrated in Figure 2.16. The ground strain parallel to the pipeline, ε_g, is:

$$\varepsilon_g = V_\alpha / C_\alpha \tag{2.6}$$

in which V_a and C_a are the ground velocity and apparent wave propagation velocity, respectively, along the longitudinal axis of the pipeline, and C is the wave propagation velocity. Please note that:

$$C_\alpha = C / \sin \gamma_i \tag{2.7}$$

$$V_\alpha = V \cos \gamma_i \tag{2.8}$$

Combining Eqns. 2.6 through 2.8 provides the ground strain, ε_g, parallel to the pipeline, which is:

$$\varepsilon_g = \frac{V \sin 2\gamma_i}{2C} \tag{2.9}$$

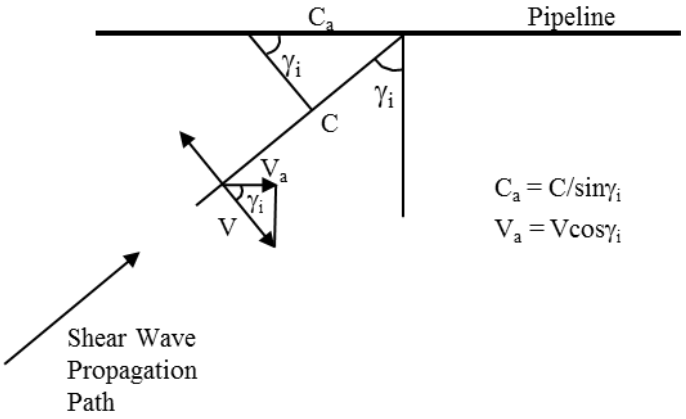

Figure 2.16. Pipeline Subjected to Shear Wave Propagation.

2.7 Dynamic Tests

2.7.1 Seismic Wave/Pipeline Interaction

The twin re-locatable shake tables in the Structural Engineering and Earthquake Simulation Laboratory (SEESL) of the University at Buffalo were utilized to perform quasi-static and dynamic tests on 9.14-m-long test sections of DI water pipelines retrofitted with CIPLs and CIPPs. The SEESL tests are described in detail by Zhong et al. (2015) and Zhong et al. (2014), and only the salient features are presented in this paper. Each specimen contained two lined DI joints, which were subjected to earthquake ground motions simultaneously and individually. The seismic movements for testing were derived from the FE simulations of S-wave interaction with pipelines reinforced with CIPLs and CIPPs, as discussed in the previous section.

Figure 2.17 shows a photo of the test setup. The seismic movements for testing were derived from FE simulations of S-wave interaction with pipelines reinforced with CIPLs (Bouziou, 2015). Strain gages, displacement transducers, accelerometers, differential pressure cells, and several video cameras were installed to monitor the

seismic response. Acoustic emission and ultrasonic guided waves inspections also were performed for each test to evaluate the extent of de-bonding between the DI pipe and liner. Asynchronous translational motions using lined joint displacement time records from the FE simulations were applied to each shake table to induce differential axial movements at the joints. The ground displacement amplitudes were scaled from about 50% to 200% of the Rinaldi Receiving Station recordings from the 1994 Northridge earthquake and from about 50% to 500% of the Joshua Tree recordings from the 1992 Landers earthquake. The scaled amplitudes were increased in stages until failure of the lining occurred.

2.7.2 Test Results

Figure 2.18 shows the axial force vs. joint opening response from a dynamic test performed with the dual shake table on a 150-mm diameter CIPL-reinforced DI pipeline. The test pipeline was subjected to Joshua Tree ("JT" in Fig. 2.18) joint displacement time records that were applied successively with amplitudes scaled in nine increments from 300% to 900% of the recorded motions.

For joint openings greater than 11-13 mm, the flexible CIPL was pinched between the spigot and the bell as the amplitude of axial displacement was reduced toward zero. This pinching was accompanied by a compressive force that is evident at low movement in the cyclic force vs. displacement plots. Pinching damages the lining and reduces its tensile capacity. The CIPL ruptured at approximately 75 kN in the seismic test, which is 15% less than the average rupture load measured during the axial tension

tests. The red oval in the plot shows unfolding of the pinched lining, and is indicative of test results in which the pinching mechanism was observed.

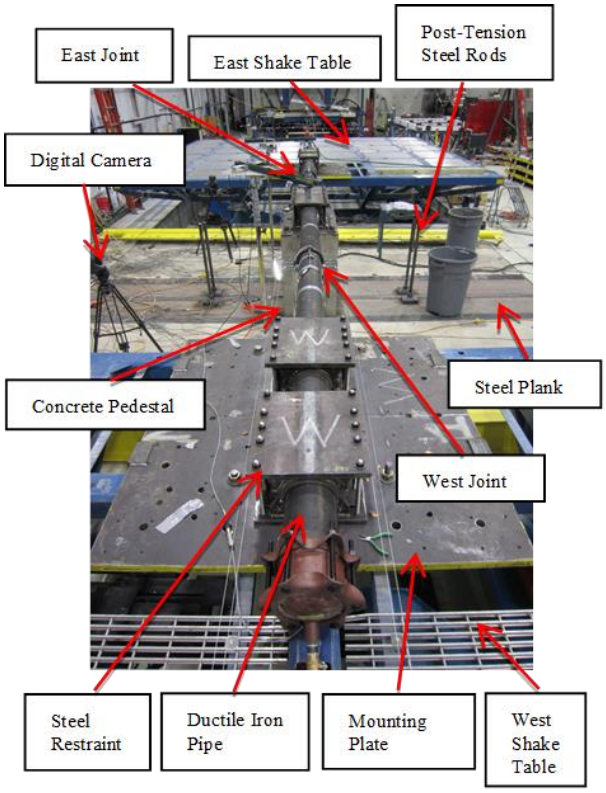

Figure 2.17. Photo of Dual Shake Table Test Setup to Evaluate the Dynamic Response of CIPL-Reinforced Pipelines.

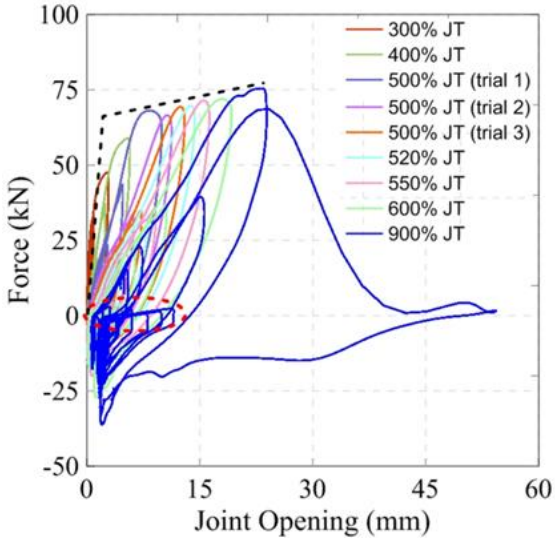

Figure 2.18. Axial Force vs. Displacement Plot from a Dual Shake Table Test on a CIPL-Reinforced Pipe (Zhong, 2014).

Figure 2.19 presents photos of a pinched CIPL during cyclic axial displacement tests performed at Cornell. The tests were performed by opening an initial 3-mm-wide gap in a 150-mm diameter DI pipe strengthened with a CIPL. The opening was expanded and closed in steps that increased the width of the opening by 3 mm each time displacement was applied. An internal water pressure of approximately 517 kPa was applied during the test. At openings of 13-15 mm the lining bulged outward at the gap and was pinched and compressed as the gap closed.

These test results show that CIPL-reinforced pipelines are vulnerable to seismic velocity pulses that can generate relatively large ground strains in the near field of fault rupture. Such ground strains can lead to opening and closing of round cracks and weak joints strengthened with CIPLs as seismic waves interact with the pipeline. The ground strain and attendant joint opening are directly related to the peak ground velocity and pulse period of the seismic waves.

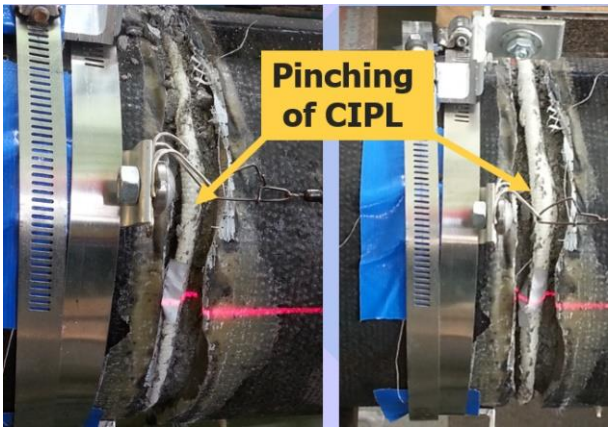

Figure 2.19. Photos of Pinched CIPL During Cyclic Axial Displacement Tests**.**

2.7.3 Simplified One-Dimensional Finite Element Model (1D FEM)

To evaluate the axial displacement across a weak joint or circumferential crack in a CIPL strengthened pipeline when subjected to ground wave interaction, a two-fold

approach to analytical and numerical modeling was undertaken. First, a simplified analytical model that accounts for seismic wave effects on a CIPL-reinforced aging pipeline was used to visualize the problem and provide an initial estimate of crack or gap opening. Then, more complex FE simulations were undertaken with the one-dimensional fracture propagation model described previously. It should be recognized that the fracture propagation model was calibrated with respect static axial tension tests. Nevertheless, full-scale experimental results on the dynamic and static performance of CIPL-reinforced pipelines (e.g., Bouziou, 2015; Zhong, 2015) show that the axial force vs joint opening results for a static axial tension test provides a close approximation of the backbone curve for the dynamic response of a similar pipeline reinforced with the same fiber reinforced lining system.

O'Rourke et al. (2005) developed a simplified model for the axial separation of a round crack or weak joint in response to S-wave interaction with an underground pipeline. The pipeline either side of the round crack or weak joint is assumed to have full capacity joints and behave as a continuous pipeline. This model provides a conservative assessment of axial separation because the round crack or weak joint is isolated from other defects, thus concentrating the effects of S wave interaction at a single defect. The concept is illustrated in Figure 2.20, which shows the ground strain, ε_g, as expressed in Eqn. 2.6 vs. distance, X, along the pipeline determined as the product of wave propagation time, t, and C_a as defined by Eqn. 2.7. It is further assumed that the pipeline is axially flexible with respect to ground strain accumulation such that no relative displacement occurs between the surrounding soil and the pipeline. Hence, the pipeline deforms as much as the surrounding ground, resulting in

$\varepsilon_p = \varepsilon_g$ everywhere the pipeline is continuous.

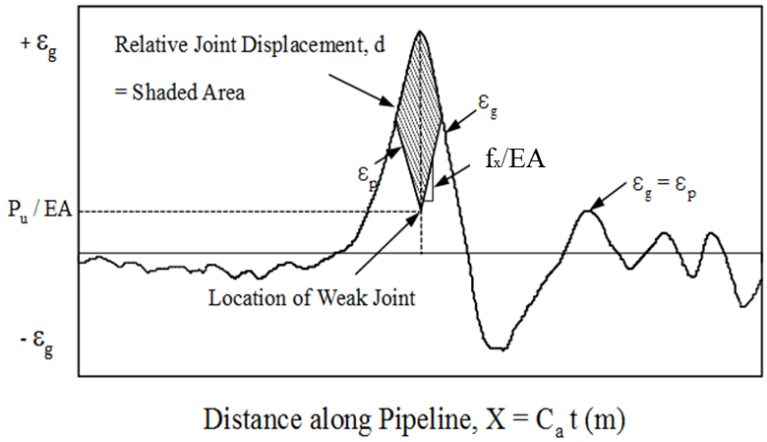

Figure 2.20. Relative Joint Displacement from Seismic Wave Interaction with a Pipeline Reinforced with a CIPL.

At a weak joint or round crack reinforced with a CIPL, the maximum axial force the pipeline can sustain, P_u, corresponds to a pullout strain, $\varepsilon_u = P_u/EA$, where E is the pipe material modulus, and A is the cross-sectional pipe area. After P_u occurs, the CIPL de-bonds, resulting in separation at the crack or weak joint that expands with little to no additional pullout resistance. As the seismic wave passes across the defect, strain in the pipeline on each side will accumulate linearly from $\varepsilon_p = \varepsilon_u = P_u/EA$ to $\varepsilon_p = \varepsilon_g$ at a slope of f_x/EA where f is the frictional resistance between pipe and soil. The shaded area in the Fig. 2.20 is the integration of the differential strain between pipeline and ground, which equals the crack or joint relative displacement. This model has been adapted to simulate the geometric nonlinear performance of weak joints or cracks at any position along the pipeline, account for both body and surface waves, and represent joints with bilinear force vs. displacement characteristics as well as welded slip joints subject to buckling (Shi & O'Rourke, 2008; Wang & O'Rourke, 2008).

A velocity pulse, similar to the one illustrated in Fig. 2.20, was modeled as a

sinusoidal half wave, with peak velocity, v_p, and period T, imposing tensile ground strain along the pipeline. The apparent wave propagation velocity in the direction parallel to the longitudinal axis of the pipeline, C_a, was calculated by Eqn. 2.7, assuming C=2.5 km/sec, which is the wave propagation velocity frequently assumed for California earthquakes and crustal conditions. The angle of incidence for seismic wave intersection with the pipeline, γ_i , was set equal to 45^o to impose maximum strain in the pipeline. The peak of the velocity pulse was assumed to coincide with the location of the defect to induce the maximum opening (O'Rourke et al., 2005). The simplified analyses were performed for peak ground velocities of 200 and 250 cm/s at pulse periods of 0.025, 0.05, 0.1, 0.2, 0.5, 0.75 and 1s. For the nominal 150-mm pipeline used in the full-scale experiments the values of P_u, E, and A used in the simplified analyses were 45 kN, 185 MPa and 40 cm^2, respectively.

The frictional force per pipeline unit length, f_x, was calculated in accordance with the recommendations of ASCE (1984) and O'Rourke et al. (2016) as follows:

$$f_x = \frac{\pi D}{2}(1+K_o)\bar{\gamma} H_c \tan\delta_s \tag{2.10}$$

where D is the outer pipe diameter, equal to 175 mm in our case, K_o is the "at-rest" earth pressure coefficient, H_c is the burial depth from the ground surface to center of the pipeline, and δ is the soil/pipeline interface friction angle.

Direct axial pull tests on nominal 150-mm DI pipe specimens reported by Wham et al. (2017) showed that δ_s ranges from $0.8\phi'$ to $1.0\phi'$. In this study, a value of 0.9ϕ' was selected. It was assumed that the pipe is buried at 1.22m depth to the top of the pipe (H = 1.3m), in partially saturated sand with total unit weight, $\bar{\gamma}$ of 17.6 kN/m^3 and

friction angle, ϕ' of 42^o. A value of 0.45 was used for K_o in accordance with values reported by O'Rourke and Druschel (1989).

To explore with greater detail and precision the relative axial displacement across a weak joint or round crack in a pipeline strengthened with a CIPL, the 1D FEM model described previously in Section 2.5 was used. That model requires a frictional force/unit length vs. relative soil/pipe axial displacement relationship. The maximum frictional force/unit length was calculated in the same way as for the simplified analytical model with Eqn. 2.10. Direct shear tests reported by O'Rourke at al. (1996) show that the maximum reaction along the pipeline axis, f_x, is mobilized at δ_x of approximately 1 mm, which was selected for the FEM analyses. The soil reaction springs (Fig. 2.10b) are assumed to follow a bilinear force vs. displacement relationship, as illustrated in Figure 2.21.

The velocity pulse was converted to displacement vs. distance records by assuming that $X=C_a\ t$, for which C_a is calculated in the same way as for the simplified analytical model. Then, the displacement vs. distance record was transferred into the soil reaction springs nodes, which conveyed ground movement to the pipeline. Again, the peak of the velocity pulse was assumed to coincide with the defect location and the angle of incidence for seismic wave intersection with the pipeline, γ_i, was set equal to 45^o to generate the maximum opening of the defect in the pipeline. Simulations were performed for various v_p of 250, 200, 150, 100, and 50 cm/s for pulse periods of 0.025, 0.05, 0.1, 0.2, 0.5, 0.75 and 1 s. The simulations were also performed for internal pressures of zero and 517 kPa. For each v_p vs. period there is a range of results pertaining to the effects of internal pressure. The upper and lower bound of the range

represents 565 zero and 517 kPa pipe pressure, respectively.

Additional description and discussion of the simplified models to account for crack/joint opening as a function of peak ground velocity and seismic wave orientation is provided in Appendix A. Of particular interest in Appendix A is a procedure to account for the combined uncertainty in seismic velocity and wave path.

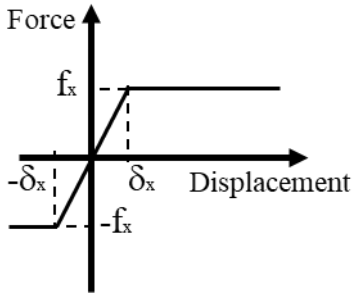

Figure 2.21. Bilinear Force vs. Displacement Relationship for Soil Reaction Springs Along Pipeline Axis.

During the simulations maximum axial tensile forces were checked to confirm that tensile failure of the lining does not precede pinching failure. In all cases the axial joint opening that corresponds to tensile failure was between 50 and 75 mm, well above the 11-13 mm needed to induce a pinching mechanism.

Figure 2.22 presents the results of the simulations in which the joint opening of a CIPL-reinforced pipeline with a round crack is plotted as a function of the pulse period for various peak ground velocities. For pulse periods exceeding approximately 0.2 s, the joint opening is virtually independent of the pulse period. Thus, for the great majority of near source velocity pulses, peak ground velocity, v_p, is the dominant ground motion parameter affecting CIPL-reinforced pipeline performance. Moreover, for v_p higher than 200 cm/s, CIPL pinching occurs, reducing the CIPL tensile capacity with a high potential for failure of the lining.

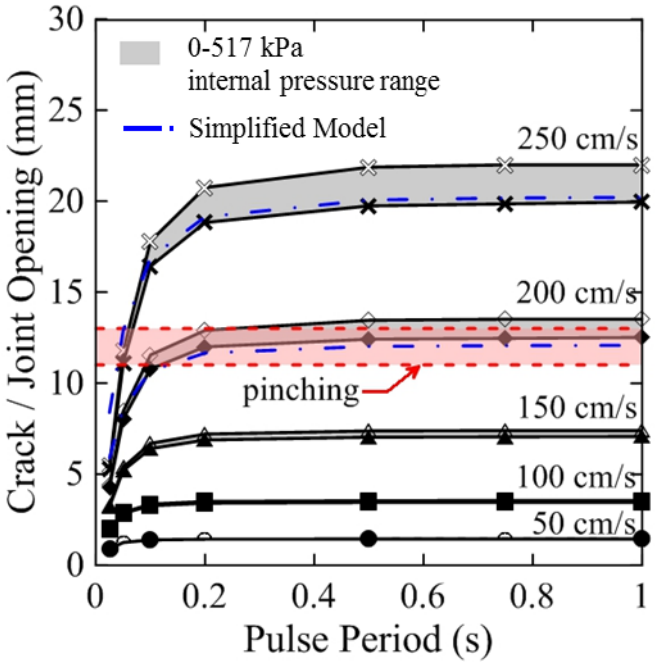

Figure 2.22. Relationship among Joint Opening, Peak Ground Velocity, and Period for a CIPL-Reinforced Pipeline with a Weak Joint or Round Crack.

Internal pipe pressure increases the axial resistance to opening of a defect. A pressure range from zero to 517 kPa, therefore, was evaluated to quantify the effect of pressure on gap formation. As shown by Figure 22, the influence of pipe pressure is relatively small, with approximately 10% reduction of joint/crack openings as the pressure increases from zero to 517 kPa. Experimental results (Bouziou, 2015; Zhong, 2015) show that a pinching mechanism occurs at pressures varying from approximately 110 kPa to 517 kPa. Even though protrusion of the lining into an opening crack requires some internal pressure, the experimental evidence suggests that this type of protrusion is initiated at pipeline pressures well below normal operating pressures for water distribution mains.

Fig. 2.22 also shows the results of the simplified analyses plotted for v_p equal to 200 and 250 cm/s and zero internal pressure. Although the simplified analyses were

performed for a rigid plastic model of the CIPL-reinforced crack opening, the results of these analyses compare favorably with those of finite element simulations.

For pulse periods exceeding 0.5 s, which are representative of many near source velocity pulses with forward directivity, Fig. 2.22 shows that pinching failure can be expected to initiate at a peak ground velocity of 200 cm/s. The threshold v_p = 200 cm/s will be related to a recurrence interval depending on the seismicity of the area, which allows for the probability of failure to be estimated. That probability can be used to decide on the seismic risk reduction benefits associated with the application CIPL technology to a specific pipeline or pipeline system.

2.8 Concluding Remarks

Experimental results summarized in this paper show that CIPLs can strengthen utilities substantially against both transient and permanent earthquake-induced ground deformation. Although in situ polymeric linings are used frequently to rehabilitate underground lifelines for daily use, they are not used in a systematic or formal way for earthquake protection. The research results presented in this paper help to correct one of the most critical deficiencies in current underground utility practice, namely the lack of verification of in situ trenchless lining technology for the retrofit of existing lifelines against earthquake effects. Key findings of the research reported in this paper are summarized as follows:

- Of critical importance for pipeline retrofitting is the de-bonding of the lining under axial extension of the pipeline. The de-bonding allows the lining to increase in length, thereby accommodating tensile ground movements. The de-bonding also

allows the linings to accommodate bending and rotation at the locations of defects, such as weak joints and round cracks in brittle pipelines and conduits.

- An important failure mode governing the response of underground pipelines strengthened with CIPLs to seismic ground waves is pinching of the lining during the dynamic opening and closing of round cracks and gaps in weak joints. A CIPL is relatively flexible and will protrude into a defect that opens during seismic wave interaction, thus subjecting the protruding portion of the lining to concentrated compression and damage as the defect closes. Full-scale dynamic and cyclic tests on the CIPL studied in this work show that the pinching mechanism is activated when the opening under transient motion exceeds 11-13 mm.

- A numerical model is described in this work that simulates the axial force vs. displacement response at weak joints and cracks in pipelines strengthened with CIPLs. The model accounts for de-bonding between the lining and pipe as the propagation of a Mode II fracture. It also accounts for enhanced frictional resistance mobilized by internal pipe pressure. The results of the numerical model are in good agreement with the full-scale test results both with respect to axial force vs. displacement as well as the relationship between the axial displacement across defects and the de-bonded length of the lining under variable pipe pressure.

- The simplified analytical and numerical models presented in this work for seismic wave interaction with pipelines reinforced with polymeric linings can be used to identify the peak ground velocity and pulse period combinations needed to exceed an axial displacement of 13 mm that activates the CIPL pinching mechanism. For pulse periods exceeding 0.2 s, the joint opening is virtually independent of the pulse period.

Thus, for the majority of near source velocity pulses, peak ground velocity, v_p, is the dominant ground motion parameter affecting CIPL-reinforced pipeline performance.

- Pinching failure can be expected to initiate at a peak ground velocity of 200 cm/s, which can be linked to a 50-year probability of failure. This probability helps to quantify the seismic risk reduction benefits for a particular pipeline or pipeline system.

The experimental work described in this paper was performed for 150-mm nominal diameter pipe and joints reinforced with a CIPL. The findings are directly applicable for pipelines with diameters of 100 to 250 mm, and generally applicable for pipe diameters of 300 to 600 mm. Pipelines with diameter less than or equal to 600 mm account for 93% of the US water distribution network (EPA, 2013). Additional experimental and analytical work is needed to address the seismic performance of larger diameter pipelines with hand-placed lining systems.

REFERENCES

Alfano, M., Lubineau, G. and Paulino, G.H. (2014). "Global Sensitivity Analysis in the Identification of Cohesive Models Using Full-field Kinematic Data." *International Journal of Solids and Structures,* 55:66-78.

Allouche, E., Alam, S., Simicevic, J., Sterling, R., Condit, W., Matthews, J. and Selvakumar, A. (2014). "A Pilot Study for Retrospective Evaluation of Cured-In-Place Pipe (CIPP) Rehabilitation of Municipal Gravity Sewers." *Tunneling and Underground Space Technology,* 39:82-93.

Ampiah, N., Fam, A. and Moore, I.D. (2010). "Effect of Wrinkles on the Circumferential Strength of a Cast-in-Place Composite Polymer Liner Used in Retrofitting Pressure Pipes." *Journal of Materials in Civil Engineering,* ASCE, 22(12): 1304-1314.

ASCE. (1984). "Guidelines for the Seismic Design of Oil and Gas Pipeline Systems." *Committee on Gas and Liquid Fuel Lifelines*, American Society of Civil Engineers ASCE, New York.

AWWA. (2011). "Cement-Mortar Lining of Water Pipelines in Place-4 in. (100 mm) and Larger." *Standard No. C602-11*, American Water Works Association, Denver, CO.

AWWA. (2001). "Rehabilitation of Water Mains." *Manual of Water Supply Practices M28, 2nd Ed.,* American Water Works Association, Denver, CO.

ASTM. (2014). "Standard Test Method for Tensile Properties of Polymer Matrix Composite Materials*." Standard No. ASTM D3039/D3039M-14,* American Society for Testing and Materials International, West Conshohocken, PA.

ASTM. (2002). "Standard Specification for Cured-in-Place Pipe Lining System for Rehabilitation of Metallic Gas Pipe." *Standard No. ASTM F2207-02*, American Society for Testing and Materials International, West Conshohocken, PA.

Bainbridge, K., Allouche, E.N. and Moore, I.D. (2005). "Laboratory Examination of Cured-in-Place Pressure Pipe Liner for Potable Water Distribution System." *NASTT No-Dig 2005,* Kissimmee, FL, Apr 24-27, Paper D-3-04, 10 p.

Barrenblatt, G.I. (1962). "The Mathematical Theory of Equilibrium Cracks in Brittle Fracture." *Advances in Applied Mechanics*, 7: 55-129.

Barsoom, J. (1995). "Trenchless Pipeline Technology." *ASTM Standardization News,* 23(5), May 1995.

Barton, N.R. (1973). “Review of a New Shear Strength Criterion for Rock Joints.” *Engineering Geology*, 7(4):287-332.

Boot, J.C., Javadi, A.A. and Toropova, I.L. (2004). “The Structural Performance of Polymeric Linings for Nominally Cylindrical Gravity Pipes.” *Journal of Thin-Wall Structures*, 42(8):1139-1160.

Bouziou, D. (2015). “Earthquake-Induced Ground Deformation Effects on Buried Pipelines.” PhD Dissertation: Cornell University.

Bouziou, D., Wham, B.P., O’Rourke, T.D., Stewart, H.E. and Palmer, M.C. (2012). “Earthquake Response and Rehabilitation of Critical Lifelines.”, *15th World Conference on Earthquake Engineering*, Sept. 24-28, Lisbon, Portugal.

Brown M.J.P., Moore I.D. and Fam, A. (2014). “Performance of a Cured-in-Place Pressure Pipe Liner Passing through a Pipe Section Without Structural Integrity.” *Tunneling and Underground Space Technology*, 42:87-95.

Bruzzone, A.A.G., Lonardo, P.M. and Diverio, G. (2007). “Experimental Characterization of Cured-in-Place Pipes (CIPP).” *International Society for Trenchless Technology, ISTT NoDig 2007*, Rome, Italy, Sep 2007.

Caggiano, A., Martinelli, E. and Faella, C. (2012). “A Fully-Analytical Approach for Modeling the Response of FRP Plates Bonded to a Brittle Substrate.” *International Journal of Solids and Structures*, 49(17):2291-2300.

Dugdale, D.S. (1960). “Yielding of Steel Sheets Containing Slits.” *Journal of the Mechanics and Physics of Solids*, 8(2):100-104.

Elices, M., Guinea, G.V., Gomez, J. and Planas, J. (2002). “The Cohesive Zone Model: Advantages, Limitations and Challenges.” *Engineering Fracture Mechanics*, 69(2):137-163.

EPA. (2013). “Primer on Condition Curves for Water Mains.” *EPA/600/R-13/080*, US Environmental Protection Agency, Columbus, OH.

Faella, C., Martinelli, E. and Nigro, E. (2009). “Direct vs. Indirect Method for Identifying FRP-to-Concrete Interface Relationships.” *Journal of Composites for Construction*, ASCE, 13(3):226-233.

Guan, S., Allouche, E., Baumert, M.I. and Bainbridge, K. (2007). “Long-Term Performance of CIPP Pressure Pipe Liner.” *NASTT No-Dig Conference 2007*, San Diego, CA, Apr 15-20, 2007, paper B-1-01.

Gustafsson, P.J. (1987). "Analysis of generalized Volkersen-Joints in terms of Nonlinear Fracture Mechanics." *Mechanical Behavior of Adhesive Joints*, Pluralis, Paris, 139-150.

Herzog, D.J., Bennett, A.J., Rahaim, K. and Schiro,J.D. (2007). "A Comparison of Cured-In-Place-Pipe (CIPP) Mechanical Properties - Laboratory vs. Field." *Composites & Polycon 2007*, Tampa, FL, Oct 17-19, 2007.

Hillerborg, A. Modeer, M. and Petterson, P-E. (1976). "Analysis of Crack Formation and Crack Growth in Concrete by means of Fracture Mechanics and Finite Elements." *Cement and Concrete Research*, 6: 773-782.

Jaganathan, A., Allouche, E. and Baumert, M. (2007). "Experimental and Numerical Evaluation of Impact of Folds on the Pressure Rating of CIPP Liners." *Tunneling and Underground Space Technology*, 22(5-6):666-678.

Jeon, S-S., O'Rourke, T.D. and Netrevali, A.N. (2004). "Repetitive Loading Effects on Cast Iron Pipelines with Cast-in-Place Lining Systems." *Journal of Transportation Engineerin*g, ASCE, 130(6):692-705.

Kramer, S.R., McDonald, W.J. and Thomson, J.C. (1992). *An Introduction to Trenchless Technology*. Van Nostrand Reinhold, New York, NY.

Netravali, A.N., O'Rourke, T.D., Shaw, S.K. and Bond, T. (2003). "Evaluation of Starline 2000-PSE Cured-In-Place Lining System for Cast Iron Gas Distribution Pipelines." *Final Report Contract No. 39802*, prepared for New York Gas Group, Apr., Cornell University, Ithaca, NY.

Netravali, A.N., O'Rourke, T.D., Gerretisen, K.I., Singh, Y.P., Jeon, S-S. and Zhao, D. (2000). "Advanced Pipeline Support and Stabilized Backfill for Gas Mains." *Final Report Contract No. 31120,* prepared for New York Gas Group, Mar., 227 p., Cornell University, Ithaca, NY.

O'Rourke, T.D., Jung, J.K. and Argyrou, C. (2016). "Underground Pipeline Response to Earthquake-Induced Ground Deformation." *Soil Dynamics and Earthquake Engineering*, 91:272-283.

O'Rourke, T.D., Jezerski, J.M., Olson, N.A., Bonneau, A.L., Palmer, M.C., Stewart, H.E., O'Rourke, M. J. and Abdoun, T. (2008). "Geotechnics of Pipeline System Response to Earthquakes." Keynote Paper, *Geotechnical Earthquake Engineering and Soil Dynamics IV* (GEESD) Sacramento, CA, May.

O'Rourke, T.D., Wang, Y. and Shi, P. (2005). "Advances in Lifeline Earthquake Engineering." *13th World Conference on Earthquake Engineering*, Vancouver, British Columbia, Canada.

O'Rourke, T.D., Netravali, A.N., Pendharkar, S.M., Tonkinson, A., Chaudhuri, D. and Toparak, S. (1996). "Evaluating Service Life of Anaerobic Joint Sealing Products and Techniques." *Final Report, Report No. GRI-96/0318,* Prepared for Gas Research Institute, Contract No. 5093-207-2798, Cornell University, Ithaca, NY.

O'Rourke, T.D. and Druschel, S.J. (1989). "Improved Anchoring Practices for Plastic Gas Distribution Pipelines", *Final Report prepared for New York Gas Group,* Cornell University, Ithaca, NY.

O'Rourke, M.J. and Liu, J.X. (2012). "Seismic Design of Buried and Offshore Pipelines." *Monograph No. 4:* Multidisciplinary Center for Earthquake Engineering Research, Buffalo, NY.

Park, K. and Paulino, G.H. (2013). "Cohesive Zone models: a Critical Review of Traction-Separation Relationships across Fracture Surfaces." *Applied Mechanics Reviews,* 64(6):060802.

Patton, F.D. (1966). "Multiple Modes of Shear Failure in Rock." *1st Congress in Rock Mechanics,* Lisbon, 1:509-513.

PPM. (2011). "3D view of Starline2000®." Progressive Pipeline Management. Available from http://progressivepipe.com/. [accessed 10 September 2013].

Sabnis, G.M., Harris, H.G., White R.N. and Saeed Mirza, M. (1983). "Structural Modeling and Experimental Techniques." Prentice Hall Civil Engineering and Engineering Mechanics Series, Englewood Cliffs, NJ, USA.

Shi, P. and O'Rourke, T.D. (2008). "Seismic Response Modeling of Water Supply Systems." *Technical Report MCEER-08-0016,* Multidisciplinary Center for Earthquake Engineering Research, Buffalo, NY.

Stewart, H.E., O'Rourke, T.D., Wham, B.P., Netravali, A., Argyrou, C., Zeng, X. and Bond, T.K. (2015). "Performance Testing of Field-Aged Cured-in-Place Liners (CIPL) for Cast Iron Piping." *Final Report prepared for NYSEARCH/Northeast Gas Association,* December, Cornell University, Ithaca, NY.

Spring, D.W. and Paulino, G.H. (2014). "A Growing Library of Three-Dimensional Cohesive Elements." *Engineering Fracture Mechanics,* Elsevier, 126:190-216.

Taljsten, B. (1996). "Strengthening of Concrete Prisms Using the Plate-Bonding Technique." *International Journal of Fracture,* 82(3):253-266.

Tashiro, C. and Tatibana, S. (1983). "Bond Strength between C_3S Paste and Iron, Copper or Zinc Wire and Microstructure of Interface." *Cement and Concrete Research*, 13(3):377-382.

Turon, A., Camanho, P.P., Costa, J. and Davila, C.G. (2006). "A Damage Model for the Simulation of Delamination in Advanced Composites Under Variable-Mode Loading." *Mechanics of Materials*, 38(11):1072-1089.

Turon, A., Camanho, P.P. Davila, C.G. and Costa, J. (2007). "An Engineering Solution for Mesh Size Effects in the Simulation of Delamination Using Cohesive Zone Models." *Engineering Fracture Mechanics*, 74(10):1665-1682.

Tvergaard, V. and Hutchinson, J.W. (1992). "The Relation between Crack Growth Resistance and Fracture Process Parameters in Elastic-Plastic Solids." *Journal of the Mechanics and Physics of Solids*, 40(6):1377-1392.

Wang, Y. and O'Rourke, T.D. (2008). "Seismic Performance Evaluation of Water Supply Systems." *Technical Report MCEER-08-0015*, Multidisciplinary Center for Earthquake Engineering Research, Buffalo, NY.

Wham, B.P., Pariya-Ekkasut, C., Argyrou, C., Lederman, A., O'Rourke, T.D. and Stewart, H.E. (2017). "Experimental Characterization of Hazard-Resilient Ductile Iron Pipe Soil/Structure Interaction under Axial Displacement." *Congress on Technical Advancement*, Sept. 10-13, Duluth, MN, available at: https://ascelibrary.org/doi/pdf/10.1061/9780784481028.013.

Wham, B.P. and O'Rourke, T.D. (2015). "Jointed Pipeline Response to Large Ground Deformation." *Journal of Pipeline Systems Engineering and Practice*, 10.1061/(ASCE)PS.1949-1204.0000207.

Zhong, Z., Filiatraut, A. and Aref A. (2017a). "Numerical Simulation and Seismic Performance Evaluation of Buried Pipelines Rehabilitated with Cured-in-place Pipe Liner under Seismic Wave Propagation." *Earthquake Engineering and Structural Dynamics*, International Association for Earthquake Engineering, 46(5):811-829.

Zhong, Z., Filiatraut, A. and Aref A. (2017b). "Experimental Performance Evaluation of Pipelines Rehabilitated with Cured-in-place Pipe Liner Under Earthquake Transient Ground Deformations." *Journal of Infrastructure Systems*, 10.1061/(ASCE)IS.1943-555X.0000326.

Zhong, Z., Filiatraut, A. and Aref A. (2015). "Seismic Performance Evaluation of Buried Pipelines Retrofitted with Cured-in-Place Pipe Liner Technology under Near-Fault Ground Motions." *Structures Congress*, April 23-25, Portland, Oregon, available at: https://ascelibrary.org/doi/10.1061/9780784479117.164.

Zhong, Z. (2014). "Earthquake Response and Rehabilitation of Critical Underground Lifelines Reinforced with Cured-in-Place Pipe Liner Technologies under Transient Ground Deformations." PhD Dissertation: University at Buffalo.

Zhong, Z., Bouziou D., Wham B., Filiatraut, A., Aref A., O'Rourke, T.D. and Stewart, H.E. (2014). "Seismic Testing of Critical Lifelines Rehabilitated with Cured-in-Place Pipeline Lining Technology." *Journal of Earthquake Engineering*, 18(6):964-985.

CHAPTER 3

LARGE-SCALE FAULT RUPTURE TESTS ON PIPELINES REINFORCED WITH CURED-IN-PLACE LININGS

Abstract

Cured-in-place linings (CIPLs) are flexible fiber reinforced polymer linings used to rehabilitate aging pipelines in situ. They also can strengthen utilities against transient and permanent ground deformation caused by earthquakes, thus providing added value through seismic retrofitting. This paper presents the results of full-scale fault rupture tests to characterize the de-bonding, axial elongation, and bending performance of pipelines with round cracks and weak joints strengthened with CIPLs and subject to abrupt ground deformation. The results of finite element simulations are compared with the experimental fault rupture response of jointed pipelines with and without CIPL reinforcement. The results of a numerical model that accounts for de-bonding between the lining and pipe as Mode II fracture propagation are in good agreement with full-scale fault rupture test results. Recommendations are made for applying the modeling and experimental results for in situ strengthening of underground utilities against earthquakes and other sources of permanent ground deformation.

3.1 Introduction

Cured-in-place linings and pipes (CIPLs and CIPPs, respectively) are reinforced polymer linings installed remotely inside existing, underground pipelines and conduits with minimum environmental disturbance through trenchless construction procedures (e.g. Brown et al., 2014; Ampiah et al., 2010; Kramer et al., 1992). Although these

cured in place systems are used primarily to rehabilitate underground lifelines for daily use, they also allow for in situ retrofitting of underground utilities against earthquake-induced transient and permanent ground deformation (Zhong et al. 2017a, 2017b, 2014; Bouziou, 2015; Zhong, 2014; Bouziou et al., 2012). This paper focuses on the performance of CIPL-reinforced pipelines when subject to fault rupture in soil. Fault rupture is also representative of the most severe ground deformation that occurs along the margins of liquefaction-induced lateral spreads and landslides.

Netravali et al. (2003, 2000) and Jeon et al. (2004) have shown through experimental and numerical evaluations that CIPLs are effective for in situ strengthening of cast iron (CI) pipelines against the effects of excavation-induced ground deformation. Large-scale laboratory tests reported by Jeon et al. (2004) simulated the effects of soil settlement caused by adjacent, parallel trench construction on CI pipelines. During those tests, a CIPL-reinforced CI pipeline with a round crack was able to accommodate excavation-induced soil movements as large as 250 mm and then sustain an additional one million cycles of traffic-induced deformation without leakage. The results of large-scale experiments with twin shake tables have been reported by Zhong et al. (2014) in which pipelines reinforced with CIPLs were subjected to quasi-static and seismic ground motions. The retrofitted pipelines were able to accommodate high intensity transient ground motions, consistent with some of the highest near-field ground velocities ever measured.

This paper begins with a description of the CIPL and ductile iron (DI) pipeline used in the experimental and numerical work. The experimental procedures for large-scale fault rupture tests are described, including information about the partially

saturated sand used in the tests. The results of three fault rupture tests are presented and discussed. A numerical model that accounts for de-bonding between the lining and pipe as the propagation of a Mode II fracture is described, and the results of this model are shown to compare favorably with the experimental measurements. Recommendations are made for applying the modeling and experimental results for in situ strengthening of underground utilities against earthquakes and other sources of permanent ground deformation.

3.2 Test Specimens

AWWA (2001) classifies a cured-in-place polymeric lining as structural, semi-structural, or non-structural, depending on its ability to carry internal pressure and external loads. A CIPL is a flexible semi-structural lining. The CIPL used in this study is commercially available as Starline2000®, which is installed by Progressive Pipeline Management, Ltd., with properties and installation methods that conform to ASTM F2207-02 (2002).

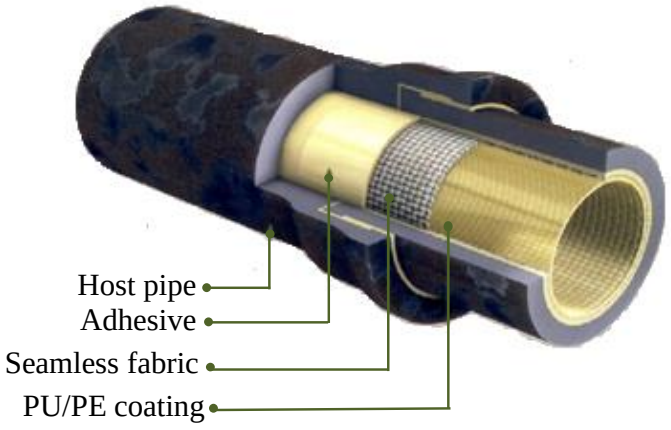

Figure 3.1. Three-Dimensional View of Cured-In-Place Lining (Progressive Pipeline Management, 2010).

As shown in Figure 3.1, the lining consists of a seamless woven polyester hose with a thin interior polyurethane layer. The polyester hose is saturated with a two-part polyurethane that bonds the hose to the inside surface of the pipe. CIPL installation is performed by the "inversion method," in which the polyurethane-impregnated lining is inverted into an existing, previously cleaned pipe using either heated air or water to drive the inversion process and accelerate curing. The woven polyester hose is composed of yarns that are orthogonal to each other and are oriented along its axial and hoop directions.

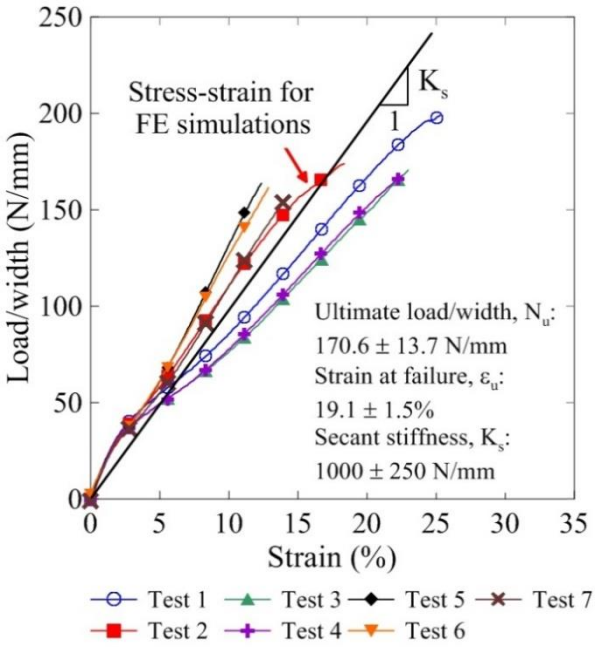

Figure 3.2. Tensile Test Results for CIPL Specimens Oriented in the Axial Direction (Stewart et al., 2015).

Tension test results are reported by Stewart et al. (2015) for CIPL samples, 15-mm-wide and 200-mm-long, performed using a modified ASTM D3039/3039M-14 (2014), with tension expressed as load/width in accordance with ASTM F2207-02 (2002). A CIPL is a composite that is relatively thin with a potentially variable wall

thickness. For this type of material, it is appropriate to express tensile load as load/width. Figure 3.2 shows the load/width vs. strain plots for specimens oriented in the axial direction. The data follow an approximately linear relationship until failure, with mean and standard deviation of strength, strain at failure, and secant stiffness of 170.6 ± 13.7 N/mm, 19.1 ± 1.5 %, and 1000 ± 250 N/mm, respectively.

The linings were installed in 150-mm-diameter DI pipe specimens manufactured by the U.S. Pipe and Foundry Co. (US Pipe). The pipe outer diameter and wall thickness were 175 mm and 7.6 mm, respectively. This was typical of DI pipe used commonly in water distribution systems. The modulus of elasticity, tensile strength and strain at rupture of the DI are 185 GPa, 417 MPa and 10.4 % (Wham and O'Rourke 2015), respectively, as determined in accordance with the ASTM E8/E8M 13a (2013). All specimens had a 3.3-mm-thick interior cement mortar lining in conformance with AWWA C602-11 (2011). Figure 3.3 shows a cross-section of a push-on bell-and-spigot joint. During field installation the spigot is inserted into the bell until contact is perceived between the spigot and bell, resulting typically in a small gap of 3-6 mm between them. The force required to extract the fully inserted spigot is very low, in the range of 0.8 ± 0.1 kN (Wham and O'Rourke 2015). Since the resistance against both axial pullout and rotation below 5° is very low with a full circumferential gap between the end of the spigot and back of the bell, the DI joints also were representative of CI pipelines with weak joints and round cracks, thereby representing pipelines with defects due to stress concentrations and aging.

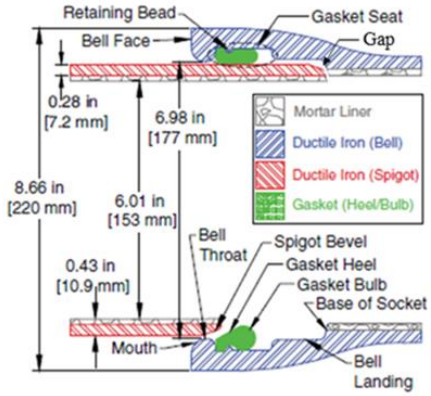

Figure 3.3. Cross-Section of a Typical 150-mm Push-on Joint (Wham & O'Rourke, 2015).

3.3 Fault Rupture Tests

Figure 3.4 shows the split-box test basin at Cornell University, capable of tests with 90 metric tons of partially saturated sand and 1.2 m of strike slip. Displacement is generated by four hydraulic actuators, two of which have load capacities of 445 kN tension/650 kN compression and one-way stroke of 1.28 m., and two of which have load capacities of 295 kN tension/500 kN compression and one-way stroke of 1.82 m. The actuators were operated during the tests at a displacement rate of 305 mm/min.

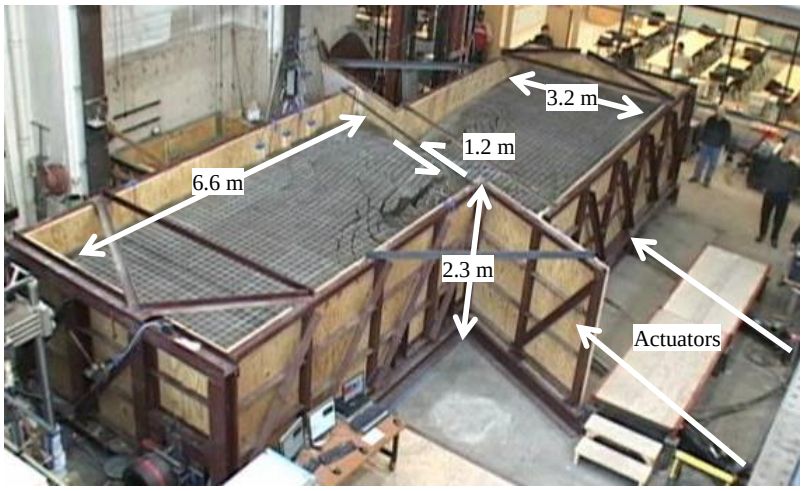

Figure 3.4. Large-Scale Split-Box Test Basin at Cornell University (https://lifelines.cee.cornell.edu/).

3.3.1 Soil Characteristics

The soil for the large-scale experiments is an angular to subangular glacio-fluvial sand, with a grain size distribution as shown in Figure 3.5. Examination assisted by microscope shows approximately 71% by weight of siltstone, fine-grained sandstone, shale, and limestone fragments, and 29% quartz grains. The mean grain size, D_{50}, for the soil is 0.59 mm, and the coefficient of uniformity, C_u, is 3.35.

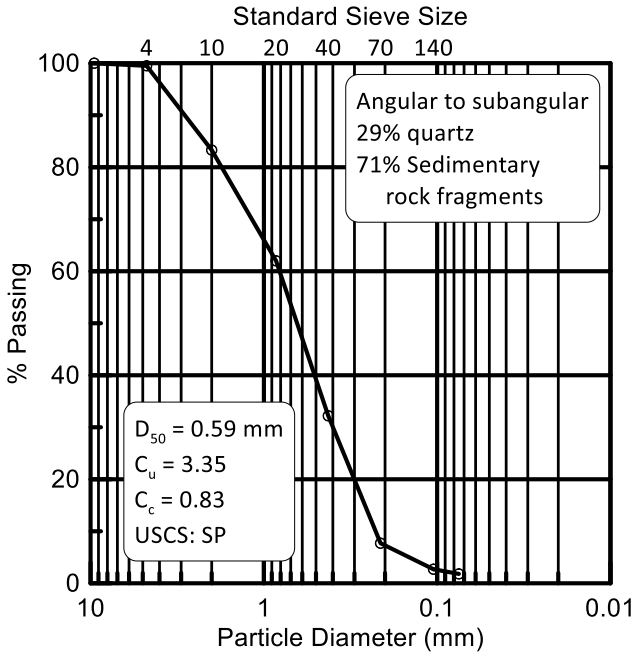

Figure 3.5. Grain Size Distribution for Large-Scale Test Sand.

The partially saturated sand was placed in 200-mm lifts, each of which was compacted with two passes of a gasoline powered plate tamper. Dry unit weight, γ_d was measured in situ using a nuclear density gage according to ASTM D2216-10 (2010b), and water content was measured in situ according to ASTM D6938-10 (2010a). The target value of dry density was $\gamma_{dry} = 16.7$ kN/m^3, and the target value of moisture content was w = 4.0 %, corresponding to a direct shear friction angle of approximately 42º. Water contents during testing were between 3.5% and 4.5%,

equivalent to the residual water content of the soil. A detailed discussion of the sand strength, including Mohr-Coulomb strength characterization for dry and partially saturated sand is provided by O'Rourke (2010).

3.3.2 Test Set Up and Procedure

Figures 3.6a and 3.6b show plan views of test set ups for the DI pipe and pipe joint centered on the fault rupture, respectively. The pipe centered test (Fig. 3.6a) was used for an unlined and lined pipeline, and the joint centered test (Fig. 3.6b) was used only for a lined pipeline. Pipe centered and joint centered configurations were used to bound the geometric conditions that apply for a jointed pipeline crossing a single plane of ground rupture. The size of the zone containing soil for each test and pipeline configuration within that zone were selected through finite element analyses, as described in the next section. The extent of the soil zone with respect to the pipeline was chosen such that the simulated bending and axial responses of the pipeline were not affected when the size of the soil zone was increased. For the joint centered test this approach resulted in a relatively small length of pipeline south of the fault rupture that was nonetheless suitable for developing pipeline bending and axial response north of the fault rupture unaffected by the boundaries of the test basin. The pipeline length from joint to joint was 3.7 m, typical of a CI pipeline. The pipe invert was located at 200 mm from the bottom of the soil box, and the depth to the top of pipe was 760 mm to be consistent with conditions of cover and backfill bedding frequently used in the field. During testing the pipeline had an internal water pressure of 520 kPa.

The instrumentation consisted of 72 strain gages at 21 locations and 84 strain

gages at 24 locations (gage planes) along the pipeline for the lined pipe centered and lined joint centered test, respectively. For the unlined pipeline, 25 strain gages were installed at 7 locations. Strain gage locations were chosen on the basis of the expected deformed shape and axial behavior of the pipeline as estimated by finite element analyses during the design phase for the tests. Strain gages were generally positioned at the crown, invert and the springlines on each side of the pipe. Load cells were used at the ends of the pipeline to measure axial forces, and strain gage stations outside the zone of soil placement in the joint centered test were used to complement the load cell measurements. Three linear variable differential transformers (LVDTs) were placed at each joint to measure the joint pullout and rotation. After the LVDTs were installed, a protective shielding was wrapped and secured around the joint.

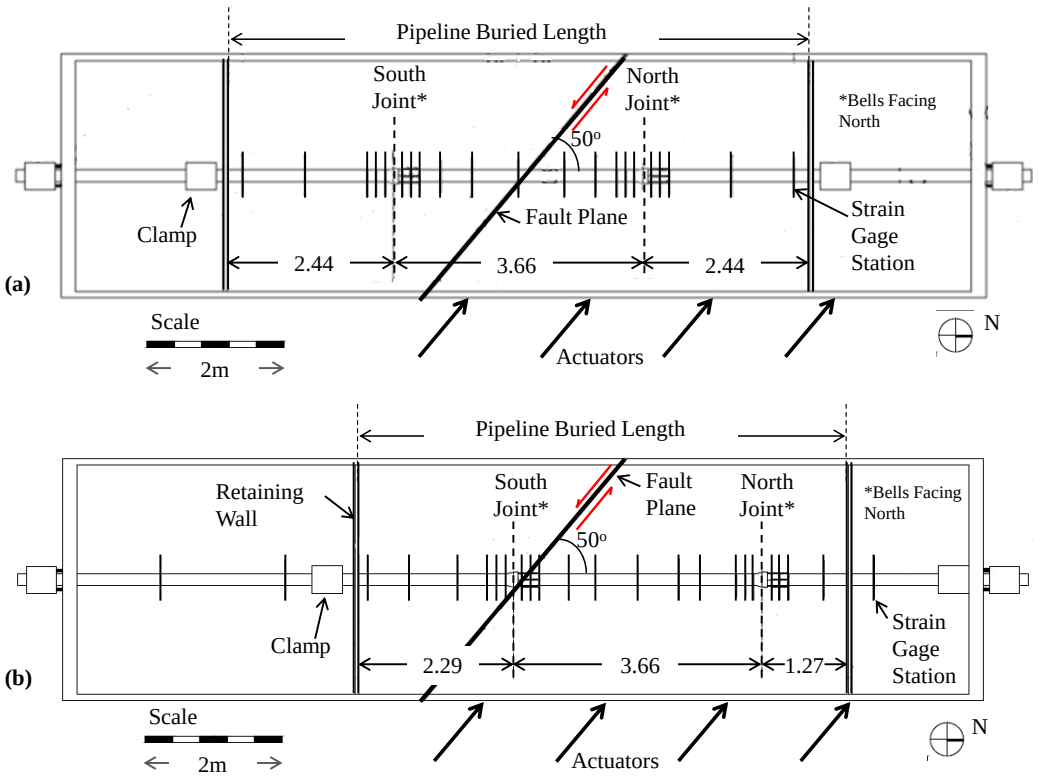

Figure 3.6. Plan view of (a) Pipe Centered and (b) Joint Centered Large-Scale Fault Rupture Test Setup.

3.4 Numerical Modeling

3.4.1 Two-Dimensional Finite Element Model (2D FEM) for Jointed Pipeline

The 2D FEM developed with the software ABAQUS (v6.13-2) conforms to the ASCE guidelines (1984), as illustrated in Figure 3.7a, with the pipeline represented by beam elements and soil reaction by independent springs in the pipeline longitudinal (frictional component) and transverse directions (horizontal and/or lateral). In the case of strike-slip faulting, only the longitudinal and transverse horizontal components are modeled. Each spring is assumed to follow bilinear force vs. displacement relationship, as shown in Figure 3.7c. At joint locations, three independent springs are used to represent the joint behavior, as shown in Figure 3.7b. Details on the calibration of the soil reaction and joint springs are provided later in this section.

3.4.2 Soil Reaction Springs in the Transverse Horizontal Direction

Jung et al. (2016) provide the dimensionless lateral force per unit pipe length, N_{qH}, for sands of different densities and any pipeline displacement orientation. The maximum lateral force per unit pipe length, f_{ym}, is calculated by the following expression:

$$f_{ym} = N_{qH}\,\bar{\gamma}\,H_c D \tag{3.1}$$

where $\bar{\gamma}$ is the soil effective unit weight, D is the pipe outer diameter and H_c is the burial depth from the ground surface to pipe centerline. For the fault rupture tests, D and H_c are equal to 154 mm and 850 mm, respectively. Since the pipeline was buried in partially saturated sand, the total unit weight, equal to 17.6 kN/m^3, was used. The N_{qH} vs. H_c/D relationship for partially saturated sand provided by Jung et al. (2016)

was used. The resulting N_{qH} and f_{ym} are equal to 11.5 and 30.1 kN/m, respectively.

According to Jung et al. (2016) the bilinear representation of the lateral soil reaction force, f_y, vs. relative soil/pipe displacement, δ_y, is defined by a linear relationship to f_{ym}, at a relative soil/pipe displacement of δ_{ym}, given by the following expression:

$$\delta_{ym} = 0.014 H_c \tag{3.2}$$

yielding a value of δ_{ym} equal to 11.9 mm for the fault rupture tests.

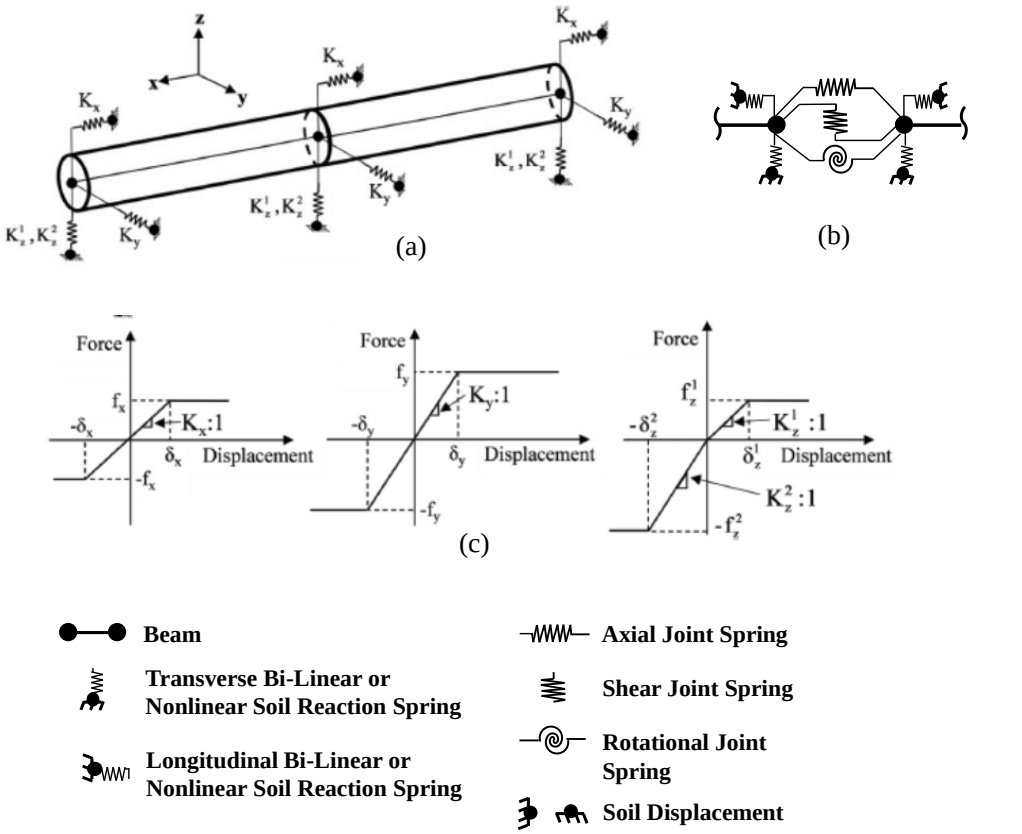

Figure 3.7. Schematic of FE Model (ASCE, 1984): (a) Pipeline with frictional, transverse horizontal and transverse vertical component of soil reaction (Bouziou, 2015), (b) Detail for Jointed Pipeline Simulation and (c) Bilinear force vs. displacement relationships at pipe-soil interface (Bouziou, 2015).

3.4.3 Soil Reaction Springs in the Longitudinal Direction

The maximum frictional force per pipeline unit length for at-rest conditions, f_{xo}, is calculated by the following expression (ASCE, 1984):

$$f_{xo} = \frac{\pi D}{2}(1 + K_o)\bar{\gamma} H_c \tan\delta_s \tag{3.3}$$

where D, H_c and $\bar{\gamma}$ are defined earlier in this section, K_o is the at-rest earth pressure coefficient, and δ_s is the soil/pipeline interface friction angle. Direct axial pull tests on 150-mm DI pipe specimens reported by Wham et al. (2017) showed that δ_s ranges from $0.8\phi'$ to $1.0\phi'$ for a sand/DI interface, where ϕ' is the effective friction angle. In this study, a value of $0.9\phi'$ was selected for the numerical simulations. A value of 0.45 was used for K_o in accordance with values reported by O'Rourke and Druschel (1989), as measured during pipe pullout tests through sand. Eqn. (3.3) yields a frictional force, f_{xo}, equal to 4.7 kN/m for the fault rupture tests. Direct shear tests reported by O'Rourke et al. (1996) showed that f_{xo} is mobilized at δ_x equal to approximately 1 mm, which was selected for the numerical analyses.

When the buried pipeline is subjected to transverse deformations, the at-rest conditions are disturbed and the frictional forces can no longer be determined by Eqn. (3.3). O'Rourke et al. (2016) present a modified 2D FE model that accounts for coupled normal and frictional forces on the pipeline through a Coulomb friction law. O'Rourke et al. (2016) also developed a correction factor to account for the actual frictional forces around the pipe circumference during pipeline lateral displacement, which are calculated by the expression:

$$f_{xu} = f_y \tan\delta_s \left(\frac{f_T}{f_A} \right) \tag{3.4}$$

where f_y is the lateral force per pipeline unit length, with maximum value f_{ym} determined by Eqn. (3.1), δ_s is the soil/pipeline interface friction angle and f_T/f_A is the correction factor for the coefficient of friction as defined by O'Rourke et al. (2016). Eq (3.4) yields a maximum frictional force of 19.9 kN/m for the ground rupture tests.

3.4.4 Joint Modeling

The pipeline joint behavior is simulated by three independent springs, as shown in Fig. 3.7b, to cover the joint behavior under axial pullout, rotation and shear deformation. The moment vs. rotation relationship for the rotational spring was determined by full-scale four-point bending tests on unlined and CIPL-reinforced joints. For the unlined DI bell-and-spigot joint, no resistance to rotation was assumed until 5^o of rotation (Wham and O'Rourke, 2015). For the CIPL-reinforced joint, the bilinear joint moment vs. rotation relationship shown in Figure 3.14b was used in the FE simulations. The shear joint spring was very stiff to represent direct contact between the spigot and the bell.

Consistent with the results of Wham and O'Rourke (2015), a rigid-plastic force vs. displacement relationship for the unlined DI joint was assumed for the axial joint spring, with maximum force equal to 0.9 kN at approximately 50 mm of opening, when the spigot pulls completely out of the bell. For the CIPL-reinforced joint, a different approach was used to model the response under axial deformations, which is discussed next.

3.4.5 Model for CIPL-Reinforced Pipe under Axial Deformation

Argyrou et al. (2017) developed a numerical model for CIPL-reinforced pipelines under axial tension based on linear elastic fracture mechanics models for fiber reinforced plastic (FRP)-to concrete interfaces (Faella et al., 2009; Caggiano et al., 2012), in which the pipe and CIPL are represented by beam elements with nonlinear springs for the pipe/lining interface. Longitudinal shear transfer along the soil/pipe interface is modeled by a bilinear force vs. displacement relationship, similar to the f_x relationship in Fig. 3.7c.

The pipe/CIPL interface shear strength, τ, is a function of the pipe/CIPL relative slip, δ:

$$\tau = \tau_c(\delta) + \tau_f(\delta) \tag{3.5}$$

where τ_c and τ_f are the cohesive and frictional components of the strength, respectively.

The cohesive component, τ_c, represents the pipe/CIPL interface bond strength under zero internal pressure. As shown in Figure 3.9a, τ_c is characterized by a maximum apparent bond strength, τ_{max}, and a maximum slip at zero bond strength, δ_u, which is in turn used to characterize the nonlinear springs for the pipe/CIPL interface shown in Fig. 3.8. The area below the τ_c vs. δ curve represents the fracture energy, G_f, i.e., the energy required to bring a unit area of a bonded surface to complete fracture in Mode II. As illustrated in Figure 3.9b, the pipe/CIPL interface is composed of both pipe/mortar and mortar/CIPL interfaces and the mortar layer. When axial forces are applied to the CIPL-reinforced pipe under zero pressure, the mortar is subjected to simple shear. As shear increases, the radius of Mohr circle likewise increases until it becomes equal to a) mortar/DI pipe interface shear capacity τ_{b1} (point 2), b)

mortar/CIPL interface shear capacity τ_{b2} (point 2) or c) mortar tensile capacity f_{tm} (point 1). Argyrou et al. (2017) show that f_{tm} and τ_{b1} are virtually identical and that τ_{max} is well represented as 2.8 MPa, which is 9% of the minimum mortar compressive strength specified in AWWA C602-11 (2011).

The fracture energy, G_f, developed with linear elastic fracture mechanics (e.g. Taljsten, 1996) for the maximum force, P, sustained by an FRP-to-concrete interface that exceeds the critical bond length is:

$$P = \pi D\sqrt{2G_f E_L t_L} = \pi D\sqrt{2G_f K_S} \tag{3.6}$$

where D_L, E_L, t_L, and K_S are the outer diameter, elastic modulus, CIPL thickness, and linear secant stiffness, expressed in terms of load/width, for the CIPL tensile test specimens, respectively. Axial tension tests show that under zero internal pressure, de-bonding propagation occurs at a constant force P equal to 45-50 kN (Argyrou et al. 2017). The CIPL outer diameter is equal to 150 mm, and the linear secant stiffness K_S is 1000 N/mm. Using G_f from Eqn. 3.6 and τ_{max} = 2.8 MPa, δ_u = 3 mm.

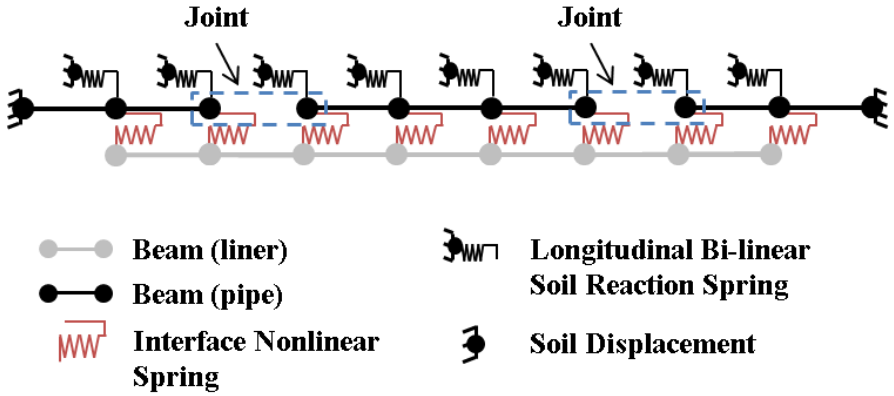

Figure 3.8. Soil-Pipeline Interaction Model for CIPL-reinforced Jointed Pipelines under Axial Soil Displacement.

The frictional component, τ_f, is activated in the presence of internal pipe pressure when relative slip between the pipe and CIPL is initiated. Relative slip causes the mortar along the interface to break up, creating interlocking rough surfaces analogous to a rock discontinuity. Using the model developed by Patton (1996), the additional shear resistance generated by the interaction of fragmented pieces of mortar, was characterized to evaluate $\tau_f(\delta)$ as explained by Argyrou et al. (2017).

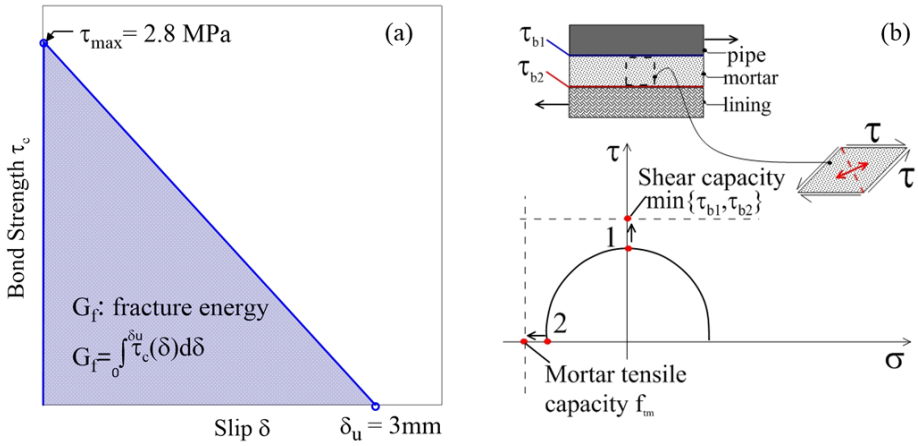

Figure 3.9. Soil-Pipeline Interaction Model for CIPL-reinforced Jointed Pipelines under Axial Soil Displacement: (a) Apparent Cohesion vs. Slip for the Pipe/CIPL Interface (b) Maximum Interface Apparent Cohesion.

3.5 Experimental vs. Numerical Results

It is well known that the response of underground pipelines to ground deformation can be decomposed into bending and axial deformation (e.g. O'Rourke et al., 2008). This decomposition applies to both experimental data and numerical simulation results. Since the fracture propagation model for de-bonding is a 1D model in the axial direction, the simulation of pipeline response to fault rupture with this model involves a two-fold process by which 1) the soil/pipeline interaction modeling illustrated in Fig. 3.7 is used to simulate the pipeline response under lateral deformation, and 2) the

results of this modeling are used to apply increased longitudinal frictional forces along the appropriate pipeline sections when using the fracture propagation model illustrated in Fig. 3.8.

This section compares the numerical and experimental results for the fault rupture tests with respect to bending moments, axial forces, axial joint movement, and joint moments and rotations. In each of the following subsections the experimental and numerical results are compared side-by-side for the unlined pipeline and both the pipe centered and joint centered lined pipeline configurations. The negative distances along horizontal axis of the bending moment and axial force plots correspond to the south portion of the test basin. (see Fig. 3.6).

3.5.1 Bending Moments

Figure 10 compares the experimental and numerical bending moments for the (a) unlined pipeline, (b) lined pipe centered and (c) lined joint centered tests at a fault displacement just before failure, which is listed in each figure. The joint centered case results in the maximum measured bending moments and is representative of how the experimental and numerical bending moment distributions compare at all levels of fault movement. The locations of the joints are marked with dashed lines. The experimental bending strains were calculated as one half the difference in measured axial strains across the pipe springlines, and were converted in bending moment, M, through the expression:

$$M = \frac{EI\varepsilon_b}{D/2} \tag{3.7}$$

where E is the DI Young's modulus, I is the pipe moment of inertia, ε_b is the bending strain, and D is the pipe outer diameter.

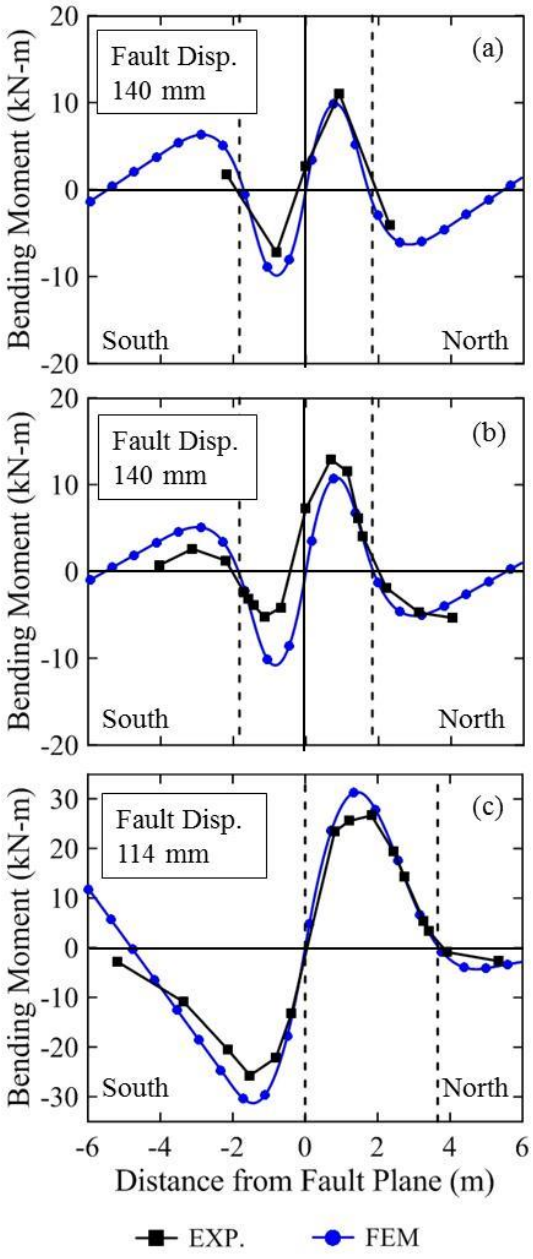

Figure 3.10. Bending Moment Distribution Along the Pipeline for (a) Unlined Pipeline, (b) CIPL-reinforced Pipeline at Pipe Centered Configuration and (c) CIPL-reinforced Pipeline at Joint Centered Configuration.

The maximum numerical and experimental moments compare very favorably with respect to magnitude and location for all three cases. This favorable comparison arises because the lateral force vs. displacement relationships for soil reactions used in the modeling are well known from previous investigations (Jung et al. 2016), which shows that the CIPL does not provide significant resistance against rotation of the joints. If the CIPL joints are modeled as pins, the numerical bending moments are virtually unchanged for both lined pipelines. The numerical and experimental moment distributions are in good agreement for the unlined pipeline and lined joint centered test.

The experimental and numerical bending moments for the lined pipe centered test compare favorably north of the fault rupture, but the experimental measurements are as much as 50% lower than the numerical results south of the fault rupture. The differences on the north and south sides can be explained with reference to Fig. 3.11, which shows a schematic of the pipeline crossing the fault. The shear forces carried by the joints are in opposite directions. Because the spigot will not be centered perfectly in the bell, the shear force on one of joints can be resisted by metal to metal contact at the same time the shear force on the opposing joint is carried by the CIPL. Although the lining shear stiffness is increased by internal pressure, it nonetheless is substantially smaller than the stiffness resulting from metal to metal contact. As a consequence, the shear force on one side of the fault can exceed that on the opposite side, resulting in an asymmetric distribution of moments with lower moments on the side of the fault where the joint shear stiffness is lowest. An asymmetric pattern of moments is not observed in the unlined pipeline because there is no pressurized CIPL

to resist shear, and the spigot shifts inside the bell to make metal to metal contact in the joints on both sides of the fault. For the lined joint centered test, there is an inflection point at the fault crossing, which results in similar but opposite moment distributions either side of the fault.

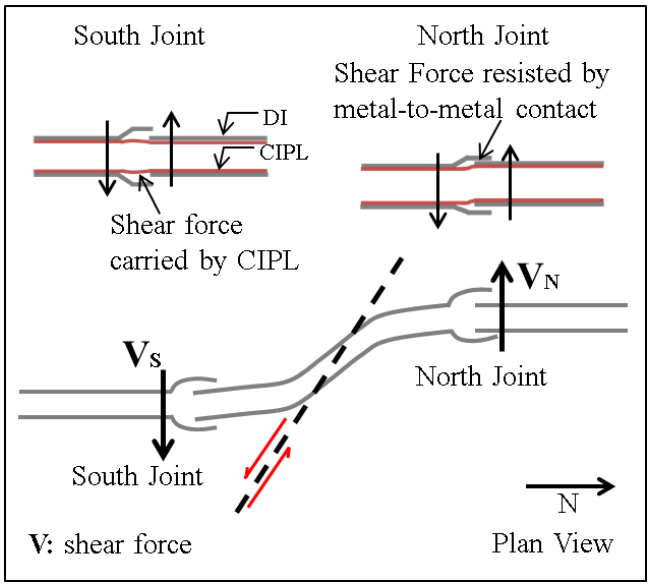

Figure 3.11. Schematic of Pipe Centered Fault Rupture Test on Jointed CIPL-reinforced Pipeline with Different Shear Force Transfer Mechanisms at the Joints.

3.5.2 Axial Forces

Figure 3.12 compares the experimental and numerical axial forces for the (a) unlined pipeline, (b) lined pipe centered and (c) lined joint centered tests at a fault displacement just before failure, which is listed in each figure. The pipe centered case results in the maximum measured axial forces in the pipe and is representative of how the experimental and numerical axial force distributions compare at lower levels of fault movement. The locations of the joints are marked with dashed lines. The experimental axial strains were calculated at each strain gage station as the average of the strain gage measurements and were then converted into axial forces through the expression:

$$N = EA\varepsilon_{\alpha} \tag{3.8}$$

where E is the DI Young's modulus, A is the pipe cross-sectional area, and ε_{α} is the average strain.

Two different conditions were simulated for the maximum longitudinal frictional force along the pipeline: (a) K_o conditions, following Eqn. 3.3, which apply for zero or very little induced lateral movement and (b) frictional force coupled to normal force, following Eqn. 3.4. The frictional forces based on Eqn. 3.4, which involve substantially greater lateral movements, are significantly higher than those calculated by Eqn. 3.3.

Figure 3.12a shows that the experimental axial forces for the unlined pipeline plot approximately midway between the numerical results for K_o and coupled friction/normal force conditions. Because of the low pullout resistance of the push-on joints, the measured axial forces are very low and only slightly higher than the repeatability of the gages.

Figure 3.12b shows good agreement in the lined pipe centered test between the experimental and numerical results for coupled friction/normal force conditions. There is very close agreement (less than 15% difference) between the maximum axial force at the fault rupture measured during the experiment and given by the numerical simulation for coupled friction/normal force conditions. In contrast, the measured maximum axial force is markedly higher (approximately 30%) than that predicted for K_o. The shaded areas around the joints mark the total CIPL de-bonding lengths that were 360 mm and 300 mm from the de-bonding simulation for the South and North joint, respectively. The model predicts de-bonding that advances uniformly around the

pipe circumference. The numerical results compare favorably with the experimental total de-bonded lengths, determined by strain gage measurements, of 380 and 280 mm, for the South and North joints, respectively.

Figure 3.12c shows that the experimental axial forces plot midway between the numerical results for K_o and coupled friction/normal force conditions north of the fault. South of the fault, the pipeline length in soil was designed to be relatively short to reduce the volume of soil needed for testing and still replicate pipeline performance unaffected by the boundaries of the test basin. There was a loss of longitudinal friction along the pipeline south of the fault. Such reductions have been observed in short lengths of pipeline that are pulled through unsaturated soil (Wham et al., 2017). When short lengths of pipe (less than 2.5 m) are inclined slightly in the longitudinal direction, they can create a small void above the pipe as they are pulled forward, which remains open due to suction in the partially saturated sand. To simulate this loss of contact south of the fault, longitudinal friction was reduced from a value consistent with coupled friction/normal forces conditions to one consistent with K_o conditions. The shaded areas around the joints mark the CIPL de-bonded lengths of 340 mm and 165 mm for the South and North joints, respectively, as predicted by the numerical simulations. Due to irregular propagation of the de-bonding, the experimental de-bonded lengths were hard to identify. In this test the strain gage measurements indicated that de-bonding advanced approximately 380 mm further at some locations around the pipe circumference than others. The maximum total de-bonding length is estimated from the gages as 700 mm and 254 mm for the South and North joint, respectively. Both experimental estimates are for maximum de-bonding distances

along an irregularly advancing front, whereas the numerical results are for a uniform de-bonding around the pipe circumference.

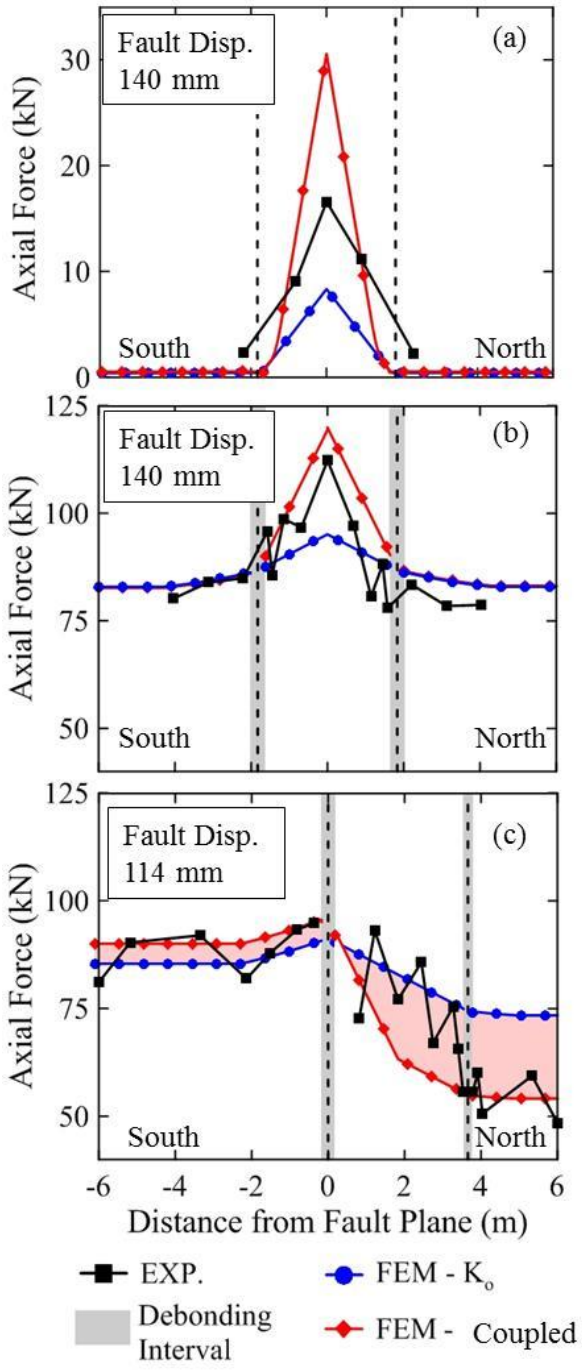

Figure 3.12. Axial Force Distribution Along the Pipeline for (a) Unlined Pipeline, (b) CIPL-reinforced Pipeline at Pipe Centered Configuration and (c) CIPL-reinforced Pipeline at Joint Centered Configuration.

3.5.3 Axial Joint Movement

Figure 3.13 shows the joint openings relative to the imposed fault displacement along the pipeline for the (a) unlined pipeline, (b) lined pipe centered, and (c) lined joint centered tests. The joint pullouts were calculated by averaging the three LVDT measurements installed at each joint. The fault displacement at failure is identified for each plot, defined as either joint pullout for the unlined pipeline test or lining rupture for lined pipeline tests.

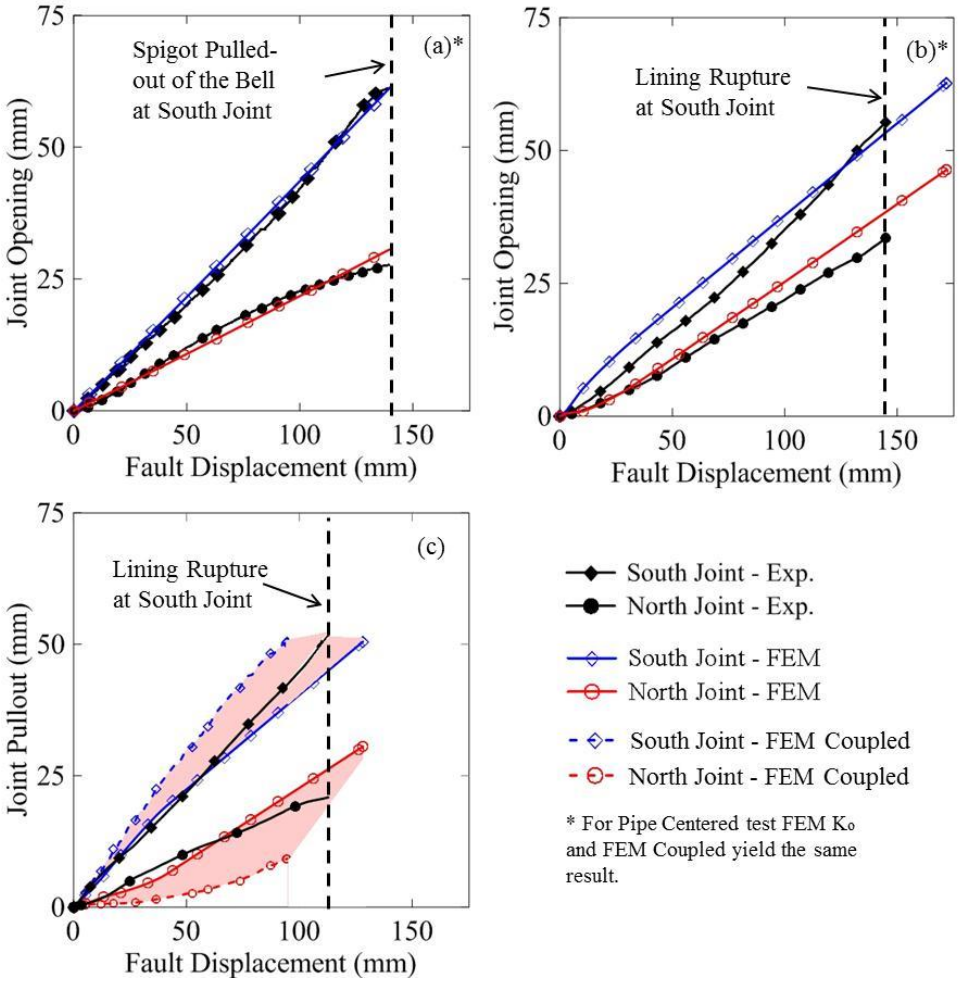

Figure 3.13. Joint Openings vs. Fault Displacement for (a) Unlined Pipeline, (b) CIPL-reinforced Pipeline at Pipe Centered Configuration and (c) CIPL-reinforced Pipeline at Joint Centered Configuration.

Wham et al. (2017) report on pullout tests of jointed pipelines in the same soil and burial conditions as associated with the fault rupture tests reported in this work. Their experimental results show a higher resistance to pullout when the flat end rather than the curved end of the bell is pulled in the direction of axial pipe movement. In all the fault rupture tests, therefore, there was a bias for additional axial pullout at the South joint because the flat end of the bell was facing the direction of axial movement toward the fault rupture and was resisting movement while the spigot pulled from the bell. Appendix B provides an explanation for the uneven distribution of joint pullouts in the pipe centered condition. To replicate the experimental results, lower axial pullout capacity assigned to the South joint in the numerical models for the unlined and lined pipe centered tests.

Figures 3.13a and 3.13b show the simulated joint openings for coupled friction/normal force conditions and the experimental measurements. For the unlined test, the stiffness of the axial joint spring (see Fig. 3.7b) of the south joint was set half of that of the north joint. For the pipe centered test, the pipe/lining interface springs (see Fig. 3.8) were assumed to have virtually zero capacity within 40 mm at each side of the South joint. Fig. 3.13c shows that the experimental results are between the numerical simulations for K_o and coupled friction/normal force conditions. As discussed in the previous subsection, for the case of coupled frictional/normal forces, higher maximum frictional forces were assigned to the center pipe for both pipe and joint centered configurations. Due to the symmetry of the pipe centered configuration, the numerical joint openings are identical for both approaches (K_o conditions and coupled normal/frictional forces). For the joint centered test, the lower frictional forces

south of the South joint in combination with the non-symmetrical configuration of the test resulted in differences in the numerical joint openings.

Figure 3.13 indicates that the South joint opening is larger than the North joint opening for all three tests. For the lined joint centered test, the South joint is located at the fault and is expected to pull out more than the North joint, which is further away. That ratio of joint pullouts is approximately constant and equal to 2 and 1.6 at all levels of fault displacement for the unlined pipeline and lined pipe centered tests, respectively. An apparently small bias, such as the orientation of the bells, affects the results so that there is considerably more movement at one joint relative to the other. Equal joint movement, therefore, is an unconservative assumption for design even though the joints are equidistant from the fault in similar soil conditions.

3.5.4 Joint Rotations and Moments

Figure 3.14a compares the measured and simulated joint rotation relative to the fault displacement for the South joint of the lined pipe centered test. The measurement is in excellent agreement with the numerical results to 120 mm of fault displacement, with maximum values of 1.8^o and 2.2^o for the test and numerical simulation, respectively.

Assuming that the CIPL-reinforced joints behave as hinges, a simplified estimate of joint rotation, α_S, can be made as follows:

$$\alpha_S = \sin^{-1}\left(\frac{d \sin \beta}{L_{pipe}}\right) \tag{3.9}$$

where d is the fault displacement, β is the angle of fault intersection with the pipeline, equal to 50^o, and L_{pipe} is the length of the center pipe segment equal to 3.7 m. This

simplified estimate for the joint rotation, α_S, is also plotted on Fig. 3.14a and predicts smaller rotations that are approximately 90% of the numerical model rotations.

Figure 3.14b compares the joint moment vs. rotation relationship for the South joint of the lined pipe centered test with the results of a four-point bending test conducted on a lined bell-and-spigot joint. The joint moment for the fault rupture test was calculated by interpolating the moments at strain gage planes located at both sides of the joint, as illustrated in the insert diagram of Fig. 3.14b. The moment vs. rotation relationships are in reasonably good agreement, and both confirm the low resistance to moment provided by the lined joints. Fig. 3.14b also presents the simplified bilinear moment vs. rotation relationship used in the FE simulations, as described previously under Joint Modeling section.

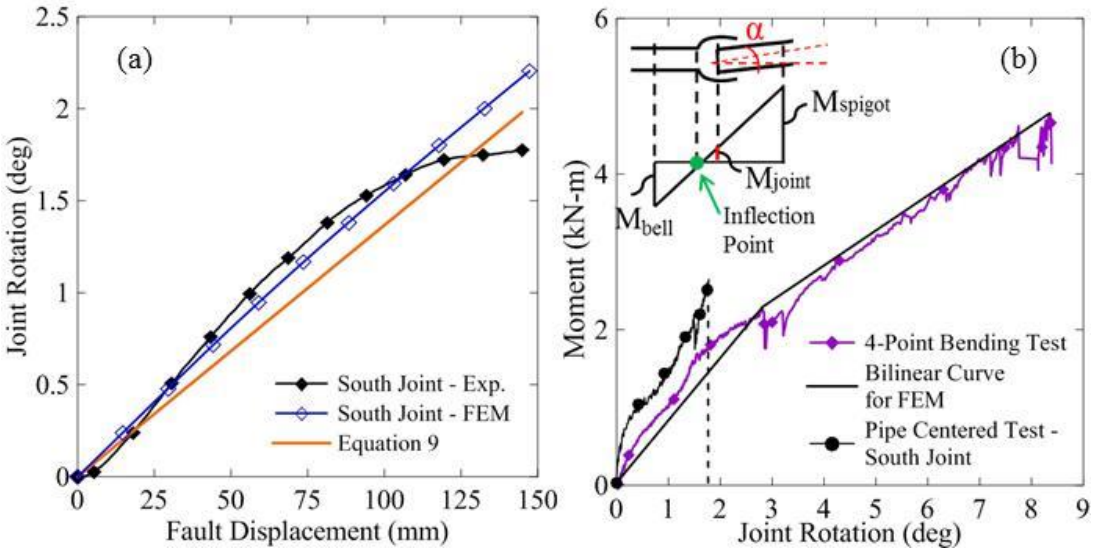

Figure 3.14. CIPL-reinforced Pipeline at Pipe Centered Configuration (a) South Joint Rotation vs. Fault Displacement and (b) South Joint Moment vs. Rotation.

Direct tension test results to characterize the axial force vs. joint opening relationship for lined joints are presented by Argyrou et al. (2017). Although space

limitations do not allow for comparison of the axial force vs. joint opening measurements from the fault rupture tests vs. those reported by Argyrou et al. (2017), conclusions similar to those for the moment vs. rotation relationships can be drawn. There is good agreement between the axial force vs. joint opening relationships from direct tension tests performed outside the experimental basin with those derived from measurements during the fault rupture tests.

3.6 Concluding Remarks

This paper summarizes the experimental results of full-scale fault rupture tests on an unlined pipeline and two pipelines reinforced with CIPLs. The 150-mm-diameter DI pipelines were buried in dense, unsaturated sand with $\phi' = 42°$ as determined by direct shear tests. The DI pipelines were used as proxies for CI pipelines with round cracks and weak joints, representative of aging pipelines. Full-scale test and numerical simulation results lead to several observations and conclusions:

- There is close agreement between the experimentally measured and numerically simulated moments at virtually all locations along the pipelines in all tests. The close agreement reflects the quality of the modeling procedures and force vs. displacement relationships that are well established from previous investigations (Jung et al., 2016). There may be variable shear stiffness in lined joints, depending on whether metal to metal or metal to lining contact occurs in response to shear forces generated by soil-structure interaction. Modeling the joints for high shear stiffness, representative of metal to metal contact,

results in moments that match the highest measured moments and provides a conservative assessment for all cases.

- The experimental axial forces compare favorably with numerically simulated forces for coupled friction/normal force conditions in all tests. This result corroborates the findings of O'Rourke et al. (2016) that coupling normal and frictional forces in the numerical modeling is necessary for assessing the maximum axial pipe forces, and therefore strongly recommended.

- Test results show unequal movement of joints that are equidistant from the fault. The ratio of joint pullouts is approximately constant and equal to 2 and 1.6 at all experimental fault displacements for the unlined pipeline and lined pipe centered tests, respectively. An apparently small bias, such as the orientation of the bells, affects the results, resulting in considerably more movement in one joint relative to the other. Equal joint movement is therefore an unconservative design assumption even for joints equidistant from the fault in similar soil conditions.

- There is good agreement between the axial force vs. joint opening and moment vs. rotation relationships from direct tension and four-point bending tests, respectively, with those derived from measurements during the fault rupture tests. Direct tension and four-point bending tests therefore provide a sound basis for the numerical modeling of joint response for pipelines reinforced with CIPLs subject to fault rupture movements similar to those generated in the full-scale tests.

- There is very good agreement between the numerical results of the model, which was developed in this work to account for de-bonding between the lining and pipe as the propagation of a Mode II fracture, and large-scale test results both with respect to axial forces and joint pullouts. The model therefore can be used to simulate the performance of CIPL-reinforced pipelines under earthquake-induced fault rupture as well as other sources of permanent ground deformation.

Of key importance is the de-bonding of the lining under axial extension of the pipeline. The de-bonding allows the lining to increase in length, thereby accommodating tensile ground movements. The de-bonding also allows the linings to accommodate bending and rotation at the locations of defects, such as weak joints and round cracks in brittle pipelines and conduits. Successful design and product development for seismic retrofitting requires an axial lining strength that exceeds the fracture propagation forces and a modulus that allows the lining to elongate sufficiently to accommodate the axial components of externally imposed ground deformation.

The findings of this work are relevant for distribution pipelines with diameters ranging from 100 mm to as large as 600 mm in which the linings are installed by an inversion or direct insertion process. Additional experimental and numerical work is necessary to evaluate the performance of larger diameter pipelines with hand-placed lining systems.

REFERENCES

ABAQUS. (2014). [computer software]. Dassault Systèmes Version 6.13, Dassault Systèmes, Providence, RI.

Ampiah, N., Fam, A. and Moore, I.D. (2010). "Effect of Wrinkles on the Circumferential Strength of a Cast-in-Place Composite Polymer Liner Used in Retrofitting Pressure Pipes." *Journal of Materials in Civil Engineering*, 10.1061/(ASCE)MT.1943-5533.0000160.

Argyrou, C., Bouziou, D., O'Rourke, T.D. and Stewart, H.E. (2017). "Retrofitting Utilities for Earthquake-Induced Ground Deformations." *3rd International Conference on Performance-based Design in Earthquake Geotechnical Engineering (PBD-III)*, July 16-19, Vancouver, Canada.

ASCE. (1984). "Guidelines for the Seismic Design of Oil and Gas Pipeline Systems." *Committee on Gas and Liquid Fuel Lifelines*, American Society of Civil Engineers, New York, NY.

ASTM. (2014). "Standard Test Method for Tensile Properties of Polymer Matrix Composite Materials." *Standard No. ASTM D3039/D3039M-14*, American Society for Testing and Materials International, West Conshohocken, PA.

ASTM. (2013). "Standard Test Methods for Tension Testing of Metallic Materials." *Standard No. ASTM E8/E8M-13a*, American Society for Testing and Material International, West Conshohocken, PA.

ASTM. (2010a). "Standard Test Method for In-Place Density and Water Content of Soil and Soil-Aggregate by Nuclear Methods (Shallow Depth)." *Standard No. ASTM D6938-10*, American Society for Testing and Materials International, West Conshohocken, PA.

ASTM. (2010b). "Standard Test Methods for Laboratory Determination of Water (Moisture) Content of Soil and Rock Mass." *Standard No. ASTM D2216-10*, American Society for Testing and Materials International, West Conshohocken, PA.

ASTM. (2002). "Standard Specification for Cured-in-Place Pipe Lining System for Rehabilitation of Metallic Gas Pipe." *Standard No. ASTM F2207-02*, American Society for Testing and Materials International, West Conshohocken, PA.

AWWA. (2011). "Cement-Mortar Lining of Water Pipelines in Place-4 in. (100 mm) and Larger." *Standard No. C602-11*, American Water Works Association, Denver, CO.

AWWA. (2001). "Rehabilitation of Water Mains." *Manual of Water Supply Practices M28, 2nd Ed.*, American Water Works Association, Denver, CO.

Bouziou, D. (2015). “Earthquake-Induced Ground Deformation Effects on Buried Pipelines.” PhD Dissertation: Cornell University, Ithaca, NY.

Bouziou, D., Wham, B.P., O’Rourke, T.D., Stewart, H.E. and Palmer, M.C. (2012). “Earthquake Response and Rehabilitation of Critical Lifelines.” *15th World Conference on Earthquake Engineering*, Sept. 24-28, Lisbon, Portugal.

Brown M.J.P., Moore I.D. and Fam, A. (2014). “Performance of a Cured-in-Place Pressure Pipe Liner Passing through a Pipe Section Without Structural Integrity.” *Tunneling and Underground Space Technology*, 42, 87-95.

Caggiano, A., Martinelli, E. and Faella, C. (2012). “A Fully-Analytical Approach for Modeling the Response of FRP Plates Bonded to a Brittle Substrate.” *International Journal of Solids and Structures*, 49(17), 2291-2300.

Cornell Lifelines Group. (2017). “Large-Scale Split-Box Test Basin at Cornell University.” <https://lifelines.cee.cornell.edu/> (Aug. 11, 2017).

Faella, C., Martinelli, E. and Nigro, E. (2009). “Direct vs. Indirect Method for Identifying FRP-to-Concrete Interface Relationships.” *Journal of Composites for Construction*, 10.1061/(ASCE) 1090-0268(2009) 13:3 (226).

Jeon, S-S., O’Rourke, T.D. and Netrevali, A.N. (2004). “Repetitive Loading Effects on Cast Iron Pipelines with Cast-in-Place Lining Systems.” *Journal of Transportation Engineering*, 10.1061/(ASCE)0733-947X(2004)130:6(692).

Jung, J.K., O’Rourke, T.D. and Argyrou, C. (2016). “Multi-Directional Force-Displacement Response of Underground Pipe in Sand.” *Canadian Geotechnical Journal*, 53, 1763-1781.

Kramer, S. R., McDonald, W.J. and Thomson, J.C. (1992). “An Introduction to Trenchless Technology.” Van Nostrand Reinhold, New York.

Netravali, A.N., O’Rourke, T.D., Shaw, S.K. and Bond, T. (2003). “Evaluation of Starline 2000-PSE Cured-In-Place Lining System for Cast Iron Gas Distribution Pipelines.” *Final Report Contract No. 39802*, Prepared for New York Gas Group, Apr., Cornell University, Ithaca, NY.

Netravali, A.N., O’Rourke, T.D., Gerritsen, K.I., Singh, Y.P., Jeon, S.-S. and Zhao D. (2000). “Advanced Pipeline Support and Stabilzed Backfill for Gas mains Affected by Excavations - Part 2: Cast-in-Place Pipe Linking Systems for Cast Iron and Steel Mains.” *Report prepared for NYGAS, Contract No. 31120*, Cornell University, Ithaca, NY.

O'Rourke, T.D., Jung, J.K., Argyrou, C. (2016). "Underground Pipeline Response to Earthquake-Induced Ground Deformation." *Soil Dynamics and Earthquake Engineering*, 91, 272-283.

O'Rourke, T.D. (2010). "Geohazards and Large, Geographically Distributed Systems." *Geotechnique*, 60(7), 505-543

O'Rourke, T.D., Jezerski, N.A. Olson, T., Bonneau, A.L., Palmer, M.C., Stewart, H.E., O'Rourke, M. J. and Abdoun, T. (2008). "Geotechnics of Pipeline System Response to Earthquakes." Keynote Paper, *Geotechnical Earthquake Engineering and Soil Dynamics IV (GEESD)* Sacramento, CA, May.

O'Rourke, T.D., Netravali, A.N., Pendharkar, S.M., Tonkinson, A., Chaudhuri, D. and Toparak, S. (1996). "Evaluating Service Life of Anaerobic Joint Sealing Products and Techniques." *Final Report, Report No. GRI-96/0318,* Prepared for Gas Research Institute, Contract No. 5093-207-2798, Cornell University, Ithaca, NY.

O'Rourke, T.D. and Druschel, S.J. (1989). "Improved Anchoring Practices for Plastic Gas Distribution Pipelines." *Final Report prepared for New York Gas Group*, Cornell University, Ithaca, NY.

Patton, F.D. (1966). "Multiple Modes of Shear Failure in Rock." *1st Congress in Rock Mechanics*, Lisbon, 1, 509-513.

Progressive Pipeline Management. (2011). "3D view of Starline2000®." <http://progressivepipe.com/>. (Sept. 10, 2013).

Stewart, H.E., O'Rourke, T.D., Wham, B.P., Netravali, An., Argyrou, C., Zeng, X. and Bond, T.K. (2015). "Performance Testing of Field-Aged Cured-in-Place Liners (CIPL) for Cast Iron Piping." *Final Report prepared for NYSEARCH/Northeast Gas Association*, December, Cornell University, Ithaca, NY.

Taljsten, B. (1996). "Strengthening of Concrete Prisms Using the Plate-Bonding Technique." *International Journal of Fracture*, 82(3), 253-266.

Wham, B.P., Pariya-Ekkasut, C., Argyrou, C., Lederman, A., O'Rourke, T.D. and Stewart, H.E. (2017). "Experimental Characterization of Hazard-Resilient Ductile Iron Pipe Soil/Structure Interaction under Axial Displacement." *Congress on Technical Advancement*, Sept. 10-13, Duluth, MN, available at: https://ascelibrary.org/doi/pdf/10.1061/9780784481028.013.

Wham, B.P. and O'Rourke, T.D. (2015). "Jointed Pipeline Response to Large Ground Deformation." *Journal of Pipeline Systems Engineering and Practice*, 10.1061/(ASCE)PS.1949-1204.0000207.

Zhong, Z., Filiatraut, A. and Aref A. (2017a). “Numerical Simulation and Seismic Performance Evaluation of Buried Pipelines Rehabilitated with Cured-in-place Pipe Liner under Seismic Wave Propagation.” *Earthquake Engineering and Structural Dynamics*, International Association for Earthquake Engineering, 46(5), 811-829.

Zhong, Z., Filiatraut, A. and Aref A. (2017b). “Experimental Performance Evaluation of Pipelines Rehabilitated with Cured-in-place Pipe Liner under Earthquake Transient Ground Deformations.” *Journal of Infrastructure Systems*, 10.1061/(ASCE)IS.1943-555X.0000326.

Zhong, Z., Bouziou D., Wham B., Filiatraut, A., Aref A., O’Rourke, T.D. and Stewart, H.E. (2014). “Seismic Testing of Critical Lifelines Rehabilitated with Cured-in-Place Pipeline Lining Technology.” *Journal of Earthquake Engineering*, 18(6), 964-985.

Zhong, Z. (2014). “Earthquake Response and Rehabilitation of Critical Underground Lifelines Reinforced with Cured-in-Place Pipe Liner Technologies under Transient Ground Deformations.” PhD Dissertation: University at Buffalo, Buffalo, NY.

CHAPTER 4

DUCTILE IRON PIPELINE RESPONSE TO EARTHQUAKE-INDUCED GROUND RUPTURE

Abstract

This paper provides a comprehensive evaluation of ductile iron (DI) pipeline response to earthquake-induced ground deformation through the results of a large-scale testing program and a fault rupture test on a 150-mm DI pipeline with restrained axial slip joints. The test is used to validate a two dimensional finite element (FE) model that accounts for soil-pipeline interaction with axial slip, pullout resistance, and rotation of pipe joints. The maximum strike-slip fault offset sustained by push-on, restrained, and restrained axial slip joints is presented as a function of the pipeline/fault crossing angle. A systematic FE assessment shows that pipelines with restrained axial slip joints accommodate 2 to 9 and 2 to 10 times as much fault offset as pipelines with push-on and restrained joints, respectively, for most intersection angles. The results of this work can be used for simplified design and to quantify the relative earthquake performance of different DI pipelines.

4.1 Introduction

Underground pipelines in seismically active areas are often affected by earthquake-induced ground deformation from surface faulting, landslides, and liquefaction-induced lateral spreading and subsidence (O'Rourke et al., 2008). Examples of abrupt ground rupture are illustrated in Fig. 4.1. Oblique slip affecting pipelines crossing a fault plane is shown in Fig. 4.1a. Strike slip across the fault plane may be accompanied by

compression or tension, depending on the angle of intersection between the pipeline and fault. As illustrated in Fig. 4.1b, a pipeline crossing a lateral spread or landslide perpendicular to the general direction of soil movement is subject mainly to bending strains and extension. As shown in Fig. 4.1c, a pipeline will undergo deformation at the margins of a lateral spread or landslide in a manner similar to a fault crossing, with bending and either tension or compression where the crossing is at an oblique angle. Fig. 4.1d shows a pipeline oriented parallel to the general direction of soil displacement. At the head and base of the soil movement zone, displacements resemble normal and reverse faulting, respectively, with tension and bending at the head and compression and bending at the base.

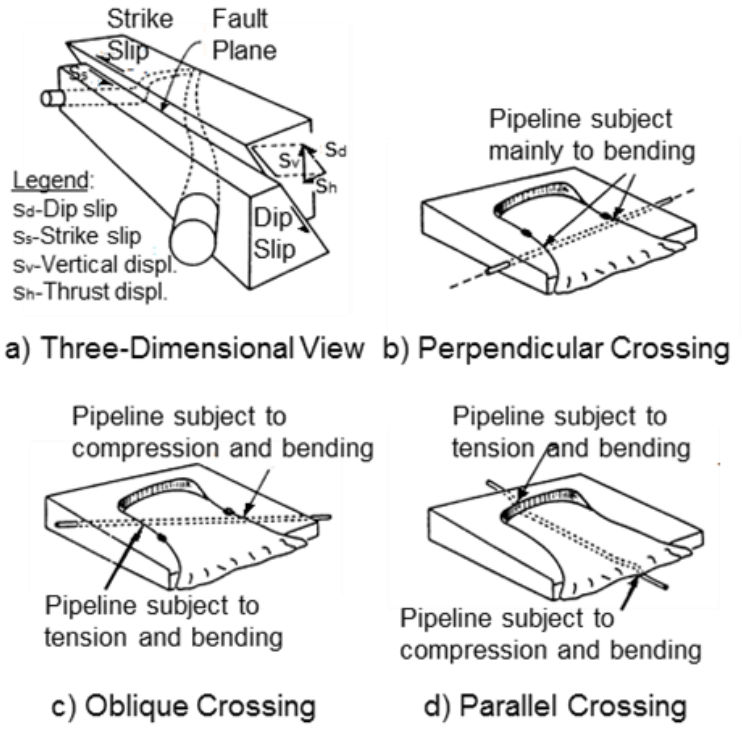

Figure 4.1. Principal Modes of Soil-Pipeline Interaction Caused by Earthquake-Induced Permanent Ground Deformation (O'Rourke et al., 2008).

This paper provides an evaluation of ductile iron (DI) pipeline response to strike-slip fault movement, which is also representative of ground deformation along the margins of liquefaction-induced lateral spreads and landslides. Due to the combination of large lateral soil pressure and elevated levels of axial pipe response, strike-slip fault movement causes some of the most severe pipeline deformation associated with externally imposed differential soil displacement. Three different DI joints are investigated, including push-on, restrained, and restrained axial slip joints. The latter type of joint resists pullout and allows for axial slip to absorb extension and compression. It is frequently referred to as an earthquake-resistant or hazard resilient joint (Stewart et al., 2015). DI pipelines with restrained axial slip joints can be used to accommodate large ground movements caused by earthquakes, flooding, subsidence related to mining and groundwater withdrawal, expansive soils, frost heave, adjacent excavations, and tunneling.

The paper begins with a description of the three types of DI pipeline joints, followed by discussion and characterization of the limit states controlling performance. A description is given for the two-dimensional (2D) finite element (FE) model that was developed in this work to simulate pipeline response to large ground deformation. The results of a large-scale fault rupture test on a nominal 150-mm DI pipeline with restrained axial joints is used to validate a 2D FE model that accounts for axial slip, pullout resistance, and rotation of the joints under conditions of extreme soil-pipeline interaction. The results of systematic and detailed FE simulations are presented for the response in granular soil of DI pipelines with three different types of joints to strike-slip fault displacement. The response for each DI jointed pipeline type is presented in terms

of ground movement that can be sustained as a function of the pipeline/fault crossing angle. A comparative assessment of the different joints types is made with recommendations for design and future research.

4.2 Joint Description

Figure 4.2 shows cross-sections of the three types of DI joints. Nominal 150-mm diameter DI push-on, restrained, and restrained axial slip joints, manufactured by U.S. Pipe under the commercial name TYTON®, TR Flex®, and TR-XTREME™, respectively, were used in this investigation. Each DI pipe joint is equipped with a rubber gasket to prevent leakage. A restrained joint has a weld bead on the spigot end and employs two restraining clips as a locking mechanism to resist pullout under tension. The restrained axial slip joint likewise employs two restraining clips to resist pullout, but possesses an elongated bell to allow for axial slip of the spigot. As shown in Fig. 4.2c, there is a 72-mm separation between the gasket haunch and locking segment. If the restrained axial slip joint is set at a position midway between them, the joint can accommodate 36 mm of axial displacement for both tension and compression before the weld bead contact with the gasket haunch or locking segment.

As illustrated in Fig. 4.3, two locking segments are used for nominal 100-mm to 200-mm joints. The three-dimensional (3D) view in Fig. 4.3a shows that locking segments are inserted typically into slots in the bell and rotated into the 9 and 3 o'clock positions around the pipe circumference. Under maximum joint extension the weld bead on the spigot makes contact with the two clips, which provide resistance to further axial slip. Fig. 4.3b is a photo, looking down, of the locking segments in contact with the

weld bead at their approximate circumferential positions in a typical field installation. Locking clips are used with some, but not all, DI joints. Full circumferential locking rings provide the restraining mechanism used in other commercially available DI joints.

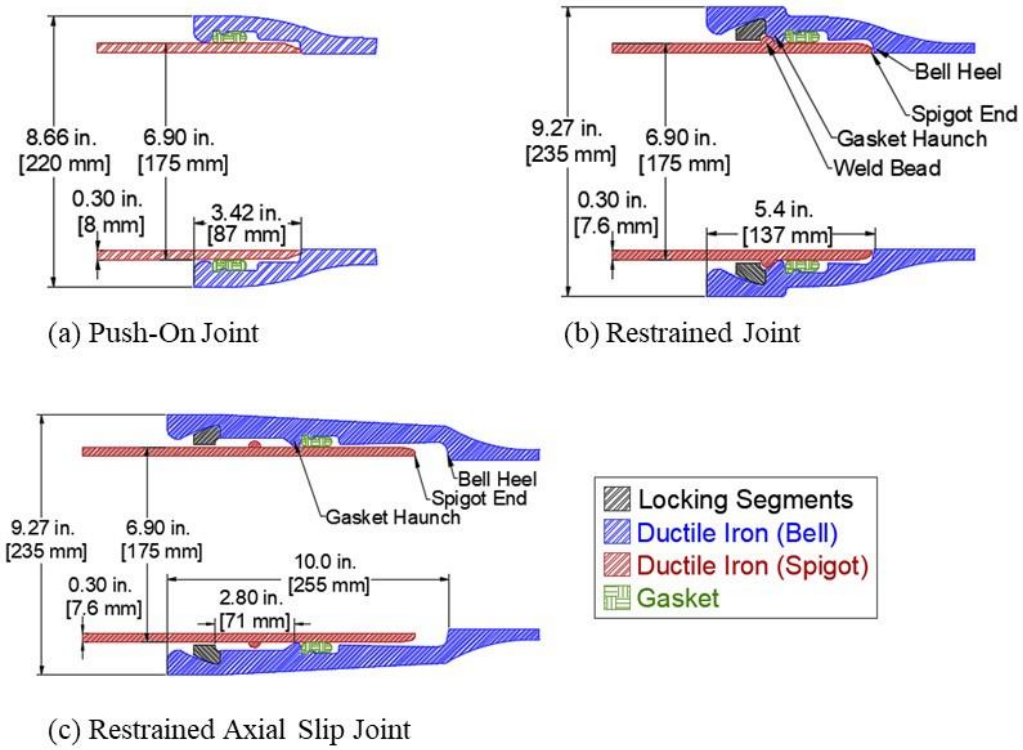

Figure 4.2. Cross-Sectional Views of DI Pipe Joints Including a) Push-On, b) Restrained, and c) Restrained Axial Slip Joint.

Figure 4.4 is a photo of two restrained axial slip joints compared with a typical push-on joint. The bell is considerably larger in diameter and length than the push-on joint. Figure 4.2 shows that the restrained joint bell has the same external diameter as that of the restrained axial slip joint, but is similar in length to that of the push-on joint. The bell diameters of all DI joints are larger than the pipe barrel diameter, and this applies in particular to the bells of both restrained and restrained axial slip joints. After pipe burial, the bells are anchored into the adjacent soil so that localized axial resistance at the bells is mobilized as the pipe moves relative to the ground.

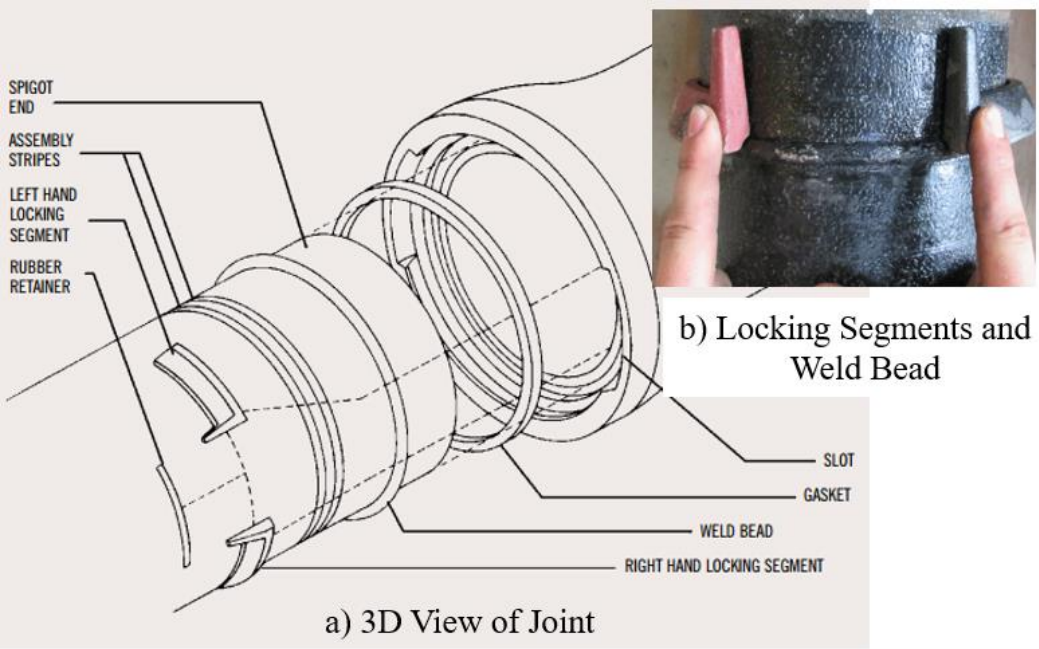

Figure 4.3. (a) 3D View of Restrained Axial Slip Joint with Locking Segments, Slots, Weld Bead, and Gasket (U.S. Pipe, 2017) and (b) Detail of Locking Segments and Weld Bead.

Figure 4.4. Photo of Enlarged Bells Used in Restrained and Restrained Axial Slip DI Joints.

4.3 Numerical Modeling

4.3.1 Two-Dimensional Finite Element (2D FE) Model for Soil/Jointed Pipeline Interaction

Fig. 4.5 shows a schematic of the 2D FE model, developed in this work using Abaqus (v6.13-2). The basic aspects of the numerical model follow those provided in the ASCE Guidelines (1984) and Honegger et al. (2004), whereby the pipeline is simulated by geometrically nonlinear beam elements and the soil reaction to relative soil/pipe movement by springs following nonlinear force vs. displacement relationships. The soil reaction is modeled using independent springs in the pipeline longitudinal and transverse directions. In the case of strike-slip faulting, only the longitudinal and transverse horizontal soil reaction components are modeled. The FE model in this work involves significant modifications of the base model in the ASCE guidelines (1984) that account for (i) coupling of shear force at the soil/pipe interface with forces normal to the longitudinal axis of the pipeline, (ii) combined axial slip, pullout resistance, and rotation of the joints, and (iii) axial resistance of the joints to relative pipe/soil movement.

4.3.2 Soil Reaction Springs in the Transverse Horizontal Direction

Jung et al. (2016) provide the dimensionless lateral force per unit length, N_{qH}, for dry and partially saturated sands of different unit weights, depths of burial, and directions of transverse pipe movement relative to the soil. The maximum lateral force per unit pipe length, f_{ym}, is calculated by the following expression:

$$f_{ym} = N_{qH}\,\bar{\gamma}\,H_c D \tag{4.1}$$

where $\overline{\gamma}$ is the soil effective unit weight, D is the pipe outer diameter and H_c is the burial depth from the ground surface to pipe centerline. The N_{qH} vs. H_c/D relationship for partially saturated sand provided by Jung et al. (2016) was used in this work.

According to Jung et al. (2016) the bilinear representation of the lateral soil reaction, f_y, vs. relative soil/pipe displacement, δ_y, is defined by a linear relationship to the maximum lateral force, f_{ym}, at a relative soil/pipe displacement, δ_{ym}, given by the following expression:

$$\delta_{ym} = 0.014 H_c \tag{4.2}$$

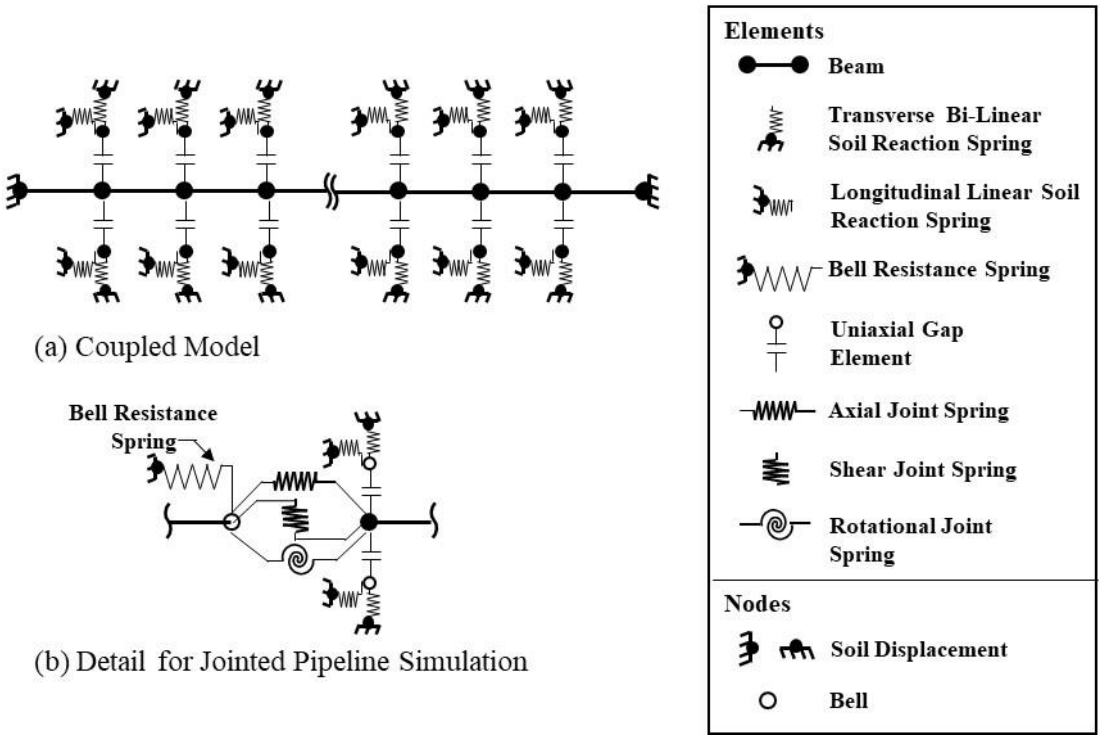

Figure 4.5. 2D FE Model for Soil-Pipeline Interaction Accounting for Coupled Normal/Shear Forces to the Pipeline and Bell Resistance.

4.3.3 Coupling of Normal and Frictional Forces

When a buried pipeline is subjected to ground displacement parallel to its longitudinal axis, the frictional force per unit length generated by relative soil/pipe axial movement is given in the ASCE Guidelines (1984) and Honegger et al. (2004) as:

$$f_{xo} = \frac{\pi D}{2}(1 + K_o)\,\bar{\gamma}\,H_c \tan\delta_s \tag{4.3}$$

where K_o is the at-rest earth pressure coefficient, and δ_s is the soil/pipeline interface friction angle. A value of 0.45 was used for K_o in accordance with soil stress measurements reported by O'Rourke and Druschel (1989) from full-scale axial pipe pullout tests.

When a buried pipeline is subjected to lateral as well as axial displacement, the at-rest conditions are disturbed and the frictional forces no longer can be determined by Eqn. (4.3). O'Rourke et al. (2016) present a modified 2D FE model that accounts for coupled normal and frictional forces on the pipeline through a Coulomb frictional law. To achieve this coupling, the transverse springs are connected to the pipeline with uniaxial gap elements that allow for the transfer of forces normal and parallel to the longitudinal axis of the pipe. The lateral soil forces are transferred unaltered to the pipeline through the gap elements, while the forces parallel to the pipeline axis are controlled by the Coulomb friction law, so they are proportional to the lateral force acting on the pipeline at each level of deformation, such that:

$$f_x = f_y \tan\delta_s \tag{4.4}$$

where f_y is the lateral force per pipeline unit length with maximum f_{ym} given by Eqn. (4.1). Direct axial pull tests on 150-mm DI pipe specimens reported by Wham et al.

(2017) showed that δ_s ranges from 0.8 ϕ' to 1.0 $\phi'$for a sand/DI interface, where ϕ' is the effective stress soil friction angle. In this study, a value of 0.9φ′ was selected for the numerical simulations.

The longitudinal linear soil reaction springs in Fig. 4.5 are needed to induce movement to activate the forces normal to the gap element axis. Shear transfer, in essence, follows a rigid plastic response. Direct shear tests for dense sand on cast iron (CI) surfaces (O'Rourke et al., 1996), as well as pullout tests in dense sand on CI pipes (Stewart et al., 1999) show that maximum interface shear force is mobilized at 1 to 2 mm of relative displacement. Rigid plastic response is a close approximation of this stiff interface behavior and generally conservative with respect to the development of axial load.

It is important to recognize that the lateral force, f_y, is a force normal to the longitudinal pipeline axis, not not the force normal to the circular pipe surface where friction is mobilized. O'Rourke et al. (2016) developed a correction factor to account for the actual frictional forces around the pipe circumference during pipeline lateral displacement, given by the expression:

$$f_x = f_y \tan\delta_s \left(\frac{f_T}{f_A} \right) \tag{4.5}$$

where f_T/f_A is the correction factor equal to the ratio of the true to apparent frictional forces, given by:

$$\frac{f_T}{f_A} = \frac{1.652}{1.346 + 0.757 \tan\delta_s} \tag{4.6}$$

The correction factor was calculated based on tactile pressure sensors measurements

obtained during large-scale tests, in which buried pipelines were displaced laterally (Palmer et al., 2009). The derivation for the correction factor f_T/f_A and regression method for the normalized pipe surface measurements are provided in Appendix C.

Large-scale test measurements with tactile pressure sensors show that passive pressures on one side of the pipe during lateral movement predominate those on the opposite side (O'Rourke et al., 2016). For tests in dry sand the measured pressures were negligible on the side opposite to the direction of movement. In partially saturated sand voids stabilized by suction and apparent cohesion were observed on the side of the pipe opposite the direction of movement. To reflect the one-sided mobilization of lateral soil resistance, the gap elements in the FE model transfer forces only when the corresponding normal springs carry compressive forces.

As initial step in the FE modeling, the lateral displacements required to activate normal forces for at-rest conditions are imposed on the soil nodes of the transverse soil springs. These initial displacements are applied so that a longitudinal frictional force equivalent to that given by Eqn. (4.3) is developed.

4.3.4 Joint Modeling

Fig. 4.5b shows a schematic of the pipe joint mechanical model with independent axial, shear and rotational springs. Because Abaqus allows for nonlinear force vs. displacement and moment vs. rotation relationships, experimental data from large-scale direct tension tests, as well as four-point bending tests, are used to simulate nonlinear axial force vs. displacement and moment vs. rotation behavior of the DI joints. The spring stiffness for shear transfer across a joint is set to a high value, consistent with the

shear stiffness of the pipe barrel. An axial joint spring, consistent with the axial stiffness of the pipe, is likewise used when there is spigot to bell contact under compression.

4.3.5 Bell Resistance to Movement

It is important to account for load drops across the enlarged bells of both restrained and restrained axial slip joints (Figs. 4.2 and 4.4) because large-scale fault rupture tests confirm that they contribute significantly to an increase in maximum axial pipe load near the fault crossing (Pariya-Ekkasut, 2018; Stewart et al., 2015). Not accounting for the increased load can lead to an unsafe overestimation of sustainable ground deformation. To account for the additional axial resistance mobilized by an enlarged bell, a nonlinear spring is attached in the FE model to the pipeline node representing the bell of a joint, as shown in Fig. 4.5b.

Wham et al. (2017) report on pullout tests of 150-mm-diameter DI pipelines with restrained axial slip joints in partially saturated sand, for pipe burial depth to top of pipe of 0.76 m, showing that a higher resistance to pullout is mobilized when the flat end rather than the curved end of the bell is pulled in the direction of axial pipe movement. The measured axial resistance of the bell with respect to bell/soil relative movement is shown in Figure 4.6 for both directions of bell movement in the same sand and burial conditions. Maximum resistance of the flat end was approximately 15% larger than that of the curved end, and the stiffness of the flat end was larger for movement exceeding 30 mm. Consistent with the modeling approach for nonlinear axial and rotational joint behavior described previously, the nonlinear bell resisting force vs axial movement plotted in Figure 4.6 was used in the FE simulations. The axial bell resistance for both

restrained and restrained axial slip joints was modeled using the plots in Figure 4.6.

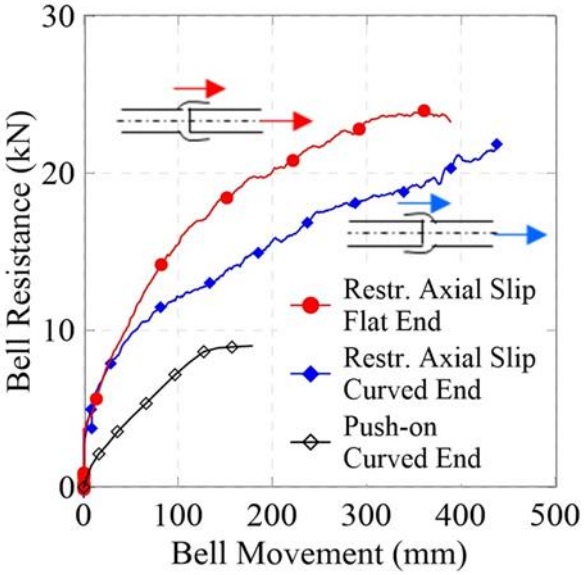

Figure 4.6. Resistance due to Bell Movement in the Pipeline Longitudinal Direction vs. Bell/Soil Relative Movement for Restrained Axial Slip joints.

A push-on joint possesses a smaller size bell than a restrained or restrained axial slip joint. Tests conducted on DI pipelines with push-on joints in partially saturated sand, for burial depth to top of pipe of 0.76 m, produced the bell resisting force vs. axial movement plotted in Fig. 4.6 for the curved end of the bell displaced in the direction of axial movement. The maximum bell resistance is approximately 60% lower than that for a restrained axial slip joint. Additionally, numerical analyses performed with and without modeling the bell resistance in tension showed that it has negligible effect on performance because the joints pull apart under relatively small amounts of axial deformation due to their lack of pullout resistance.

Wham et al. (2018) report on axial pull tests conducted in the same partially saturated sand at at-rest conditions on 150-mm-diameter jointed pipelines at different burial depths. The tests show that the axial resisting loads mobilized by the restrained

joints are directly proportional to depth, and thus the vertical and horizontal stresses provided by the soil. Using these experimental results, the bell resisting force at any depth can be scaled directly from a known reference bell force and depth, provided that the bell geometry, pipe composition, soil properties are similar. The scaling relationship used in this work is expressed as:

$$\frac{F_{bell.Hc}}{F_{bell.ref}} = \frac{H_c}{H_{c,ref}} \tag{4.7}$$

where $F_{bell,ref}$ is the bell resistance measured at a reference depth to pipe center, $H_{c,ref}$, and $F_{bell,Hc}$ is the bell resisting force projected to a different depth of interest, H_c. The experimental data reported by Wham et al. (2018) show that the resisting force scales to higher or lower values at approximately the same axial displacement when the bell resisting force is plotted against axial pipe movement.

As discussed previously, the longitudinal frictional forces on the pipe barrel scale in direct proportion to the lateral soil forces mobilized during fault movement. Following on this principle, a similar scaling relationship is adopted for estimating the axial load drop across enlarged bells subject to transverse lateral movement during fault displacement. The scaling relationship is given by:

$$\frac{F_{bell.fym}}{F_{bell.ref}} = \frac{N_{qH}}{(1+K_o)\pi/2} \tag{4.8}$$

where $F_{bell,fym}$ is the axial bell resisting force in the zone where maximum lateral soil forces are mobilized. For these conditions, the bell resisting force is directly proportional to N_{qH} in Eqn. (4.1). $F_{bell,ref}$ is the bell resistance measured at a reference burial depth, $H_{c,ref}$, where the bell resisting force is directly proportional to $(1+K_o)/2$ for

at-rest conditions. This scaling relationship requires the same soil and pipe material properties, depths of burial, and bell geometries.

4.4 Ductile Iron Pipeline Limit States

There are four primary limit states that characterize DI pipeline behavior and help quantify maximum ground movements associated with the loss of structural integrity and water leakage. These limit states pertain to tensile, rotational, compressive, and local buckling capacities. In addition, the exceedance of shear capacity in the pipe joints and barrel was also investigated and not found to be a limiting factor in pipeline performance. The primary limit states are discussed under the subheadings that follow.

4.4.1 Joint Tensile Capacity

Large-scale test results (Pariya-Ekkasut, 2018; Stewart et al., 2015) are used to characterize the joint force vs. pullout relationship for each type of joint under study. Figure 4.7 shows the axial force vs. pullout measurements for both the restrained and restrained axial slip joints of a 150-mm-diameter DI pipe when subjected to axial extension. An internal water pressure of 550 kPa was applied during both tests. For the tension test, it was assumed that the restrained axial slip joint is set at a position midway between the gasket haunch and locking segment where the joint can accommodate 36 mm of axial displacement in both tension and compression. Under tension the joint moves 36 mm until the weld bead makes contact with the locking segments, after which the restrained axial slip joint behaves in a manner similar to that of the restrained joint. The maximum tensile force measured for the restrained axial slip joint was 370 kN at

an axial displacement of 45 mm. The maximum tensile force measured for the restrained joint was 425 kN at an axial displacement of 18 mm.

The onset of leakage for both joints was caused by forces generated between the weld bead on the spigot and the restraining clips that deform the spigot inward a sufficient distance to allow the bead to slip past the clips. The limit state is therefore associated with ovaling of the pipe as it is pulled past the restraining clips, causing leakage and loss of water pressure.

In contrast, push-on joints have very low tensile capacity. Wham and O'Rourke (2015) report the results of axial tension tests on 150-mm DI push-on joints, for which the spigot pulled out of the bell after 50 mm of displacement and a maximum force of 0.9 kN. In the FE model, axial resisting force was neglected and the maximum pullout movement was taken as 50 mm.

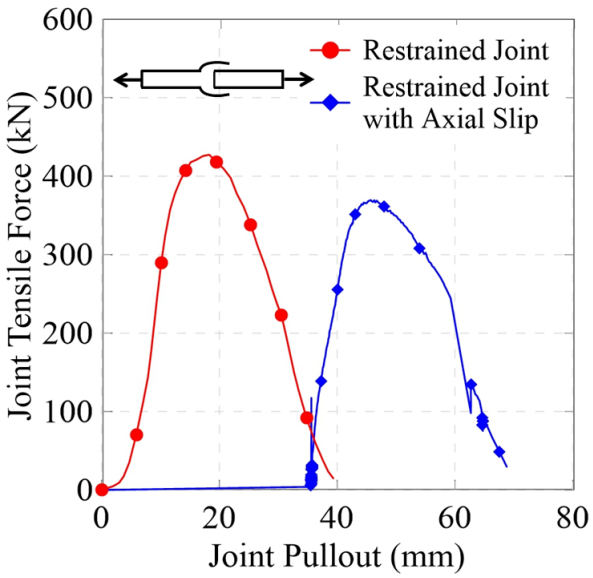

Figure 4.7. Joint Tensile Force vs. Pullout Plots for Restrained Axial Slip and Restrained Joints.

4.4.2 Joint Rotational Capacity

Large-scale test results are again used to characterize the joint behavior during rotation or deflection. Figure 4.8 shows the joint moment vs. rotation relationships for both restrained and restrained axial slip joints as determined by four-point bending tests, conducted under internal water pressure of 550 kPa (Pariya-Ekkasut et al., 2018; Pariya-Ekkasut, 2018; Stewart et al., 2015). The test on the restrained axial slip joint was performed at the fully extended position of the joint. The restrained joint had a high rotational capacity, accommodating approximately 20^{o} before the initiation of leakage. Test results show that the restrained axial slip joint sustained 9^{o} before the onset of leakage. Similar tests indicate that push-on joints are able to rotate until there is spigot to bell contact at about 5^{o} and that the maximum rotation before leakage is 16^{o} (Wham and O'Rourke, 2015). The results of four-point bending tests were used to identify the limiting rotations for each joint type as well as their moment vs. rotation relationships.

The axial capacity of DI pipe joints is reduced by the simultaneous application of rotation. Wham and O'Rourke (2015) identified combinations of joint pullout and rotation resulting in leakage for 150-mm-diameter push-on joints through experimental and numerical simulations. This leakage envelope is used to determine the joint capacity under combined axial pullout and rotation. Large-scale fault rupture test data are used to estimate joint pullout capacity when combined with rotation for both restrained and restrained axial slip joints.

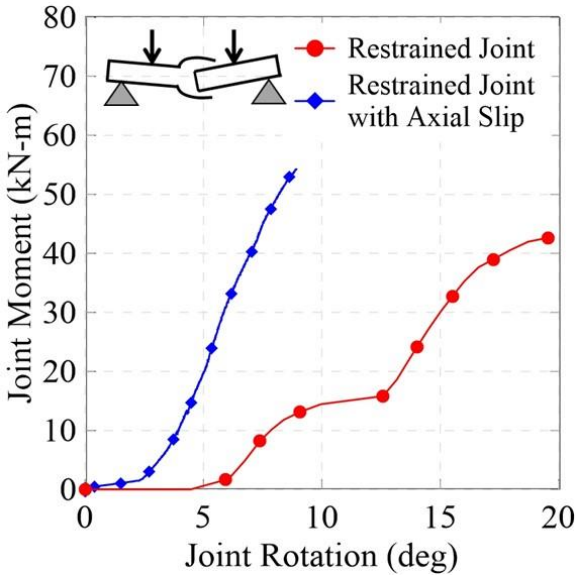

Figure 4.8. Joint Moment vs. Rotation Plots for Restrained Axial Slip and Restrained Joints.

4.4.3 Joint Compressive Capacity

When DI jointed pipelines are subject to compression, the spigot makes internal contact with the bell heel. When this occurs, compressive forces are transferred through the joints. For the push-on and restrained joints, this contact occurs at virtually zero compressive displacement. Because it is assumed in this work that the restrained axial slip joint is set midway in its range of axial travel, the type of joint used in this work can accommodate 35 mm of axial shortening before the spigot makes contact with the back of the bell.

Large-scale direct compression test results for the restrained axial slip joints used in this study show that the joints were able to accommodate axial loads without excessive local deformation or leakage until a load consistent with the DI proportional stress limit was developed (Pariya-Ekkasut, 2018; Stewart et al., 2015). After this level was reached, progressive bending as well as local distortion and rotation of the pipe

joint occurred. Direct compression tests on other commercially available DI joints (Pariya-Ekkasut, 2018) show similar behavior. For FE simulations reported in this paper, the compressive limit state for all joint types under investigation was taken as an axial compressive stress that equals the DI proportional limit.

4.4.4 Local Buckling

When DI jointed pipelines are subject to combined compression and bending, local buckling can occur. This type of deformation occurs when the DI pipeline is under compression at the same time there is significant lateral offset. Gresnigt et al. (2011) summarized experimental results for pressurized pipes subjected to pure bending by plotting maximum compressive strain that was measured at the onset of local buckling as a function of its outer diameter to wall thickness ratio, D/t. The DI pipe under investigation in this work has D/t = 23. For this ratio, Gresnigt et al. (2011) show measured compressive strains in the range of 1.9%-3.5% corresponding to the initiation of local buckling. The local buckling limit state in this work is taken as the lower bound curve identified by Gresnigt et al. (2011) for measured compressive strain vs. D/t, equal to 1.9%.

4.5 Comparison of Numerical & Experimental Results

A large-scale fault rupture test on a DI pipeline with 175 mm outside diameter, 7.8 mm wall thickness, and restrained axial slip joints was performed in the Cornell University Large-Scale Lifelines Testing Laboratory. The results of this test are described in detail (Pariya-Ekkasut, 2018; Stewart et al., 2015), and only the salient features are presented

here.

Figure 4.9 shows a plan view of the experimental set up. The total length of the DI pipeline buried in soil was approximately 11.89 m. The pipeline consisted of a 3.06-m-long pipe section centered on the rupture plane, two 3.06-m pipes north and the south of the center pipe, and a 0.99-m and 1.49-m pipe section on the north and south side of the fault, respectively. As shown in the figure, there were four restrained axial slip joints in the pipeline. Left lateral strike-slip movement was imposed with a pipeline/fault crossing angle of 50°, resulting in tension and bending in the pipes. The pipeline was pressurized with water to approximately 550 kPa. It was laid out so that the spigot at each joint could pull from the bell approximately 58 mm before the spigot bead made contact with the locking segments. The depth of burial to top of pipe was 0.76 m. The pipeline was buried in partially saturated sand that was compacted to have an average friction angle of 42º, equivalent in strength to that of a medium dense to dense granular backfill. Fig. 4.9 also shows the locations of the instruments along the test pipeline. The instrumentation consisted of strain gages at thirteen locations (gage planes) along the pipeline, load cells at the ends of the pipeline, and direct current differential transformers (DCDTs) to measure axial and rotational joint displacements.

The ground rupture test ended when the spigot pulled from the S joint bell at a fault displacement of approximately 460 mm. Figure 4.10 shows how the S and N joints closest to the fault responded in terms of axial force vs. pullout (Fig. 4.10a) and moment vs. rotation (Fig. 4.10b). The joint pullouts and rotations were calculated from DCDT measurements, while the joint forces and moments were evaluated from strain gage measurements. At fault displacements between 380 mm and 400 mm, the spigots of the

S and N joints started ovaling when the weld bead was pulled through the restraining clips, as explained previously for joint tensile capacity. Strain gage measurements for bending at key locations became unreliable because of localized transverse distortion of the pipe and loss of gages at these higher levels of movement.

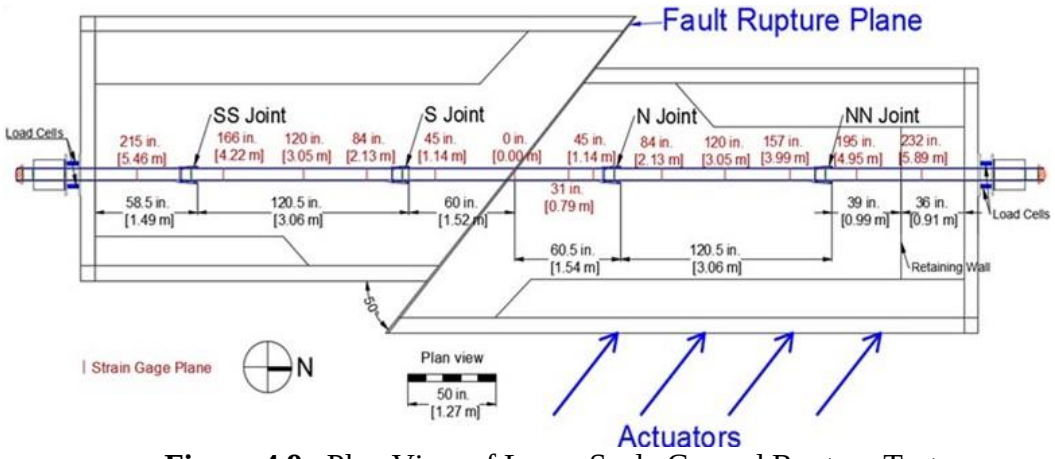

Figure 4.9. Plan View of Large-Scale Ground Rupture Test.

Joint performance during the ground rupture test is also compared in Fig. 4.10 with the results of axial tension and four-point bending tests conducted outside the soil. Fig. 4.10a compares the response of the S and N joints in terms of axial force vs. joint pullout with the tension test results in Fig. 4.7. The joint force vs. pullout plots from the fault rupture test agree well with the results of the axial tension test to about 380 mm of fault displacement after which several gages became unstable. The maximum axial force from undamaged strain gage readings as well as the load cell measurements at the ends of the pipeline at failure are plotted in Fig. 4.10a, and show a reduction in axial load capacity of about 18% relative to that from the axial tension test.

Figure 4.10b shows that the joint moment vs. rotation measurements from the fault

rupture test are in good agreement with the moment vs. rotation relationship from the four-point bending test, which is plotted in Fig. 4.8. That test was performed with the joint fully extended and is thus consistent with conditions in the fault rupture test just before pullout. The comparison of four-point bending and fault rupture test measurements show close agreement with respect to the joint moment vs rotation relationship. A similar comparison for the joint axial force vs pullout relationship shows close agreement until the failure load, which is notably lower under combined pullout and rotation.

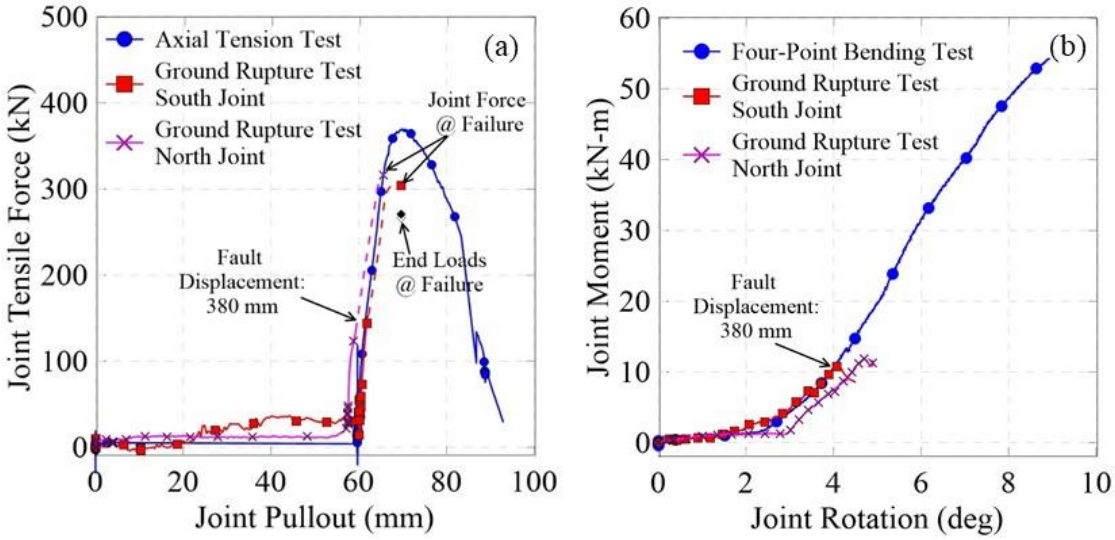

Figure 4.10. Restrained Axial Slip Joint Response Inside and Outside the Soil (a) Force vs. Pullout (b) Moment vs. Rotation.

The large-scale ground rupture test was simulated using the numerical model presented in Fig. 4.5. The joint rotational and axial joint springs were modeled with the four-point bending and axial tension test results, respectively. Figure 4.11 compares the fault rupture experimental and numerical model results. Figures 4.11a and 4.11b show the response in terms of joint behavior, i.e. joint pullouts and rotations, respectively,

relative to fault displacement. The numerical model predicts the sequence of joint slip (Fig. 4.11a) successfully, with the closest joint south of the fault (S) slipping first, followed by the closest joint north of the fault (N), the outer joint south of the fault (SS) and finally the outer joint north of the fault (NN). In addition, the numerical results for joint rotations are in excellent agreement with the measured joint rotations for N and S joints (Fig. 4.11b). It is noted that both experimental and numerical results showed virtually no rotation of joints NN and SS.

The numerical and experimental axial force distributions are in good agreement at all levels of fault displacement to 380 mm. The markers on the horizontal axis of Figures 4.11c and 4.11d indicate the locations of the joints. Fig. 4.11c shows the axial force along the pipeline for a fault displacement of 350 mm. The two distributions follow the same trends, with the maximum axial force at the location of the fault crossing being identical for both. In addition, the experimental axial force distribution, shows significant load drops across the joints closest to the fault, which is captured by the numerical model. Using the scaling relationship in Eqn. 4.8, the axial resistance predicted for the restrained axial slip joints near the fault plane is large, corresponding to a load drop of 66 kN, which compares well with 64 kN measured in the fault rupture test. Differences between the numerical and experimental results are likely the result of load drop in the numerical model being simulated by a single spring (Fig. 4.5b), whereas axial resistance at the bell is mobilized in a more distributed fashion as the joint moves relative to the surrounding soil. The pipe segment centered on the fault plane experiences the highest relative lateral movements with highest lateral pressures, mobilizing higher frictional forces along the center compared to the outer segments. The

numerical distribution tracks the experimental one remarkably well on the north side of the fault, with similar axial force attenuation along each pipe segment.

Figure 4.11d compares the experimental and numerical bending moment distributions along the pipeline for fault displacement of 350 mm. The two distributions follow similar trends. The maximum bending moment from the numerical analysis is approximately 14% higher than the maximum measured moment south of the fault plane, and thus provides a conservative, but reasonably close prediction.

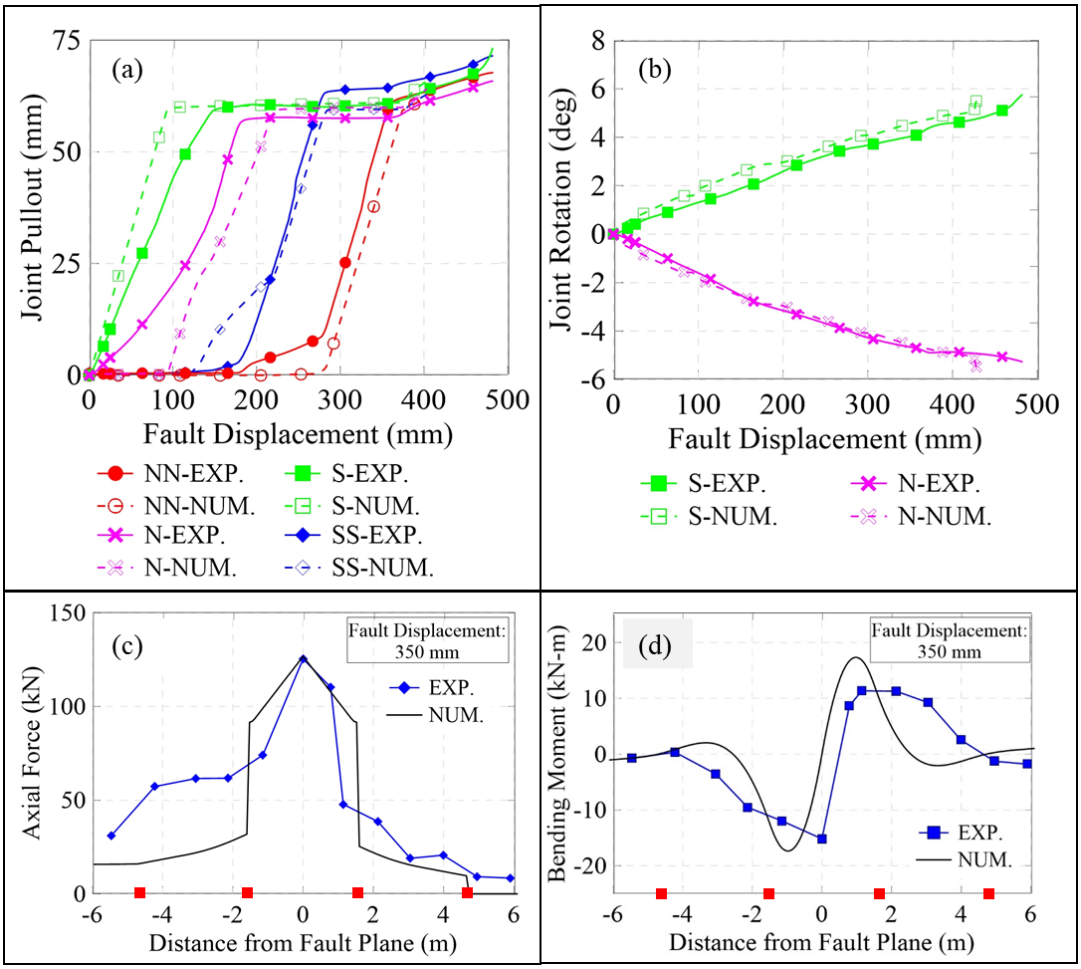

Figure 4.11. Comparison of Experimental and Numerical Results: (a) Joint Pullouts vs. Ground Rupture Displacement (b) Joint Rotation vs. Ground Rupture Displacement (c) Axial Force Distribution Along the Pipeline (d) Bending Moment Distribution Along the Pipeline.

4.6 Ductile Iron Pipeline Response to Fault Rupture

Given the favorable comparison between the numerical and fault rupture test results, the numerical model described earlier was applied to evaluate jointed DI pipeline performance for general conditions of fault rupture. It is well known that pipeline response to abrupt ground deformation depends on its angle of intersection with the plane of movement. As illustrated in Figures 4.12 and 4.13 for strike-slip fault movement, angles of pipeline/fault intersection $0^o \leq \beta \leq 90^o$ result in pipeline tension and bending, whereas intersection angles $90^o < \beta \leq 180^o$ result in pipeline compression and bending. Having a validated numerical model for soil/jointed pipeline interaction under conditions of extreme ground deformation and a full suite of large-scale test results for representation of pipeline performance with push-on, restrained, and restrained axial slip joints provides a unique opportunity for a comparative assessment in which pipeline response is characterized for all possible pipeline/fault intersection angles.

The numerical analyses were run for DI pipelines with an external diameter of 175 mm and wall thickness was 7.6 mm. The length of a single pipe segment was 5.5 m, consistent with DI pipe lengths used in standard practice. A burial depth to the pipe centerline of 1.3 m was assumed, which is typical of most water mains. Partially saturated sand with a unit weight $\overline{\gamma}$ = 17.6 kN/m^3 and internal friction angle of $\phi' = 42^o$ was used. The DI pipe material was assumed to follow an elastic-plastic stress vs. strain relationship with Young's modulus E, yield stress σ_y and maximum tensile strength σ_u of 156 GPa, 362 MPa and 559 MPa, respectively (Pariya-Ekkasut, 2018).

"Infinite" pipeline conditions were assumed, beyond which there is no additional

axial frictional resistance mobilized by the pipeline. This defines a unique condition for which any increase in pipeline length does not change the numerical results. The total length of the pipeline in the numerical analyses was equal to 50 pipe segments, half of which were located on each side of the fault. This length was found to satisfy infinite pipeline requirements for all cases included in this work.

The results of the fault rupture test described above, showing a decreased pullout force for combined axial slip and rotation, were incorporated in the interpretation of the numerical results. A first order approximation of how tensile axial capacity is reduced by rotation was adopted as $F_\theta = F_{\theta=0}(1- \theta)$, in which F_θ and $F_{\theta=0}$ is the axial force at joint rotation θ and 0, respectively. This approximation was used in the numerical analyses in a manual iterative process, in which the measured joint rotation at failure was used to update the tensile joint capacity. Because the restrained axial slip and restrained joints exhibit similar behavior once the locking segments are engaged in carrying tensile force, the same estimation process was applied to both types of joints.

As explained by Wham et al. (2016) two geometric conditions bound the performance of jointed pipelines in response to ground deformation: joint centered (JC) and pipe centered (PC) in which a joint and the center of a pipe segment, respectively, is positioned at the location of maximum soil movement. The presentation and discussion of the numerical results are summarized for JC and PC configurations below. Observations during large-scale fault rupture tests show that a shear zone develops with width similar to the length of the restrained axial slip joint used in this study. The soil disturbance within this shear zone will prevent axial bell resistance from being developed, and marginalize the axial load drop for a joint located at the fault plane. For

JC conditions therefore, the axial joint resistance at the fault crossing was not included in the numerical analyses.

The numerical results are plotted in Figures 4.12 and 4.13 for JC and PC conditions, respectively. The results are presented as the maximum ground movement that can be accommodated across the fault plane vs pipeline/fault crossing angle, β. The definition of the pipeline/fault crossing angle is illustrated by the inset diagram in each figure. Also shown in each figure are the limit states that control pipeline performance depicted as a function of the ranges in pipeline/fault crossing angle. Hence, the information presented in each figure includes maximum ground displacement and pipeline limit state vs. pipeline/fault crossing angle for DI pipelines with push-on, restrained, and restrained axial slip joints.

For both JC and PC conditions there are common performance characteristics. For $\beta < 90°$ joint tensile capacity is the governing limit state. The ability of a pipeline with push-on joints to sustain tensile displacement is limited by the capacity of the most vulnerable joint. Because only a very low axial force can be carried through the center joint or joints closest to the fault, axial movements accumulate at a joint location until pullout. Both restrained and restrained axial slip joints can carry approximately two orders of magnitude larger tensile forces than the push-on joints, resulting in more joints being mobilized and accommodating larger fault movements before failure of the most vulnerable joint at or closest to the fault. For this range of β, DI pipelines with restrained axial slip joints can accommodate 2 to 3 and 4 to 10 times as much fault offset as pipelines with push-on joints and restrained joints, respectively. The differences in pipeline response are amplified as β decreases.

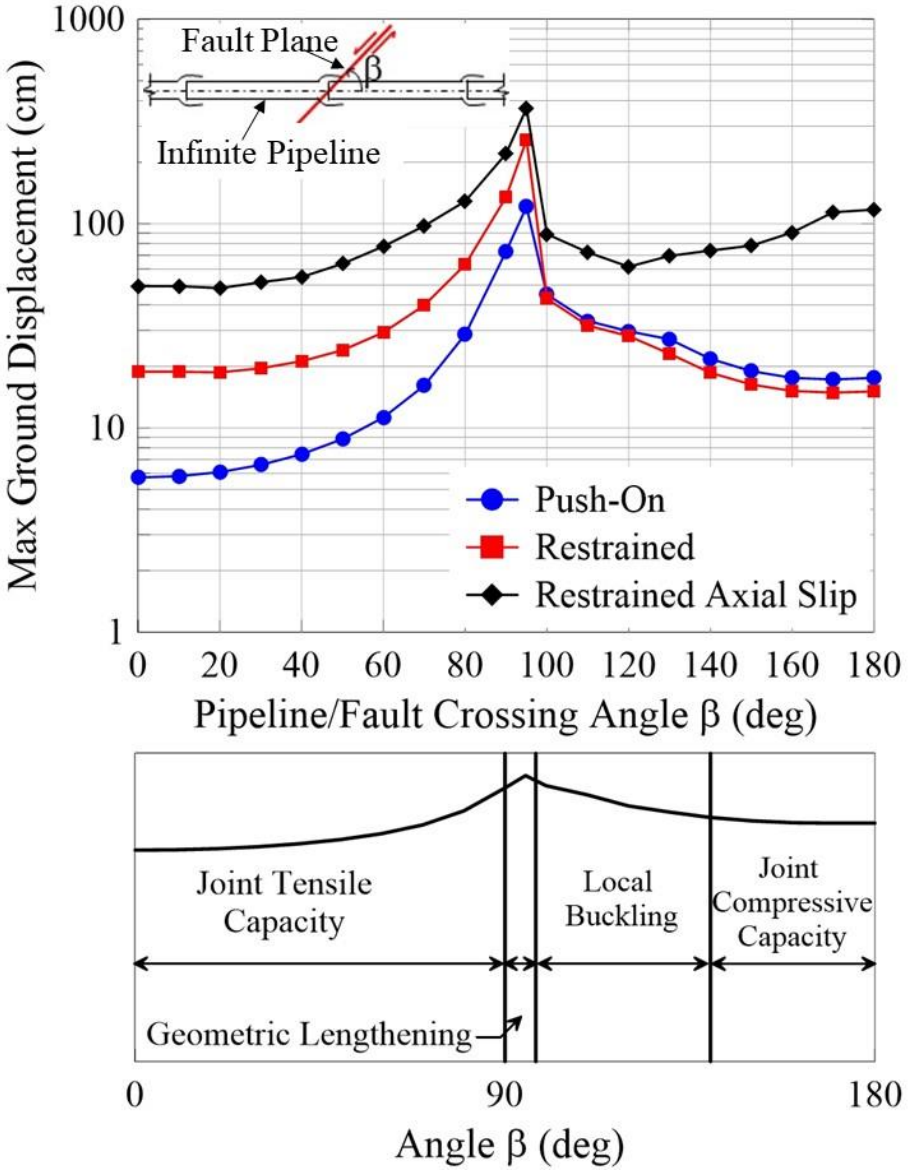

Figure 4. 12. Maximum Ground Displacement relative to Pipeline/Fault Crossing for Joint Centered Condition.

For $\beta \geq 130°$ joint compressive capacity is the controlling limit state for both JC and PC conditions for pipelines with push-on and restrained joints. Compressive axial force accumulates with increased fault movement until the proportional limit stress in the pipe is exceeded. The fault offset that can be accommodated is similar for push-on and restrained joints. In fact, a pipeline with restrained joints will accommodate slightly

less fault movement than a pipeline with push-on joints because the axial load drops across the enlarged bells result in a higher maximum compressive force for a given fault displacement. For pipelines with restrained axial slip joints, joint compressive capacity governs the behavior when $\beta \geq 160°$.

For both JC and PC conditions, the maximum fault offset coincides with $90^{\circ} \leq \beta \leq 110^{\circ}$, where geometric lengthening and joint rotation affect the maximum movement that can be accommodated. For JC conditions, pullout occurs at the center joint in response to geometric lengthening of the pipeline. Thus, the tensile pullout capacity of the joint establishes the maximum sustainable fault offset. For PC conditions, either joint rotational capacity or joint pullout due to geometric lengthening, affects performance, which is particularly consequential for restrained axial slip joints. As shown in Figure 4.8, the maximum rotational capacity of a restrained axial slip joint is approximately half that for a restrained joint, resulting in a lower fault offset. The restrained axial slip joint capacity is also lower than that of a push-on joint.

As the configuration of a pipeline with restrained axial slip joints transitions from a JC to PC condition, the sustainable fault offset decreases from approximately 3.5 m to 1.5 m. Thus, pipeline performance is particularly sensitive to joint location relative to the fault for β near 90°. Increasing the rotational capacity of the restrained axial slip joint would increase fault offset capability and reduce the sensitivity of joint location for orthogonal pipeline/fault crossings.

Plots for JC and PC conditions are similar for $110^{o} \leq \beta \leq 130^{o}$, for pipelines with push-on and restrained joints, for which pipeline performance is controlled by local buckling, which is the only limit state not associated with joint performance. Figure 4.14

illustrates how local buckling develops by showing the lateral pipe movement (Fig. 4.14a) and maximum compressive strain distribution (Fig. 4.14b) along a pipeline with restrained joints at a fault crossing angle $\beta = 120^{o}$.

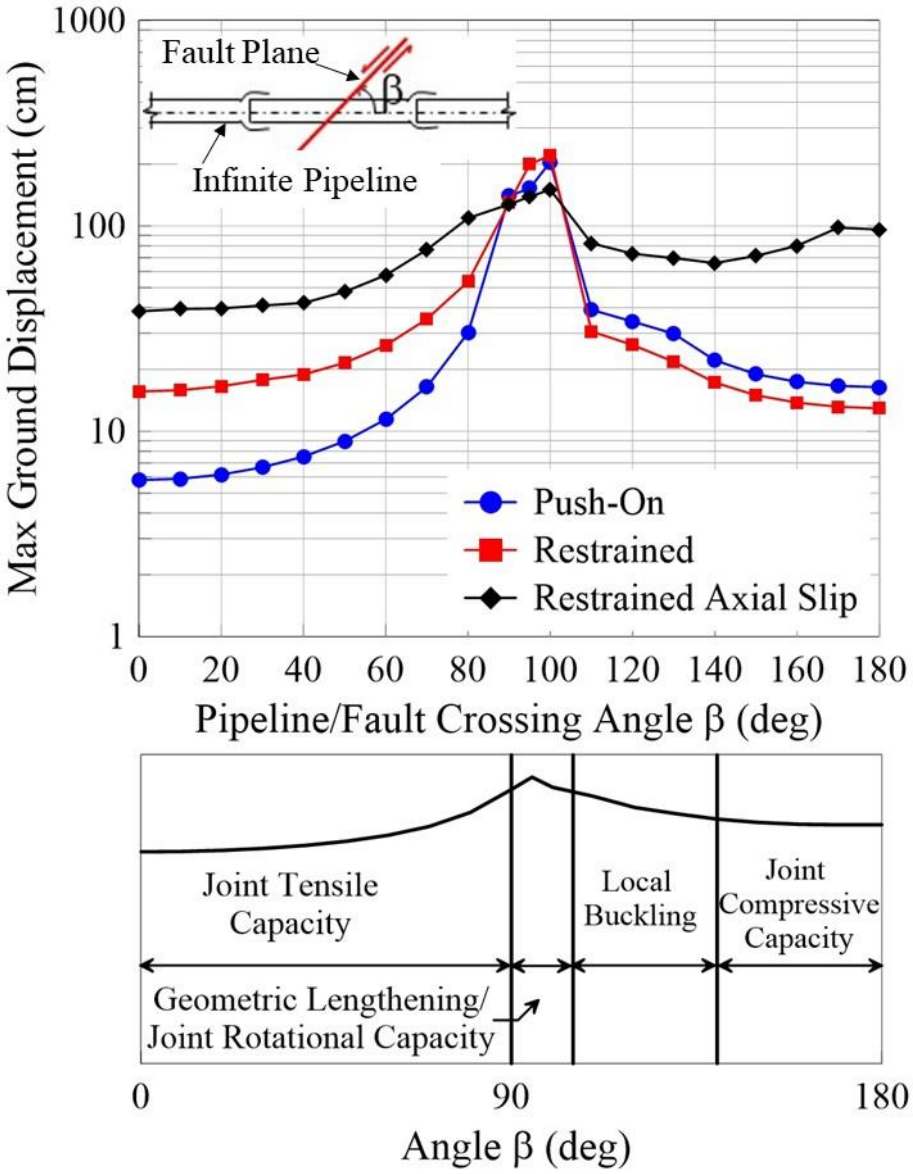

Figure 4.13. Maximum Ground Displacement relative to Pipeline/Fault Crossing for Pipe Centered Condition.

The dashed lines mark the locations of the joints. The pipeline accommodates

lateral deformation primarily by flexure. It is the high curvatures at locations 1-2 m from the fault plane (Fig. 4.14a), and not joint rotation, that accommodates the lateral component of fault offset. At a fault displacement of 280 mm, the maximum compressive strain due to combined bending and axial force reaches 1.9% at a distance of approximately 1 m on both sides of the fault (Fig. 4.14b). As described previously, this strain corresponds to the lower bound local buckling limit identified by Gresnigt et al. (2011). For pipelines with restrained axial slip joints, local buckling controls the performance when $110^{o} \leq \beta \leq 160^{o}$. When $\beta \geq 120°$, pipelines with restrained axial slip joints accommodate greater fault displacement as β increases. Under these conditions of rising β, additional joints slip into compression before generating compressive stress resulting in local buckling.

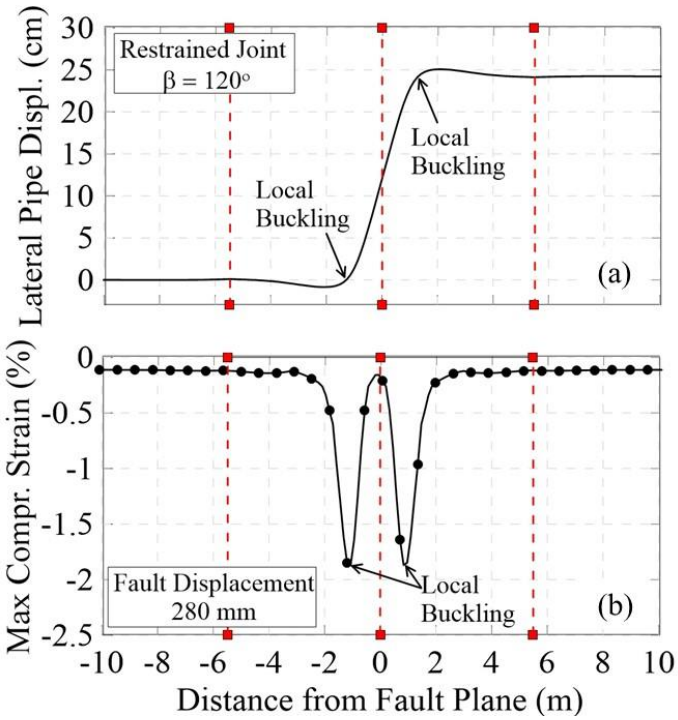

Figure 4.14. (a) Lateral Pipe Displacement (b) Maximum Compressive Strain along the Pipeline for DI pipeline with Restrained Joints and Fault Crossing Angle of 120°.

4.7 Concluding Remarks

This paper provides a comprehensive evaluation of DI pipeline response to earthquake-induced ground deformation through the results of a large-scale testing program and fault rupture test, development of advanced numerical modeling to simulate the geometrically nonlinear performance of DI pipelines with earthquake resistant joints, and validation of the numerical model relative to fault rupture test measurements. The numerical model is applied to quantify and compare the performance of DI pipelines with push-on, restrained, and restrained axial slip joints at any orientation of the pipeline relative to the fault rupture plane under strike-slip faulting conditions. The principal findings of this investigation are:

- A two dimensional finite element model has been developed that accounts for the (i) coupling of shear forces at the soil/pipe interface with forces normal to the longitudinal axis of the pipeline, (ii) combined axial slip, pullout resistance, and rotation of the joints, and (iii) axial resistance of the joints to relative pipe/soil movement. These formulations expand on the modeling capabilities developed by Jung et al. (2016) and O'Rourke et al. (2016) so that numerical simulation can be extended to large, geometrically nonlinear changes in the axial slip and rotation of restrained axial slip joints and also to account for the load drop across DI joints. The modeling capabilities have been validated by favorable comparison with large-scale fault rupture test measurements.
- Based on the results of large-scale tests, scaling relationships are proposed to estimate axial joint resistance at any pipe depth and to account for increased resistance to axial movement in the zone of highest lateral soil reaction. Given

the potentially large load drop, it is necessary to account for the joints when analyzing and designing DI pipelines with restrained and restrained axial slip joints. Accounting for load drop is especially important for restrained axial slip joints, which are used for earthquake and hazard resilient applications.

- The results of systematic and detailed FE simulations are presented for the response in granular soil of DI pipelines with three different types of joints to strike-slip fault displacement. The response for each joint type is presented in terms of fault offset that can be sustained as a function of the pipeline/fault crossing angle. Pipelines with restrained axial slip joints can accommodate 2 to 9 and 2 to 10 times as much fault offset as pipelines with push-on and restrained joints, respectively, for most pipeline/fault crossing angles.
- Pipeline performance is governed by four limit states, including tensile, compressive, and rotational capacity of the joints and local buckling of the pipe. Each governing limit state is related to a specific range of pipeline/fault crossing angles, which are identified and shown in parallel with the plots of maximum fault offset vs. pipeline/fault intersection angles.
- The largest fault offsets are accommodated by all joint types when the pipeline/fault intersection angle is near 90°. This orientation also shows large variation in pipeline performance. Depending on the restrained axial slip joint location relative to the fault, the pipeline limit state may be governed by rotational capacity, which reduces substantially its ability to accommodate fault displacement.

The findings of this study are related directly to the performance of jointed DI water

distribution mains with diameters of 100 mm to 200 mm, and more generally representative of DI water pipelines as large as 600 mm in diameter. Additional testing is recommended to clarify the effects of combined joint slip and rotation on the pullout capacities of the restrained and restrained axial slip joints. Future research is needed to quantify further the compressive stresses that affect leakage and failure of DI joints and to extend the evaluation of pipeline response vs pipeline/fault intersection angle to larger diameter pipelines in the range of 300 mm to 600 mm. Increasing the rotational capacity of restrained axial slip joints will increase fault offset capability for pipeline/fault intersection angles near 90°.

REFERENCES

ASCE. (1984). "Guidelines for the Seismic Design of Oil and Gas Pipeline Systems." *Committee on Gas and Liquid Fuel Lifelines*, American Society of Civil Engineers ASCE, New York.

Gresnigt, A.M., Jo, C.H. and Karamanos, S.A. (2011). "Local Buckling of Tubular Sections in Structural Applications." *World Congress on Advances in Structural Engineering and Mechanics*, Sept. 18-22, Seoul, Korea.

Honegger, D. and Nyman, D.J. (2004). "Guidelines for the Seismic Design and Assessment of Natural Gas and Liquid Hydrocarbon Pipelines." *Pipeline Research Council International*, *Catalog No. L51927*, October.

Jung, J.K., O'Rourke, T.D. and Argyrou, C. (2016). "Multi-Directional Force-Displacement Response of Underground Pipe in Sand." *Canadian Geotechnical Journal*, 53(11): 1763-1781.

O'Rourke, T.D., Jung, J.K. and Argyrou, C. (2016). "Underground Pipeline Response to Earthquake-Induced Ground Deformation." *Soil Dynamics and Earthquake Engineering*, 91:272-283.

O'Rourke, T.D., Jezerski, J.M., Olson, N.A., Bonneau, A.L., Palmer, M.C., Stewart, H.E., O'Rourke, M. J. and Abdoun, T. (2008). "Geotechnics of Pipeline System Response to Earthquakes." Keynote Paper, *Geotechnical Earthquake Engineering and Soil Dynamics IV (GEESD)*, Sacramento, CA, May.

O'Rourke, T.D., Netravali, A.N., Pendharkar, S.M., Tonkinson, A., Chaudhuri, D. and Toparak, S. (1996). "Evaluating Service Life of Anaerobic Joint Sealing Products and Techniques." *Final Report, No. GRI-96/0318, Prepared for Gas Research Institute, Contract No. 5093-207-2798*, Cornell University, Ithaca, NY.

O'Rourke, T.D. and Druschel, S.J. (1989). "Improved Anchoring Practices for Plastic Gas Distribution Pipelines." *Final Report, Prepared for New York Gas Group*, Cornell University, Ithaca, NY.

Palmer, M.C., O'Rourke, T.D., Olson, N.A., Abdoun, T., Ha, D. and O'Rourke, M.J. (2009) "Tactile pressure sensors for soil – structure interaction assessment." *Journal of Geotechnical and Geoenvironmental Engineering*, 135(11): 1638 – 1645.

Pariya-Ekkasut, C. (2018). "Characterization of Hazard-Resilient Ductile Iron Pipelines Response to Earthquake-Induced Ground Deformation." PhD Dissertation: Cornell University.

Pariya-Ekkasut, C., Berger, B.A., Stewart, H.E. and O'Rourke, T.D. (2018). "Evaluation of McWane Seismic Flex Coupling for Resistance to Earthquake-Induced Ground Deformation." *Report, Prepared for Stuart Liddell, National Manager-MASD*, Cornell University, Ithaca, NY.

Stewart, H.E., Bilgin, O., O'Rourke, T.D. and Keeney, T.M.-J. (1999). "Technical Reference for Improved Design and Construction Practices to Account for Thermal Loads in Plastic Gas Pipelines." *Final Report, Prepared for Gas Research Institute, Contract No. 5095-207-2821*, Cornell University, Ithaca, NY.

Stewart, H.E., Pariya-Ekkasut, C., Wham, B.P., O'Rourke, T.D., Argyrou, C. and Bond, T.K. (2015). "Hazard Resilience Testing of US Pipe Ductile Iron TR-XTREME^{TM} Pipe Joints." *Report prepared for Russ Huggins, PE, VP of Produce Development and Quality, US Pipe*, Feb. 2015, Cornell University, Ithaca, NY.

U.S. Pipe. (2017). "3D View of Restrained Axial Slip Joint with Locking Segments, Slots, Weld Bead, and Gasket." <http://uspipe.com/>, available at: http://www.uspipe.com/upload/products/ductile-iron-pipe/tr-flex-restrained-joint-pipe/tr-flex-ductile-iron-pipe-and- fittings/USP_TRFlex_SubmittalDocument_Web_090817.pdf

Wham B.P., Argyrou C. and O'Rourke T.D. (2016). "Jointed Pipelines Response to Tunneling Induced Deformation." *Canadian Geotechnical Journal*, 53(11): 1794-1806.

Wham, B.P. and O'Rourke, T.D. (2015). "Jointed Pipeline Response to Large Ground Deformation." *Journal of Pipeline Systems Engineering and Practice*, 10.1061/(ASCE)PS.1949-1204.0000207.

Wham, B.P., Pariya-Ekkasut, C., Argyrou, C., Lederman, A., O'Rourke, T.D. and Stewart, H.E. (2017). "Experimental Characterization of Hazard-Resilient Ductile Iron Pipe Soil/Structure Interaction under Axial Displacement." *Congress on Technical Advancement*, Sept. 10-13, Duluth, MN, available at: https://ascelibrary.org/doi/pdf/10.1061/9780784481028.013.

Wham, B.P., Berger, B.A., Pariya-Ekkasut, C., O'Rourke, T.D., Stewart, H.E., Bond, T.K. and Argyrou, C. (2018). "Achieving Resilient Water Networks –Experimental Performance Evaluation." *11th U.S. National Conference on Earthquake Engineering*, June 25-29, Los Angeles, CA.

CHAPTER 5

CONCLUSIONS AND RECOMMENDATIONS FOR FUTURE RESEARCH

This thesis deals with the performance of underground pipelines under earthquake-induced permanent ground deformation (PGD). The first part of the thesis focuses on the response to PGD of pipelines with defects (e.g., weak joints and/or circumferential cracks) reinforced with cured-in-place linings (CIPLs). A full-scale testing regime and fault rupture tests were performed to characterize the performance of CIPL-strengthened pipelines to earthquake-induced ground deformation. Numerical models were developed to analyze combined pipe/CIPL and soil/pipeline interaction during fault rupture. The second part of the thesis involves a comprehensive assessment of the fault deformation response of ductile iron (DI) pipelines with three different types of joints, including push-on, restrained, and restrained axial slip joints. Large-scale test results were used to quantify DI pipeline performance during fault rupture, and numerical simulations were conducted to explore pipeline response to strike slip fault movement for any pipeline/fault intersection angle. The main conclusions of this work are presented and recommendations for future research are discussed under the headings that follow.

5.1 Response of Pipelines Retrofitted with Cured-In-Place Linings to Earthquake-Induced Ground Deformation

The most critical deformation mode for pipeline performance is in the axial direction. A series of static and dynamic tests were presented in this thesis to characterize the response of the CIPL-retrofitted pipelines under tensile deformation. The results of

these tests indicate that CIPLs provide effective reinforcement for underground utilities under transient and low to moderate permanent ground deformations. A one-dimensional finite element model was developed to simulate CIPL de-bonding from the host pipe under tensile axial loading. The key findings of the experimental and numerical study are summarized as follows:

- Of great importance for CIPL-reinforced pipeline performance is the CIPL de-bonding under axial tensile loading. The de-bonding allows the CIPL to increase in length, therefore accommodating tensile ground deformation at the locations of defects, such as weak joints and round cracks in brittle pipelines and conduits. The initiation and the amount of de-bonding depends on the CIPL strength relative to the axial force required to damage the CIPL/pipe bond. The CIPL/pipe interface strength increases in the presence of internal pressure.
- An important failure mode controlling the response of CIPL-strengthened pipelines to cyclic loading is pinching of the lining due to the closing of round cracks and gaps in weak joints. Pinching occurs when the CIPL, which de-bonds from the pipe under tensile deformation, protrudes into a defect and is compressed as the defect closes. Cyclic loading tests at Cornell and dynamic tests at University at Buffalo show that pinching of the CIPL used in this study occurs when tension-induced opening at a defect exceeds 11-13 mm.
- A numerical model for CIPL/pipe interaction that accounts for the de-bonding mechanism as a Mode II fracture propagation phenomenon is proposed. The model also accounts for enhanced frictional resistance mobilized by internal pipe pressure. The results of the numerical model are in good agreement with

full-scale test results both in terms of axial force vs. defect opening and de-bonded length vs. defect opening under variable internal pressure.

- The CIPL/pipe interaction model was extended to account for soil reaction in the pipeline longitudinal direction and was used to identify the peak ground velocity and pulse period combinations required to cause CIPL pinching. The numerical study showed that peak ground velocities ≥ 200 cm/s can be expected to activate the pinching mechanism. The results for defect openings are independent of the pulse period for pulse periods larger than 0.2 sec.

5.2 Large-Scale Fault Rupture Tests on Pipelines Retrofitted with Cured-In-Place Linings

The effectiveness of CIPLs to retrofit underground utilities under PGD is assessed and their performance is quantified through two large-scale fault rupture tests on CIPL-reinforced pipelines. The experimental results are presented and compared with results of tests on unlined pipelines with weak joints. The response of the pipeline is decomposed into axial and bending/rotational deformation, which are linked to the axial and lateral offset components of strike-slip fault movement. Fault rupture test results are compared with numerical soil-pipeline interaction results. The key findings of the experimental and numerical work are:

- Cured-in-place linings can strengthen pipelines with round cracks and weak joints substantially against permanent ground deformation. De-bonding under axial extension allows the CIPL to increase in length, thereby accommodating tensile ground movements. The de-bonding also allows the linings to accommodate bending and rotation at the locations of defects, such as weak

joints and round cracks in brittle pipelines and conduits. Successful design and product development for seismic retrofitting requires an axial lining strength that exceeds the fracture propagation force and a modulus that allows the lining to elongate sufficiently to accommodate the axial components of externally imposed ground deformation.

- Experimentally measured and numerically simulated bending moments are in close agreement, reflecting the quality of the modeling procedure for the pipeline response under deformations normal to the pipeline axis. Large-scale tests results show that there may be variable shear stiffness for CIPL-reinforced pipeline joints, depending on whether metal to metal or metal to CIPL contact occurs in response to shear forces. Modeling the joints for high shear stiffness results in a conservative estimate for the maximum bending moment.
- To model the axial response of CIPL-reinforced pipelines, it is necessary to account for CIPL de-bonding. In this work, a one-dimensional finite element model accounting for CIPL de-bonding as a Mode II fracture propagation phenomenon is developed. Furthermore, the coupling of normal/shear forces along the pipeline is an integral part of the analytical process. The numerical and experimental results compare favorably with respect to axial forces along the pipeline and joint pullout. Neglecting the shear/normal force coupling results in underestimation of the maximum axial forces in the pipeline.
- There is good agreement between the axial force vs. joint opening and moment vs. joint rotation relationships from direct tension tests and four-point bending tests, respectively, with those derived from measurements during the fault

rupture tests. Therefore, characterizing the joint behavior under axial pullout and rotation outside the soil provides a sound basis for the numerical modeling of CIPL-reinforced pipelines under fault rupture conditions.

5.3 Ductile Iron Pipeline Response to Permanent Ground Deformation

Three different DI joint types, including push-on, restrained, and restrained axial slip joints, are investigated in this study. The systematic evaluation of DI pipeline performance under strike-slip faulting conditions is performed through numerical simulations. A series of large-scale axial tension, axial compression and four-point bending tests is used to identify key limit states for jointed DI pipeline performance. A two-dimensional finite element model accounting for (i) coupled shear/normal forces along the pipeline, (ii) bell resistance to axial pipe movement, and (iii) combined axial slip, pullout resistance, and rotation of the joints, is used to quantify the performance of jointed DI pipelines under strike-slip faulting conditions, for all possible pipeline/fault intersections. Fault movement at intersection angles of $0^o \leq \beta < 90^o$ and $100^o \leq \beta \leq 180^o$ induce tension and compression, respectively, as well as bending/joint rotation in the pipeline. Two geometric conditions, bounding the performance of jointed pipelines in response to ground deformation were considered: joint centered (JC) and pipe centered (PC), in which a joint and the center of a pipe segment, respectively, is positioned at the location of the fault. Key findings of the study are summarized as follows:

- The two dimensional finite model used in the numerical study is validated against a fault rupture test on a pipeline with restrained axial slip joints. The numerical and experimental results are in a good agreement in terms of joint

response, including joint pullout and rotation, axial force, and bending moment distribution along the pipeline.

- Based on the results of large-scale tests, scaling relationships are proposed to estimate the axial resistance against bell movement at any pipe depth under at-rest and maximum lateral soil reaction conditions. Neglecting these load differentials results in an overestimation of the amount of fault displacement that can be sustained by a jointed pipeline. Given the potentially high value of axial load differential along the joints, it is important to account for them when analyzing and designing pipelines with restrained and restrained axial slip joints.
- DI pipeline performance is controlled by four limit states; joint tensile, compressive and rotational capacity and local buckling in the pipe barrel. Joint tensile capacity is critical when tensile deformations are induced to the pipeline, either directly or due to pipeline geometric lengthening ($\beta \leq 90^o$). Joint compressive capacity is critical for $\beta \geq 130^o$ for pipelines with push-on and restrained joints and for $\beta \geq 170^o$ for pipelines with restrained axial slip joints. Local buckling controls the pipeline performance for $110^o \leq \beta \leq 120^o$ for pipelines with push-on and restrained joints and for $110^o \leq \beta \leq 160^o$ for pipelines with restrained axial slip joints.
- Pipelines with restrained axial slip joints accommodate 3 to 9 and 2 to 3 times as much fault displacement as pipelines with push-on and restrained joints, respectively, for $0 \leq \beta \leq 80^o$. They accommodate 2 to 9 times as much fault displacement as pipelines with push-on and restrained joints for $100° < \beta \leq 180^o$.

- The largest offsets are accommodated by all joint types at crossing angles close to 90 °. This same orientation is also associated with the highest variations between JC and PC conditions. For JC conditions, joint tensile capacity controls, while for PC conditions either joint tensile or rotational capacity governs the pipeline performance. Pipelines with restrained axial slip joints are by far the most sensitive to the joint location relative to the fault, because of significantly lower rotational capacity relative to push-on and restrained joints.

5.4 Recommendations for Future Research

Recommendations for future research associated with each chapter of this thesis are provided under the headings that follow.

5.4.1 Response of Pipelines with Cured-In-Place Linings to Permanent Ground Deformation

The results of the experimental and numerical work presented in this thesis are directly applicable to pipelines with diameters of 100 mm to 200 mm retrofitted with cured-in-place linings (CIPLs), and generally applicable for pipe diameters of 300 to 600 mm. Additional experimental and numerical is needed for pipe diameters of 300 to 600 mm. Research also is needed to address the seismic performance of pipelines reinforced with other types of linings, such as cured-in-place pipes (CIPPs) and hand-placed lining systems. Three dimensional pipeline modeling for combined transverse and longitudinal deformation is recommended for pipelines with diameters larger than 600 mm.

Further investigation is needed of the bond strength vs. axial slip relationship along

the pipe/lining interface. To accomplish this, axial tension tests on full-scale lined pipe specimens with dense arrays of strain gages are recommended.

In this work the lining was treated as an isotropic material, using properties in the axial direction as determined by tensile coupon tests. Linings, however, are commonly manufactured with different reinforcements in the axial and hoop directions. It is recommended that anisotropy be taken into account in numerical simulations to represent better the lining properties.

The decomposition of pipeline response to fault rupture into components parallel and normal to the pipeline longitudinal axis is appropriate for pipelines reinforced with linings with negligible shear stiffness and flexural rigidity. This is the case for cured-in-place linings (CIPLs) that are quite flexible, but not necessarily for cured-in-place pipes (CIPPs) that are relatively rigid and stronger after curing. For CIPPs three dimensional models of a pipeline and pipeline/lining interface should be explored for a more accurate representation of de-bonding by shear in the circumferential and axial directions as well as de-bonding normal to the interior pipe surface. Abaqus offers a variety of options for interface modeling, using complex formulations, among which the Cohesive Zone Models is a promising choice.

5.4.2 Ductile Iron Pipeline Response to Permanent Ground Deformation

The results of the experimental and numerical work presented in this thesis are directly applicable to pipelines with diameters of 100 mm to 200 mm. Additional research is required to evaluate the response of pipelines with diameters in the range of 300 mm to 600 mm vs. fault/pipeline intersection angle.

Further experimental work is needed to quantify the reduction in axial tensile capacity of DI joints caused by combined rotation and tension and to determine the compressive stresses that result in leakage for combined joint rotation and compression.

Local buckling can be critical for pipelines with high D/t ratios. Modeling the three dimensional geometry of the pipeline allows for capturing changes in the geometry of the pipe cross-section (e.g. shell, elbow elements) and is recommended for the numerical modeling of pipelines with high D/t ratios.

The results of this study indicate that DI pipelines with restrained axial slip joints can accommodate higher displacement than those with restrained and push-on joints for almost the entire spectrum of pipeline/fault intersection angles, with the exception of cases that joint rotational capacity is the governing limit state. Redesigning the restrained axial slip joint to sustain higher rotations will make it the most viable option for pipelines subject to PGD hazards.

APPENDIX A

SIMPLIFIED MODEL FOR JOINT OPENING INCIPL-REINFORCED PIPELINE

A.1 Simplified Model Overview

A close inspection of Figure 2.20 can be converted into a single sinusoidal pulse as illustrated in Figure A.1. The ground strain, ε_g, due to a sinusoidal pulse is plotted relative to distance, X, along the pipeline. The pipeline is assumed to be flexible, thereby following the motion of the surrounding soil, resulting in pipeline strain $\varepsilon_p = \varepsilon_g$, everywhere that the pipeline is continuous.

At the location of a defect, i.e. crack or weak joint, lined with a CIPL, a tensile force P_u can be sustained, corresponding to a pullout strain $\varepsilon_u = P_u/EA$ for the pipe, where E is the pipe material modulus, and A is the cross-sectional pipe area. For tensile axial forces P > Pu, the CIPL de-bonds or ruptures, resulting in defect opening with minimal or no additional pullout resistance. As the seismic wave passes across the defect, strain in the pipeline on each side will accumulate linearly from $\varepsilon_p = \varepsilon_u = P_u/EA$ to $\varepsilon_p = \varepsilon_g$ at a slope of f_x /EA where f_x is the frictional resistance between pipe and soil. The shaded area in the Fig. A.1 is the integration of the differential strain between pipeline and ground, which is equal to the crack or weak joint opening. When the peak of the pulse passes over the location of the defect, the shaded area, and thus the defect opening, is maximized.

The actual defect opening is given by the areas within the lines included at f_x/EA from P_u/EA to the central part of the sinusoidal function. The simplified model estimates the defect opening as the area within the two right triangles superimposed on the

sinusoidal function. The simplified model always provides a defect opening larger than its counterpart in the field, and contains an error with a conservative bias. The error is generally small, as explained in Section A.3.

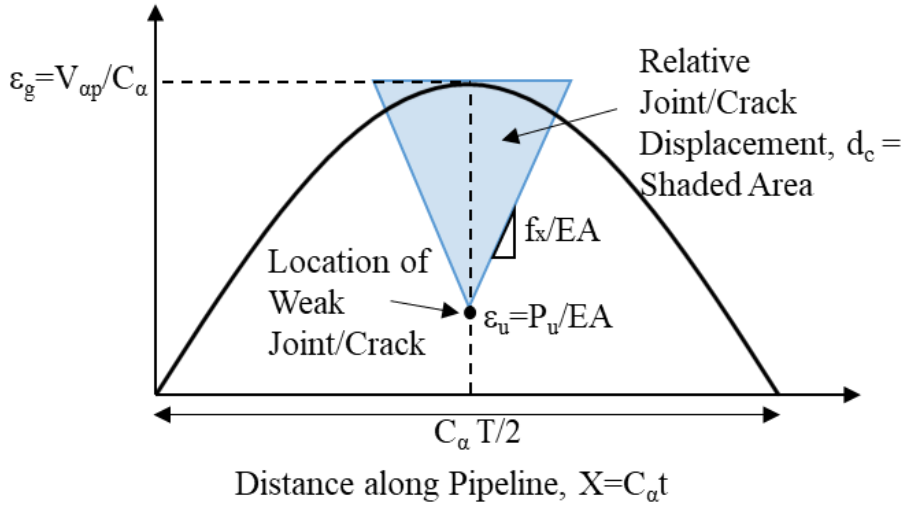

Figure A.1. Relative Joint Displacement from Sinusoid Pulse Interaction with a Pipeline Reinforced with a CIPL.

From the geometry of the triangle representing the crack opening displacement, d_c, in Figure A.1, it can be shown that:

$$d_c = \left(\frac{V_{ap}}{C_a} - \frac{P_u}{EA}\right)^2 \frac{EA}{f} = \left[\left(\left(\frac{V_{ap}}{C_a}\right)^2 - 2\frac{P_u}{EA}\frac{V_{ap}}{C_a} + \left(\frac{P_u}{EA}\right)^2\right)\right]\frac{EA}{f} \tag{A.1}$$

Given that the maximum ground strain is equal to:

$$\varepsilon_g = \frac{V_{ap}}{C_a} = \frac{V_p \sin 2\gamma_i}{2C} \tag{A.2}$$

where $V_{\alpha p}$ and C_α are the particle and wave propagation velocity in the pipeline axial direction, respectively, and V_p and C are the peak ground and wave propagation velocity along the wave propagation path, respectively.

Combining Eqns. (A.1) and (A.2) results in:

$$d_c = V_p^2\left(\frac{\sin 2\gamma_i}{2C}\right)^2\frac{EA}{f} - 2\frac{P_u}{EA}V_p\left(\frac{\sin 2\gamma_i}{2C}\right)\frac{EA}{f} + \left(\frac{P_u}{EA}\right)^2\frac{EA}{f} \tag{A.3}$$

Eqn. (A.3) is a quadratic equation with respect to V_p and yields the maximum value for d_c when γ_i=45°. Solving Eqn. (A.3), one obtains:

$$V_p = \frac{\frac{P_u}{f} \pm \sqrt{d_c\frac{EA}{f}}}{\frac{EA}{f}\left(\frac{\sin 2\gamma_i}{2C}\right)} \tag{A.4}$$

For $P_u = 0$, Eqn. (A.4) is reduced to:

$$V_p = \frac{2C}{\sin 2\gamma_i}\sqrt{d_c\frac{f}{EA}} \tag{A.5}$$

Setting the reference velocity equal to $V_{pRef} = V_p$ at γ_i=45°, then using Eqn. (A.4):

$$V_{p\,\mathrm{Re}\,f} = \frac{\frac{P_u}{f} \pm \sqrt{d_c\frac{EA}{f}}}{\frac{EA}{f}\left(\frac{1}{2C}\right)} \tag{A.6}$$

For any other intersection angle, the velocity V_p required to cause a crack opening equal to d_c must be higher than V_{pRef}. A higher V_p will correspond to a lower probability of occurrence or higher return interval than V_{pRef}. Given that $V_{pRI} = V_p > V_{pRef}$ at a recurrence interval RI, the combination of Eqns. (A.4) and (A.6) results in:

$$\frac{V_{pRI}}{V_{p\,\mathrm{Re}\,f}} = \frac{1}{\sin 2\gamma_i} \tag{A.7}$$

A.2 Combined Uncertainty of Seismic Velocity and Wave Path Orientation

The wave path orientation and angle of incidence, γ_i, in Figure 2.16 are illustrated for a direction, or polarity, towards the right. Using the simplified model described above and the wave propagation conditions presented in the figure, one can account for the combined uncertainty of the seismic velocity and wave orientation with respect to an underground pipeline by recognizing that the reference peak particle velocity, V_{pRef}, for $\gamma_i = 45^o$ is associated with the maximum crack displacement. All other wave paths will result in a smaller crack opening. Thus, the probability of exceeding the opening limit state for all other γ_i is zero, provided that the design peak ground velocity for the pipeline or pipeline network is less than or equal to V_{pRef}. Typically, the design peak velocity will be associated with an annual probability of occurrence, or return interval, V_{pRI}. If $V_{pRI} < V_{pRef,}$ no damage will occur in the lined pipeline at the location of the defect or weak joint. If $V_{pRI} \geq V_{pRef}$, then there will be angles of incidence that will cause pinching failure of the CIPL.

The plot of V_{pRI} / V_{pRef} vs. γ_i in Figure A.2 can be used to define a range of γ_i associated with lining failure and that range can be converted to a probability of exceedance. For instance, when $V_{pRI} / V_{pRef} = 2$, wave paths with angles of incidence of $15^o \leq \gamma_i \leq 75^o$ result in crack openings higher than d_c, which is the limiting condition associated with CIPL pinching failure.

Assuming that the pipeline has an equal chance of being intersected by a shear wave within the range of $0 \leq \gamma_i \leq \pi/2$, the variable γ_i follows a uniform probability density function, with:

$$f(\gamma_i) = \frac{2}{\pi}, \quad for\ 0 \le \gamma_i \le \frac{\pi}{2} \tag{A.8}$$

The probability of exceedance for any $V_{pRI} \geq V_{pRef}$ can be defined by determining the range of γ_i that results in failure and normalizing that range with respect to $\pi/2$:

$$p = \frac{N_f}{\pi / 2} \tag{A.9}$$

where N_f is the range of incidence angles γ_i resulting in a crack opening larger than d_c at a given V_{pRI}/V_{ref}.

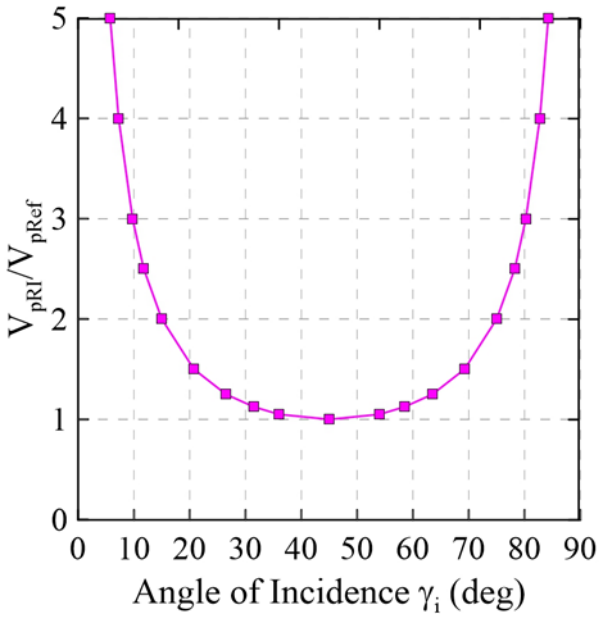

Figure A.2. V_{pPI} / V_{pRef} vs. Angle of Incidence γ_i for Pipeline with Crack/Weak Joint.

Given the results shown in Figure A.2 for the critical ranges of incidence angles γ_i associated with each V_{pRI} / V_{pRef} and Eqns. (A.8) and (A.9), the pipeline or pipeline system reliability R can be determined for each V_{pRI} / V_{pRef} , as follows:

$$R = 1 - p \tag{A.10}$$

Figure A.3 shows the pipeline or pipeline system reliability R as a function of V_{pRI} /

V_{pRef} for crack openings larger than d_c. It is noted that the reliability declines significantly with increasing V_{pRI} / V_{pRef} . For instance, a velocity 40% larger than V_{ref} results in pipeline reliability reduction of 50%.

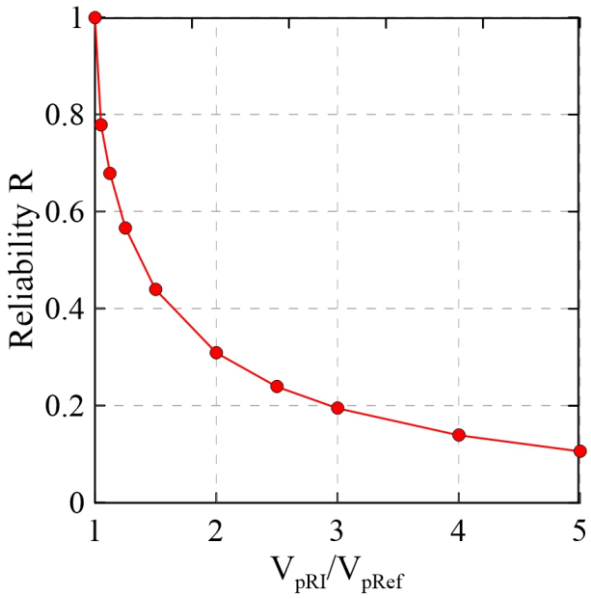

Figure A.3. Reliability vs. V_{pRI} / V_{pRef} for Pipeline with Crack/Weak Joint.

The reliability plot in Figure A.3 pertains to a wave direction, or polarity, of propagation to the right. The opposite polarity of wave propagation to the left results in the same V_{pRI} / V_{pRef} vs. γ_i and R vs. V_{pRI} / V_{pRef} relationships as shown in Figures A.2 and A.3, respectively.

For wave propagation polarities in both the right and left directions with range of $0 \le \gamma_i \le \pi$, the variable γ_i follows a uniform probability density function, with:

$$f(\gamma_i) = \frac{1}{\pi}, \quad for\ 0 \le \gamma_i \le \pi \tag{A.11}$$

The probability of exceedance for any $V_{pRI} \ge V_{pRef}$ can be defined by determining the range of γ_i that results in failure and normalizing that range with respect to π:

$$p = \frac{N_f}{\pi} \tag{A.12}$$

for which the symbols are defined after Eqn. (A.9) above. The combination of Eqns. (A.11) and (A.12) for both polarities results in a reliability plot that is identical to the one in Figure A.3.

A.3 Quantification of Error in the Estimate of Crack Opening

The error associated with the simplified model can be quantified by evaluating the difference in the area of the right triangles and area included within the lines at f_x/EA from P_u/EA to the central part of the sinusoidal function, as illustrated in Figure A.1.

The error is a function of the magnitude of the $\varepsilon_u = P_u/EA$ relative to the maximum ground strain ε_g, i.e. $\varepsilon_u / \varepsilon_g$, the pulse period T and the slope f_x /EA. Figure A.4 provides the error in the estimate of the crack opening using the simplified method as a function of the pulse period for $\varepsilon_u/\varepsilon_g$ equal to 0, 0.25, 0.50 and 0.75. The estimates are performed for a 150-mm ductile iron (DI) pipeline, buried in dense sand, at a depth of 1.3 m to the pipe centerline, subjected to a sinusoidal velocity pulse with V_p =200 cm/s. The error is very small, less than 10%, for the range of pulse periods and $\varepsilon_u/\varepsilon_g$ ratios examined. For pulse periods greater than 0.5 sec., which have been detected in numerous near source ground motion records, the error is less than 1%, confirming that the simplified method provides a very close estimate of the actual crack opening. Low $\varepsilon_u / \varepsilon_g$ ratios and low pulse periods are associated with the highest errors.

Figure A.5 shows the error in the estimate relative to the pulse period for different peak ground velocities of 100 cm/s, 200 cm/s and 300 cm/s, for $\varepsilon_u/\varepsilon_g = 0$ and the same

conditions as in Figure A.4. The higher the peak ground velocity, V_p, the higher the error in the crack estimate opening. For $V_p \leq 300$ cm/s, the error is smaller than 10%.

As discussed earlier, the error is also a function of the f_x /EA ratio. To explore the effect of this parameter on the error estimate, the case of a 1500-mm diameter steel pipeline buried at a depth of 1.7 m to the pipe centerline is considered. The steel pipe thickness is assumed to be equal to 9 mm, resulting in f_x/EA = 5×10^{-6} / m. The corresponding f_x /EA for the 150-mm DI pipeline used in this study is f_x /EA = 1×10^{-5} / m. Figure A.6 compares the error in the crack estimate for DI and steel pipes for V_p = 200 cm/s and $\varepsilon_u / \varepsilon_g = 0$. The error is a little higher for the steel pipeline, because of the lower value of the slope f_x /EA. However, the parameter f_x /EA is not expected to vary significantly for the burial depths and pipe geometries used in standard practice. Overall the maximum error in the estimate of the crack opening using the simplified method is expected to be less than 4% for pulse periods higher than 0.2 sec.

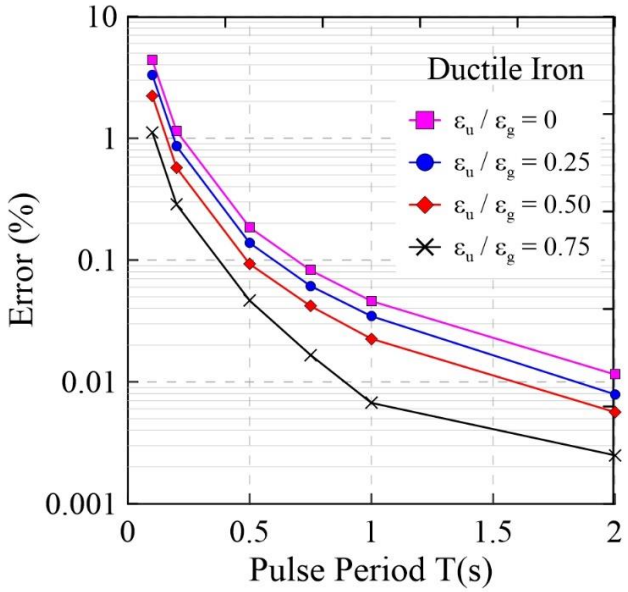

Figure A.4. Error in the Estimate of Defect Opening of DI Pipeline vs. Pulse Period for Different $\varepsilon_u / \varepsilon_g$ for V_p = 200 cm/s.

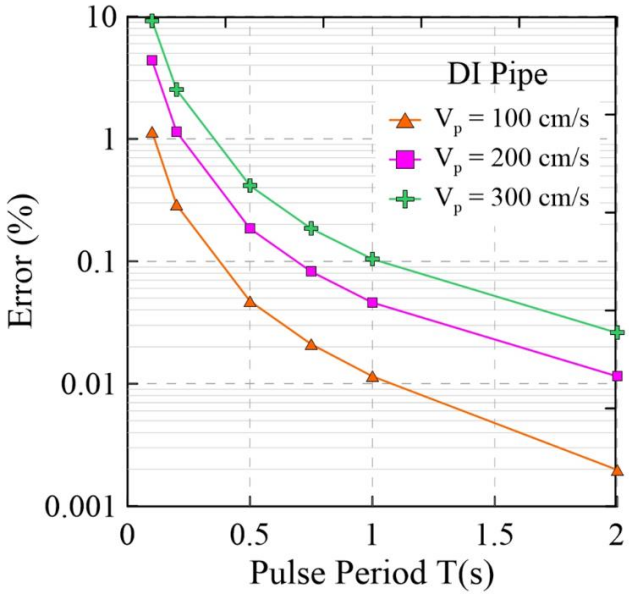

Figure A.5. Error in the Estimate of Defect Opening of DI Pipeline vs. Pulse Period for Different Peak Ground Velocities and $\varepsilon_u / \varepsilon_g = 0$.

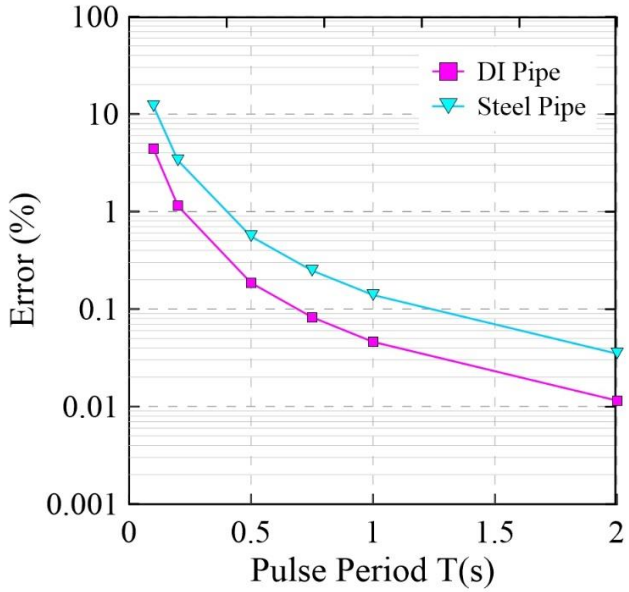

Figure A.6. Error in the Estimate of Defect Opening vs. Pulse Period for DI and Steel Pipelines, V_p = 200 cm/s and $\varepsilon_u / \varepsilon_g = 0$.

APPENDIX B

JOINT PULLOUT RATIO FOR PIPE CENTERED CONDITION

Large-scale fault rupture test results on jointed ductile iron (DI) pipelines indicate an uneven distribution of joint pullouts under pipe centered conditions in which pullout is concentrated at one joint. This observation is important because it sets a lower limit capacity for accommodating ground deformation than would occur if the axial slip were distributed more evenly between the two joints.

To understand this phenomenon additional analytical modeling was performed, as described in this Appendix. Figure B.1a shows a schematic of a pipeline subject to strike-slip faulting that induces tension and bending to the pipeline, similar to the experiments described in Chapter 3. The center pipe segment is centered on the fault, and both south (S) and north (N) joint bells face the same direction.

The accumulation of tensile ground deformation in the pipeline axial direction involves the opening of its joints and the relative motion of both bell and spigot with respect to the surrounding soil. Figures B.1b and B.1c present a representative force vs. displacement relationship for the spigot and bell end of the S and N joint, respectively. Experimental pull through tests on DI pipelines indicate that higher resistance is mobilized when the bell flat end, rather than the curved end, faces the direction of axial movement in the soil, as illustrated in Figure B.1, i.e. $K_S > K_N$. Please note that the axial component of the strike-slip displacement illustrated in Figure B.1 results in the flat face of the S joint and curved face of the N joint being pulled toward the fault rupture plane. The force vs. displacement relationship for spigot pullout from the bell end of the joint

shown in Figure B.1, has a linear portion of stiffness K_j, followed by a plateau when the maximum pullout capacity is reached. This simplification is consistent with experimental results of axial tension tests on push-on joints.

When the pipeline is subjected to tensile deformation, tensile load is carried through the joints resulting in spigot pulling out of the bell. At the same time, the bell of each joint moves in the direction shown in the Figure B.1a. The S joint bell encounters higher resistance to movement compared to N joint bell, resulting in S joint bell moving less under the same tensile force.

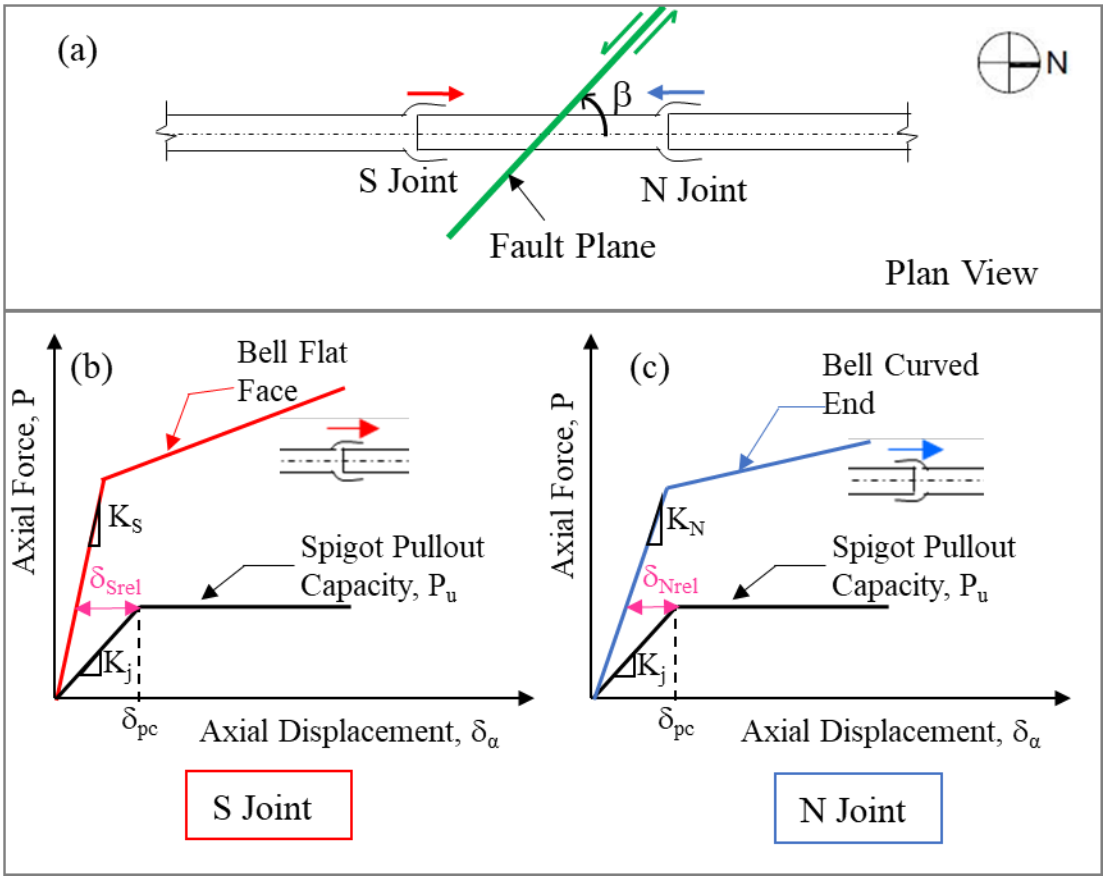

Figure B.1. (a) Schematic of Pipeline Subject to Strike-Slip Faulting in Pipe Centered Condition (b) Axial Tensile Force vs. Axial Displacement for Joint Bell Face Facing Rupture (c) Axial Tensile Force vs. Axial Displacement for Joint Curved End Facing Rupture

The opening of each joint is the result of the relative movement of spigot with

respect to the bell, which is equal to δ_{Srel} and δ_{Nrel}, for S and N joint, respectively. The pullout ratio of the S joint slip to N joint slip is defined as:

$$R_p = \frac{\delta_{Srel}}{\delta_{Nrel}} \tag{B.1}$$

Rearranging Eqn. (B.1) and expressing δ_{Srel} and δ_{Nrel} using the force P and stiffnesses K_j, K_N, K_S as defined and illustrated in Figures B.1b and B.1c), results in:

$$\left(\frac{P}{K_j} - \frac{P}{K_S}\right) = R_p\left(\frac{P}{K_j} - \frac{P}{K_N}\right) \tag{B.2}$$

Rearranging Eqn. (B.2), results in the following expressions:

$$1 - \frac{K_j}{K_S} = R_p\left(1 - \frac{K_j}{K_N}\right) \tag{B.3}$$

$$R_p - 1 = R_p\left(\frac{K_S - K_N}{K_S K_N}\right)K_j \tag{B.4}$$

Solving Eqn. (B.4) with respect to R_p:

$$R_p = \frac{\frac{K_S}{K_j}}{\frac{K_S}{K_j} - \left(\frac{K_S}{K_N} - 1\right)} \tag{B.5}$$

Large-scale pull through tests performed at Cornell (Wham et al., 2018; 2017a) on DI pipes show that $1.5 \leq K_S/K_N \leq 2.5$, resulting in $R_p > 1$. Test results are also consistent with the range of $2 \leq K_S/K_j \leq 3$. It should be noted that this range applies for only a low level of axial force required to mobilize the pullout capacity. Given that $2 \leq K_S/K_j \leq 3$, pullout ratios $1.5 \leq R_p \leq 2$ are obtained from Eqn. (B.5).

It is noted that there are many combinations of K_S, K_N and K_j to provide R_p. However, there is always a bias to $R_p > 1$, because $K_S/K_N > 1$, so that slip concentrates

always at the S joint. This is corroborated by experience in the lab. Following a uniform testing procedure, all fault rupture tests with jointed DI pipelines have been performed with the flat face of the bells facing north. Thus, the flat faces of the S joints and curved ends of the N joints were displaced axially towards the fault in all tests (Pariya-Ekkasut, 2018; Pariya-Ekkasut et al., 2018, 2017, 2016; Stewart et al., 2015). In every test the S joint closest to the fault slipped first before any other joint with no exceptions. In all cases, except one, the S joint closest to the fault failed first. In contrast, similar fault rupture tests performed with identical DI restraints on PCV jointed pipelines showed failure at the S joint as well as the N joint closest to the fault (Wham et al., 2017b).

REFERENCES

Pariya-Ekkasut, C. (2018). "Characterization of Hazard-Resilient Ductile Iron Pipelines Response to Earthquake-Induced Ground Deformation." PhD Dissertation: Cornell University.

Pariya-Ekkasut, C., Berger, B.A., Stewart, H.E. and O'Rourke, T.D. (2018). "Evaluation of McWane Seismic Flex Coupling for Resistance to Earthquake-Induced Ground Deformation." *Report, Prepared for Stuart Liddell, National Manager-MASD,* Cornell University, Ithaca, NY.

Pariya-Ekkasut, C., Stewart, H.E., Wham, B.P., O'Rourke, T.D., Bond, T.K. and Argyrou, C. (2017). "American Earthquake Joint System Resistance to Earthquake-Induced Ground Deformation." *Final Report, prepared for David Drake, American Cast Iron Pipe Company,* Cornell University, Ithaca, NY.

Pariya-Ekkasut, C., Stewart, H.E., Wham, B.P., O'Rourke, T.D. and Bond, T.K. (2016). "Direct Tension and Split Basin Testing of 6-in. (150-mm)-Diameter Kubota Earthquake Resistant Ductile Iron Pipe." *Final Report, prepared for Toshio Toshima, Kubota Corporation,* Cornell University, Ithaca, NY.

Stewart, H.E., Pariya-Ekkasut, C., Wham, B.P., O'Rourke, T.D., Argyrou, C. and Bond, T.K. (2015). "Hazard Resilience Testing of US Pipe Ductile Iron TR-XTREME^{TM} Pipe Joints." *Report prepared for Russ Huggins, PE, VP of Produce Development and Quality, US Pipe,* Feb. 2015, Cornell University, Ithaca, NY.

Wham, B.P., Pariya-Ekkasut, C., Argyrou, C., Lederman, A., O'Rourke, T.D. and Stewart, H.E. (2017). "Experimental Characterization of Hazard-Resilient Ductile Iron Pipe Soil/Structure Interaction under Axial Displacement." *Congress on Technical Advancement,* Sept. 10-13, Duluth, MN, available at: https://ascelibrary.org/doi/pdf/10.1061/9780784481028.013.

Wham, B.P., Berger, B., O'Rourke, T.D., Pariya-Ekkasut, C. and Stewart, H.E. (2017b). "Performance Evaluation of Bionax SR PVCO Pipeline with Extended Bell Joints under Earthquake-Induced Ground Deformation." *Final Report, prepared for Jeff Phillips, Western Regional Engineer, IPEX Management, Inc.,* Cornell University, NY.

Wham, B.P., Berger, B.A., Pariya-Ekkasut, C., O'Rourke, T.D., Stewart, H.E., Bond, T.K. and Argyrou, C. 2018. "Achieving Resilient Water Networks –Experimental Performance Evaluation." *11th U.S. National Conference on Earthquake Engineering,* June 25-29, Los Angeles, CA.

APPENDIX C

DERIVATION OF CORRECTION FACTOR FOR TRUE FRICTIONAL FORCES ON PIPE CIRCUMFERENCE

C.1 Derivation of Correction Factor

When a pipeline or conduit is intersected by soil movement, the at-rest conditions are disrupted, and the pipeline is subjected to frictional force directly related to the distribution of stresses normal to the pipe surface and indirectly related to p_H, which is the soil reaction force normal to the pipeline longitudinal axis.

To understand how p_H is related to the frictional force on the pipeline, pipe surface stress measurements with tactile pressure sensors are examined. As described by Palmer et al. (2009), a tactile pressure sensor is an array of small sensing units, called sensels, embedded in a polymeric sheet or pad that measures the magnitude and distribution of stresses normal to the sheet surface. Measurements with these sensors during large-scale 2D tests of soil-pipe interaction under relative horizontal displacement, δ_H, between pipe and soil (Palmer et al., 2009) were analyzed in accordance with Figure C.1.

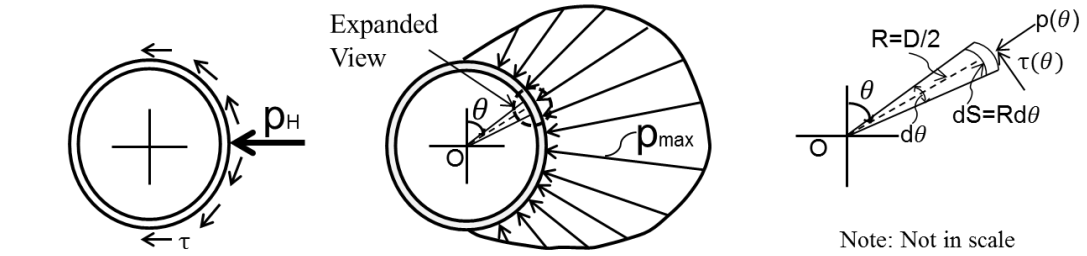

Figure C.1 Lateral Soil- Pipe Interaction Model for Underground Pipelines (Palmer et al., 2009)

As a pipe displaces laterally in soil, approximately half the pipe circumference is drawn away from the soil, while the other half is pushed towards the soil mobilizing passive pressures. This observation has been validated by test measurements and described in previous publications (e.g., O'Rourke et al., 2008; Palmer et al., 2009). Thus, the pressure is exerted predominantly on half the pipe. In partially saturated sands, there is virtually no pressure on the back of the pipe, because suction holds the soil particles in place and a void typically opens behind the pipe. The tactile pressure sensor data confirm that, at least for pipe depth to diameter ratios, H_c/D, of 3.5 to 7.5, measured pressures were virtually zero from $\theta=\pi$ to $\theta=2\pi$. This is consistent with the schematic of the pressure distribution shown in Figure C.1.

If $p(\theta)$ denotes the soil stress normal to the pipe surface as a function of angular position around the circumference, θ, and $\tau(\theta)= p(\theta)\tan\delta_s$ is the frictional shear stress, p_H is obtained by integrating the horizontal components of $p(\theta)$ and $p(\theta)\tan\delta_s$ as follows:

$$p_H = \frac{D}{2}\left[\int_0^{2\pi} p(\theta)\sin\theta d\theta + \tan\delta_s \int_0^{2\pi} p(\theta)\left|\cos\theta\right| d\theta\right] \tag{C.1}$$

The net horizontal force per unit length, p_H, can also be obtained from the experimental data using the following relation:

$$p_H = \sum_{j=1}^{J} p(m)_j S_j \sin\theta_j + \tan\delta_s \sum_{j=1}^{J} p(m)_j S_j \left|\cos\theta_j\right| \tag{C.2}$$

in which $(p_m)_j$ is the measured pressure, p_m, at the j-th pressure sensor node, S_j is the arc length associated with the j-th pressure sensor node ($S_j = 2\pi R/J$), θ_j is the angle defining the orientation of $(p_m)_j$, and J is the total number of pressure sensor nodes around the pipe surface per unit length.

Normal stress measurements taken by Palmer et al. (2009) for soil-pipe interaction in dry sand were normalized with respect to the maximum normal stress, p_{max}, and regressed with the sinusoidal curve fitting techniques described in Section C.2 to obtain distributions of measured normalized stress, $p(\theta)/p_{max}$. Two sets of measurements were regressed from tactile pressure sensors, denoted as Sensor B and Sensor A, located at the midpoint and a distance of ¼ the test pipeline length from its midpoint, respectively. The two datasets show slightly different normalized pressure distributions, and were selected to cover variations in pressure measured along the test pipeline. The regression analyses were performed on 24 and 12 different measurements at different levels of lateral soil movement for Sensor A and B, respectively. In each case, two erratic measurements were screened from the data at relatively low levels of lateral pipe movement before the maximum horizontal force was attained.

Figure C.2a is a plot of the regression equation for normalized pressure measured by Sensor A regressed with respect to angular distance, θ, from the pipe crown, as defined in the insert diagram. Also plotted in the figure are the normalized pressure distributions from finite element (FE) simulations using pipe shell and soil continuum elements performed by Jung et al. (2013) for the same large-scale 2D test reported by Palmer et al. (2009). The FE results correspond to 20 and 30 mm of relative horizontal pipe displacement, which is consistent with the relative displacements pertaining to the experimental data. The analytical and experimental normalized pressures are in close agreement.

Figure C.2b provides an alternative way of visualizing the data in which the normalized pressure, transformed as an inverse sine function ($\sin^{-1}$) in accordance with

Section C.2, is shown as a linear regression with respect to angular distance. The actual measurements are plotted in the figure. The linear regression involves rising and falling portions that are fit to the data by the least squares method.

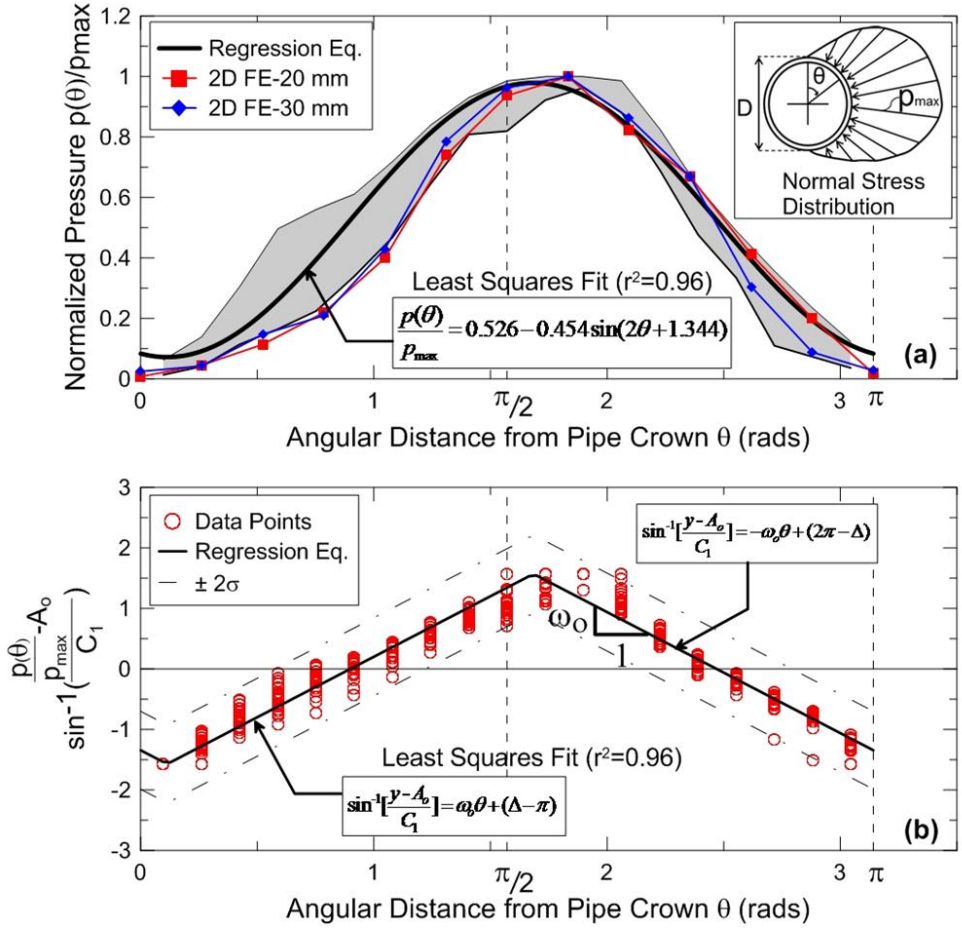

Figure C.2 Normalized Pressure vs. Angular Distance for (a) Sinusoidal Pressure Distribution and (b) Linear Regression with Transformed Normalized Pressure.

For Sensor A, the normalized pressure distribution (r^2=0.96) is given by:

$$\frac{p(\theta)}{p_{\max}} = 0.526 - 0.454\sin(2\theta + 1.344) \qquad \text{(C.3)}$$

The total normal force per unit distance, p_N, acting on the pipe can be calculated as the product of the maximum pressure and integration of the normalized stress distribution.

Similarly, p_H, can be determined by means of Eqns. C.1 and C.2. Both numerical integration of tactile pressure sensor measurements and closed form integration of Eqn. C.3 are in excellent agreement, yielding:

$$p_N = \frac{D}{2} p_{\max} \int_0^{\pi} \frac{p(\theta)}{p_{\max}} d\theta = 1.652 \frac{D}{2} p_{\max} \tag{C.4}$$

$$p_H = \frac{D}{2} p_{\max} \left[\int_0^{\pi} \frac{p(\theta)}{p_{\max}} \sin\theta d\theta + \int_0^{\pi} \frac{p(\theta)}{p_{\max}} \tan\delta_s |\cos\theta| d\theta \right] = \\ = \frac{D}{2} p_{\max} (1.346 + 0.757 \tan\delta_s) \tag{C.5}$$

The total frictional force, f_T, is the product of the normal force acting on the pipe and tan δ of the pipe surface, as follows:

$$f_T = p_N \tan\delta_s = 1.652 \frac{D}{2} p_{\max} \tan\delta_s \tag{C.6}$$

The apparent frictional force per unit pipe length, f_A, can be defined as:

$$f_A = p_H \tan\delta = \frac{D}{2} p_{\max} (1.346 + 0.757 \tan\delta_s) \tan\delta_s \tag{C.7}$$

It is convenient to estimate the longitudinal friction force during numerical simulation as the product of the force normal to the longitudinal pipeline axis and $\tan\delta_s$. Therefore, the ratio, f_T / f_A, is a correction factor that can be applied to the apparent friction, f_A, to reflect the total friction acting on the pipe. Combining Eqns. C.6 and C.7 results in:

$$\frac{f_T}{f_A} = \frac{1.652}{1.346 + 0.757 \tan\delta_s} \tag{C.8}$$

Figure C.3a shows f_T / f_A relative to $\tan\delta_s$ for both Sensor A and B measurements.

Figure C.3b provides a plot of the Sensor A and B measurements compared with the calculations of f_T / f_A vs. $\tan\delta_s$ from finite element (FE) simulations of lateral, upward, and downward pipe movement that are described under forthcoming sections of this paper. As shown in Figure C.3b, the experimental and numerical data for different types of pipe movement are in close agreement. The f_T / f_A vs. $\tan\delta_s$ relationship for Sensor A measurements is within ± 5% of the f_T / f_A values for lateral and vertical pipe movements. Hence, the f_T / f_A vs. $\tan\delta_s$ relationship for all orientations of pipe movement can be estimated with Eqn. C.8.

For polyethylene and polyvinyl chloride pipelines as well as pipelines with polyethylene or fusion epoxy coatings, $\tan\delta$ ranges between 0.3 and 0.6. As shown in Figure C.3, f_A and f_T are in close agreement for this range of $\tan\delta_s$, with variations up to 8%. For concrete pipelines, pipelines with mortar coatings, and metallic pipelines without coatings $\tan\delta_s$ typically is between 0.7 and 1.0 so that f_A is a conservative overestimate of f_T by about 12 – 21%.

Figure C.3 indicates that $p_H \tan\delta_s$ can be used to estimate the longitudinal frictional force on a pipeline with little to no error when $0.4 \leq \tan\delta_s \leq 0.6$ and to provide a conservative estimate when $\tan\delta_s > 0.6$. A reliable estimate of longitudinal frictional force, therefore, requires a coupled analysis in which p_H and $\tan\delta_s$ are combined.

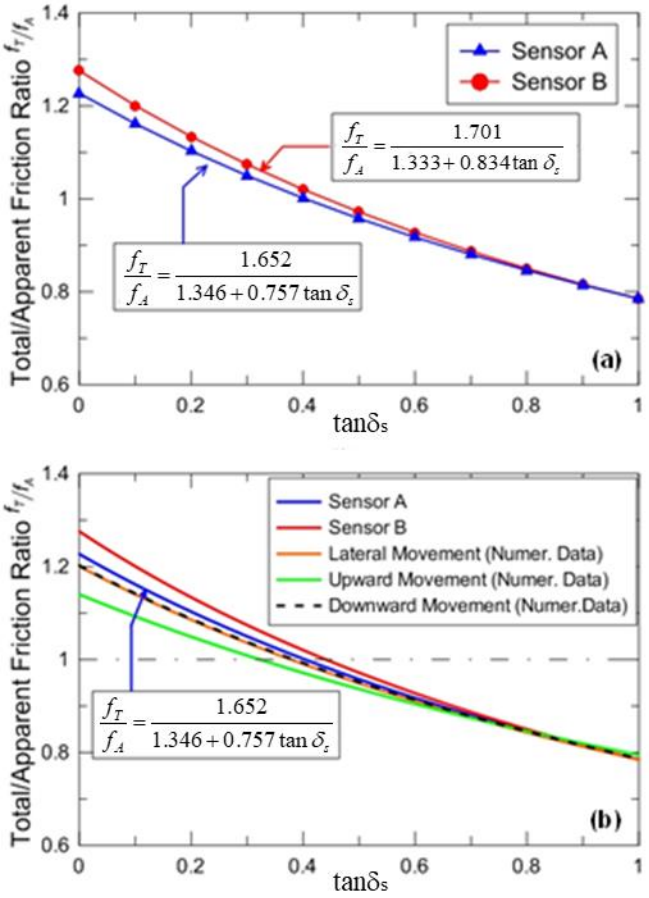

Figure C.3 Ratio of total to apparent friction f_T/f_A vs. $\tan\delta_s$ based on (a) tactile pressure sensor measurements and (b) tactile pressure sensor and numerical data.

C.2 Regression of Normalized Pipe Surface Stress Measurements

Curve fitting techniques described by Chapra and Canale (2006) for a sinusoidal function with angular frequency, ω_0, were used to derive an analytical expression for the normal stresses distribution. The least squares model follows the expression:

$$y = A_o + A_1\cos(\omega_o\theta) + B_1\sin(\omega_o\theta) \tag{C.9}$$

$$A_o = \frac{1}{N}\sum_{i=1}^{N} y_i \tag{C.10}$$

$$A_1 = \frac{2}{N}\sum_{i=1}^{N} y_i \cos(\omega_o \theta_i) \tag{C.11}$$

$$B_1 = \frac{2}{N}\sum_{i=1}^{N} y_i \sin(\omega_o \theta_i) \tag{C.12}$$

where θ is the angular distance from the pipe crown, and N is the number of equispaced data points. The alternative form for Eqn. (C.9) is:

$$y = A_o + C_1 \sin(\omega_o \theta + \Delta) \tag{C.13}$$

in which:

$$\Delta = \varphi + \frac{\pi}{2} \tag{C.14}$$

$$\varphi = \tan^{-1}\left(-\frac{B_1}{A_1}\right) \tag{C.15}$$

$$C_1 = \sqrt{A_1^2 + B_1^2} \tag{C.16}$$

Eqn. (C.13) can be rearranged as follows:

$$\sin^{-1}\left[\frac{y - A_o}{C_1}\right] = (\omega_o \theta + \Delta) \tag{C.17}$$

When $A_1 < 0$, π needs to be added to φ.

REFERENCES

Jung, J.K., O'Rourke, T.D. and Olson, N.A. (2013). "Lateral soil-pipe interaction in dry and partially saturated sand." *Journal of Geotechnical and Geoenvironmental Engineering*, 139(12): 2028-2036.

Chapra, S.C. and Canale, R.P. (2006). "Numerical Methods for Engineers." *McGraw Hill*: New York.

O'Rourke, T.D., Jezerski, J.M., Olson, N.A., Bonneau, A.L., Palmer, M.C., Stewart, H.E., O'Rourke, M.J. and Abdoun, T. (2008). "Geotechnics of pipeline system response to earthquakes." *Geotechnical Earthquake Engineering and Soil Dynamics IV (GEESD)*, Sacramento, CA.

Palmer, M.C., O'Rourke, T.D., Olson, N.A., Abdoun, T., Ha, D. and O'Rourke, M.J. (2009). "Tactile pressure sensors for soil – structure interaction assessment." *Journal of Geotechnical and Geoenvironmental Engineering*, 135(11): 1638 – 1645.